Time domain, near-infrared diffuse optical methods for path length resolved, non-invasive measurement of deep-tissue blood flow

Marco Pagliazzi

A thesis presented for the degree of
Doctor of Philosophy

Institut
de Ciències
Fotòniques

Medical Optics Group (Advisor: prof. Turgut Durduran)
ICFO, Castelldefels (Spain)
June 30th, 2019

Dedication

In memory of my father Enrico
for teaching me how important is to learn.

Abstract

The non-invasive and, often, continuous measurement of the hemodynamics of the body, and for the main purposes of this thesis, the brain, is desired because both the instantaneous values and their changes over time constantly adapt to the conditions affecting the body and its environment. They are altered in pathological situations and in response to increased function. It is desirable for these measurements to be continuous, reliable, minimally invasive, and relatively inexpensive. In recent years, optical techniques that, by using diffusing and deep-reaching (up to few centimeters) light at skin-safe levels of intensity, combine the aforementioned characteristics, have increasingly become used in clinical and research settings. However, to date there is, on one side the need to expand the number and scope of translational studies, and, on the other, to address shortcomings like the contamination of signals from unwanted tissue volumes (partial volume effects). A further important goal is to increase the depth of penetration of light without affecting the non-invasive nature of diffuse optics.

My PhD was aimed at several aspects of this problem; (i) the development of new, more advanced methods, i.e. the time/pathlength resolved, to improve the differentiation between superficial and deeper tissues layers, (ii) the exploration of new application areas, i.e. to characterize the microvascular status of bones, to study the functional response of the baby brain, and (iii) to improve the quality control of the systems , i.e. by introducing a long shelf-life dynamic phantom.

In conceptual order, first I introduce long shelf-life reference standards for diffuse correlation spectroscopy. Secondly, I describe the use of an existing hybrid time domain and diffuse correlation spectroscopy system to monitor the changes that some pathological conditions, in this case osteoporosis and human immunodeficiency virus infection, may have on many aspects of the human bone tissue that are currently not easy to measure (i.e. invasively assessed) by conventional techniques. Thirdly, I describe the development of a novel time domain optical technique that intimately combines, introducing many previously unmet advancements, the two previously cited optical spectroscopy techniques. For the first time I was able to produce a time domain device and protocol that can monitor the blood flow *in vivo* in the head and muscles of healthy humans. Lastly, I describe a device and method that I have used to monitor changes in blood flow in healthy human infants of three to five months of age, for the first time in this age bracket, as a marker of activation following visual stimulation.

Overall, this work pushes the limit of the technology that makes use of diffuse light to minimally invasively, continuously, and reliably monitor endogenous markers of pathological and physiological processes in the human body.

Resumen

La medición no invasiva y, a menudo, continua de la hemodinámica del cuerpo, y para los propósitos principales de esta tesis, del cerebro, es conveniente porque tanto los valores instantáneos como sus variaciones en el tiempo se adaptan constantemente a las condiciones que afectan el cuerpo humano y su entorno. Estas suelen alterarse en situaciones patológicas o como respuesta a una mayor función. Es deseable que estas mediciones sean continuas, confiables, mínimamente invasivas y relativamente asequibles. En los últimos años, las técnicas ópticas que, mediante el uso de luz difusa para medir los tejidos en profundidad (hasta unos pocos centímetros) mediante niveles de intensidad que son seguros para la piel, combinan las características arriba mencionadas, se han utilizado cada vez más tanto en entornos clínicos como de investigación. Sin embargo, al día de hoy hay, por un lado, la necesidad de ampliar el número y el ámbito de los estudios translacionales y, por el otro, de suplir a las deficiencias como por ejemplo la contaminación de volúmenes de tejido no deseados (efectos de volumen parcial). Otro objetivo importante es aumentar la profundidad de penetración de la luz sin afectar la naturaleza no invasiva de la óptica difusa.

Mi doctorado está destinado a mejorar varios aspectos de este problema; (i) el desarrollo de nuevos métodos más avanzados, es decir, el

método resuelto en el tiempo/trayectoria de los fotones, para mejorar la diferenciación entre los tejidos superficiales y profundos, (ii) la exploración de nuevas áreas de aplicación, es decir, para caracterizar el estado microvascular de los huesos, para estudiar la respuesta funcional del cerebro en los niños, y (iii) para mejorar el control de calidad de los sistemas, es decir, mediante la introducción de un phantom dinámico de larga vida útil.

En orden conceptual, primero voy a introducir estándares de referencia de larga vida útil para la espectroscopia de correlación difusa (DCS). En segundo lugar, voy a describir el uso de un sistema híbrido espectroscopia tiempo-resuelta (TRS) con DCS ya existente para monitorizar los cambios que algunas condiciones patológicas, en este caso la osteoporosis y la infección por el virus de la inmunodeficiencia humana, pueden comportar para muchos aspectos del tejido óseo humano que actualmente no se pueden medir con facilidad (es decir, se van evaluado de forma invasiva) mediante técnicas convencionales. En tercer lugar, voy a describir el desarrollo de una novedosa técnica óptica en el dominio temporal que combina íntimamente, introduciendo muchos avances previamente no cumplidos, TRS y DCS. Por primera vez pude producir un dispositivo y un protocolo tiempo-resueltos para medir el flujo de la sangre en la cabeza y en los músculos de seres humanos sanos. Por último, en esta tesis voy a describir un dispositivo y un método que he usado para monitorear los cambios en el flujo sanguíneo como marcadores de activación del cerebro debida a estímulos visivos en bebés entre tres y cinco meses de edad.

En general, este trabajo amplia los limites de la tecnología que hace uso de la luz difusa para monitorizar, de forma mínimamente invasiva, continua y confiable los marcadores endógenos de procesos patológicos y fisiológicos en el cuerpo humano.

Acknowledgements

I want to thank my supervisor for his patient guidance. I also acknowledge the contribution of our collaborators, Dr. Sanathana Konugolu Venkata Sekar, Lorenzo Colombo, Dr. Alberto Dalla Mora, Dr. Alessandro Torricelli, Dr. Davide contini, Dr. Antonio Pifferi, Dr. Edoardo Martinenghi, Dr. Lorenzo Spinelli, Dr. Andrea Farina, Dr. Paola Taroni and Dr. Laura di Sieno from Politecnico di Milano (Milano, Italy), Dr. Ernesto Vidal Rosas, Claus Lindner and Dr. Aykut Eken from ICFO (Castelldefels, Spain), Dr. Nuria Sebastian-Galles, Marc Colomer Canyelles, Dr. Carlos Guerrero-Mosquera, Dr. Chiara Santolin from the Center of Brain and Cognition of Universitat Pompeu Fabra (Barcelona, Spain), Dr. Eugenia Negredo, Nuria Perez-Alvarez, Dr. Anna Bonjoch, Dr. Patricia Echeverria, Dr. Roser Escrig, Dr. Bonaventura Clotet from Lluita contra la Sida foundation (LSF, Germans Trias i Pujol University Hospital, Badalona, Spain) and Dr. Joaquim Rosales from Digest (Badalona, Spain). I want to thank Dr. Claudia Valdes, Dr. Hari Varma, and Dr. Tanja Dragojevich form ICFO, and Dr. Judith Gervain, Laboratoire Psychologie de la Perception, Universite Paris Descartes (Paris, France) for her helpful and constructive advice.

I'd like to thank all the people that I had the chance to meet by being part of the Medical Optics Group which were not listed before: a big thanks goes to Miguel, Peyman, Francisco, Michal, Parisa, Clara, Joseph, Lorenzo, Pablo, Lisa, Giuseppe, Stella, Federica, Ameer, Jonas, Susanna, Manish, Laura, Gemma, Igor, Gianluca, Udo, Kristian, Claudia, Daniel, and Martin... you all were there when I had doubts about the matter; a big thank you also goes to everybody who populated ICFO during these years and who did his share to make it a nice place to work and live. A very special "thank you!" goes to Xavier Menino and to Jose Carlos Cifuentes from ICFO's Mechanical and Electronic workshops, respectively, and all the staff there: Alberto, Oscar, Xavi, ... Thanks to all the people that helped me while I was visiting Polimi: Sara, Amedeo, Edoardo, Anurag, Edoardo, Marta, Ileana, Pranav, Lina, Marta, Rebecca, Andrea.

On the personal side, this would not have been possible weren't for the patience and of my girlfriend Sara... and for the closeness of both my family and friends (sometimes I forget the difference: it doesn't matter, I love you guys!), so thank you Paola, Daniele, Aldo, Andrea (M), Pousa, Blanca, Laura, Andrea (F), Carles, Emanuele and last but not least Manu, Paolo, Marcel and Michael from the band. Thanks to everybody that supported me while I was roaming the continent for this experiment or that conference: Giulio, Anton, Ka, Tommy, Ila, Lorenzo, Federico, Manu, Giulia, Gabriele, Diego and Daniele.

Good luck also to the students that I had the pleasure to meet and in part to supervise while I was at ICFO: Jordi, Lorenzo and Alba.

Contents

List of Figures

List of Tables

Chapter 1

Introduction

> Said there's gotta be some meaning to the purpose of life
> I know there must be more than the struggle and strife
>
> Cro-Mags, *The Age of Quarrel*. Profile Records, 1986

Visible light is an obvious tool to use in medical physics for diagnosis. In order to obtain information from deep tissues, a visible and near-infrared radiation window (approximately ∼650 to 950 nm) is today at the focus of a renewed technological interest, due in part to an increased understanding of the physical modeling of the photon propagation in tissues. The leitmotif of the present work is the improvement of diffuse optics as a quantitative technique for the non invasive continuous monitoring of the physiology of oxygen metabolism in humans. A particular focus is on the "window" that opens to non-invasively measure the adult brain due to the fact that the scalp and skull are relatively transparent to light in the wavelengths as was first reported by Joöbsis in the 70s [9].

From an historical perspective, transillumination, the inspection of the body using a strong source of light at one side and detection (either by eye or by a detector) on the other side, is documented since the nineteenth-century. Some specific kinds of tumor, like some mammarian cancers [1, 2], or even in some cases the presence of hydrocephalus in babies [3], could be (and as a matter of fact they are still) seen by the naked eye as they generate a detectable contrast in the reddish glow of a breast or a head sitting in the way between the observer and an intense source of light. Image details, however, are quickly lost: light gets randomly redirected (i.e. scattered) by microscopical constituents (e.g. cells, organelles, and proteins). Scattering also enhances light dissipation by the optically active substances naturally present in tissue, termed chromophores. Without scattering centers, the human body would have the transparency of feebly colored glass [4]. Nonetheless, some light does still reach through, carrying useful information. In diffuse optical spectroscopy, for example, attenuation at a certain wavelength of resonance of a chromophore is a marker of its concentration and local environment [5]. In diffuse correlation spectroscopy, the fluctuations of the interference pattern of multiply scattered light can be examined to infer about the dynamics of light scattering particles like red blood cells [6, 7].

It seems evident that the key for the transition from a qualitative to a quantitative use of light to investigate deep inside the human body resides in the availability of a more intimate knowledge of the process of photon migration in turbid tissue. Perhaps the most impactful advancement in the field has been the understanding that light transport in tissue at the length scale of several centimeters can be conveniently modeled as a diffusive random process [8]. Another method for dealing with scattering was to resort to time domain methods. Time-gating techniques for example can exploit the fact that light photons that leave the transilluminated object at earlier time after its injection travels a shorter and straighter path than the ones leaving later [9, 10]. The consequent correction of systematic errors that plagued the early days of transillumination allowed for quantitative estimation of the optical properties of tissue with light. Nowadays, quantitative diffuse optics spectroscopy (DOS, also termed near infrared spectroscopy, NIRS) is used in a wide range of applications, from the measurement of the ripeness of fruit, to functional brain studies [11], to the monitoring of critically ill patients [12]. Time domain methods, which are getting more and more accessible [13] in terms of price and ease of use, due to advancements in source and detector technologies but also perhaps to the better understanding of the underlying physics mechanisms, allow the absolute characterization of the concentrations of tissue components and, in some cases that I discuss, of their dynamics.

Diffuse correlation spectroscopy (DCS) is, if compared with NIRS, a relatively new technique. Diffuse correlation spectroscopy makes use of measurements of the autocorrelation of speckle intensity fluctuations of coherent laser light that underwent multiple scattering in the diffusive regime with moving light scatterers, which in the perfused tissue are mostly red blood cells, in the microvasculature [5]. It has been proven to be a reliable tool for the noninvasive assessment of blood flow in the microvasculature [7]. Absolute values of the blood flow index (BFi) have been found to correlate with many other techniques that measure blood flow like xenon-enhanced computed tomography (Xe-CT) and arterial spin labeling magnetic resonance imaging (ASL-MRI) [14]. Measuring microvascular blood flow offers complementary information with respect to NIRS that allows the computation of metabolism through endogenous markers, continuously, in fast ($\sim$1 s) processes [14].

Time resolved near infrared spectroscopy (TRS), also referred to as time domain (TD) NIRS, measures the distribution of photon path lengths in tissue in the diffusive regime [15]. In reflectance (i.e. backscattering) geometry, detected photon path lengths statistically correlate to the depth of penetration, and longer path lengths correspond to photons that have travelled deeper inside the tissue[16]. The combination of TRS and DCS modules can use the estimated local optical properties for fitting the DCS data to obtain absolute blood flow index and oxygenation values in a continuous way. This has been demonstrated in several studies [17, 18, 19, 20].

The case for hybrid NIRS/DOS-DCS

As a continuous-wave technology that can not readily sort photons by their path lengths, DCS suffers from partial volume effects and systemic changes in the superficial tissue layers. Furthermore, in order to accurately estimate absolute blood flow, DCS requires knowledge of the absorption and scattering properties of the probed volume. The latter can be tackled by hybrid systems that utilize an independent FD or TD NIRS device to measure the absorption and scattering coefficients μ_{a} and μ_{s}' in absolute way, or, at least, CW NIRS devices that measure μ_{a} changes.

However, the proposed and used hybrid solutions so far use separate laser sources and detectors; the two techniques are made to work together by using optical filtering, with a consequent sub-optimal light collection efficiency, or using time-multiplexing, which reduces the sample rate. In addition to this, as described in [21, 17], the two techniques have different penetration depths and sampling volumes, possibly resulting in partial volume effects that are difficult to correct and that depend on the optical properties and structure of the tissue being probed. The ultimate combination would consist in using pulsed sources, similar to those used in TRS, to measure a path length resolved DCS signal.

Unfortunately, standard picosecond pulsed sources have too low coherence lengths to be used as DCS sources [22, 23, 24, 25]. In reflectance geometry, typical tissue optical properties result in distributions of the path lengths that are much wider (in the order of 10 m). When the coherence length ℓ_c is smaller or comparable to the span of photon path lengths, the signal-to-noise ratio of DCS is expected to decrease and the model relation used to explain the measured intensity autocorrelation becomes non-trivial [26, 27]. The existence of a finite time-bandwidth product acts as a physical limit on the coherence length of pulsed sources [28, 29]. Some sort of compromise must be made in order to use the same pulsed sources for TRS (short pulse needed) and DCS (short bandwidth needed).

Time-domain DCS

As shown in the pioneer work by Yodh, Kaplan and Pine [30] in the context of diffuse wave spectroscopy (DWS), by selecting a part of (i.e. by *time gating*) the photons stream from which the autocorrelation is generated based on their times-of-flight, one can make the technique insensitive on the distribution of photon path lengths, directly recover the reduced scattering coefficient of the medium, and ultimately separate the contribution of photons coming from shallow and deep layers in tissue. Time-of-flight measurement for each photon is only possible with narrow pulses sources and very precise timing of the photon detection. The first experimental design that achieved this, however, made use of the frequency up-conversion phenomenon in nonlinear crystals [30], and therefore relied on high laser power that can strongly interfere with the sample, limiting its applications to non-biological media and making *in vivo* applications not possible.

Recently there has been a renewed interest in time-of-flight resolved DCS, as a group from Harvard's Martinos Center managed to make it feasible at relatively low source light levels [31]. However, the low source power prevented *in vivo* human experiments from being carried out with this system, and experimental reports were limited to small animals. The advancements that I have introduced, which allowed for the first time *in vivo* continuous measurement of blood flow and optical properties in humans, is be discussed in depth in chapter 3.

Contributions Since this was first of all a collaborative work between ICFO and Politecnico di Milano, I feel it's mandatory to insert here a detailed description of my contribution. Among the results presented in this chapter, I took care of the experimental design (the retrieval and integration of the existing components, the choice of the experimental parameters), the management and recruitment of human subjects, most of the experimental work, the totality of the data analysis here presented, and the dissemination (redaction of the manuscripts for publication in peer reviewed journals and conference talks).

Functional DCS

Functional near infrared spectroscopy (fNIRS) is a relatively inexpensive technique aimed to detect localized brain metabolic activation non-invasively and, most importantly, quietly and without the need for confinement of the subject's head. Neuronal metabolic activation in the human cortex is in fact temporally correlated with hemodynamic changes (neurovascular coupling) that, happening few millimeters or centimeters below the scalp, can be probed by NIR diffuse light from the skin surface. In adults, the mechanism of localized increase of blood flow following neuronal activation is known as *reactive hyperemia*, and is well documented [32].

While NIRS measures relative changes in oxy- ([HbO_2]) and deoxy- ([Hb]) hemoglobin concentrations [11], DCS can capture any alteration in the blood flow in the cortex. It has a spatial resolution of few millimetres and temporal resolution of about 1 s or less. It is argued that, for functional studies, cerebral blood flow (CBF) is a marker with faster onset and greater contrast. Continuous wave DCS is inherently more sensitive to the brain than other continuous wave techniques [21]. Visual activation has been the object of study and is widely used for validation of novel instruments and techniques, also in awake infants [33, 34]. For these reasons, it is considered here as the target physiological change to be measured by functional DCS. In particular I have aimed to fDCS monitoring the reactive hyperemia following visual stimulation in awake infants of about 4 months of age. For this population, non-invasive diffuse optical assessment of CBF is interesting because MRI cannot be used without sedation. Methods and results are discussed in chapter 4.

Contributions Since the work described in this chapter is the result of a collaboration between ICFO and the center for Brain and Cognition at Pompeu Fabra University, Barcelona, Nuria Sebastian Galles' group, I state that my contributions were the experiment design (the probe and the rest of the device were built by me starting from off-the-shelf components), the redaction of the technical part of the documents that were then successfully evaluated by the ethical committee, the totality of data analysis, and the dissemination (redaction of a poster presented at an international conference).

Hybrid NIRS/DOS-DCS to detect bone pathologies

As anticipated, NIRS/DOS can offer information on a variety of tissues that goes beyond the quantification of the local concentrations of oxy- and deoxy-hemoglobin ([HbO_2] and [Hb], respectively): water, lipid, collagen and other light absorber concentrations in tissue have been quantified in many studies [5, 7, 35, 36, 37, 38, 20, 17, 39, 40, 41]. NIRS has also recently been applied to the systematic study of bone density in humans [39, 41]. On the other side, DCS can provide information on hemodynamics inside the tissue, e.g. microvascular blood flow. Both are indeed portable, relatively inexpensive, non-invasive, safe, continuous and fast proven clinical methods that use non-ionizing radiation, and this constitutes a niche that no single medical technology is able to fill at the moment: MRI, for example, is not portable, fast or inexpensive. The combination of information on microvascular tissue hemoglobin concentrations and blood flow obtained by non-invasive diffuse optical methods can yield information about tissue oxygen metabolism and contribute to early detection and therefore to reduce morbidity and mortality of bone-affecting pathologies. In the recent years, the first studies evaluating bone using NIR/DOS and DCS have been published in humans [7, 35, 37, 38, 20, 39, 41, 42] and in animals [43, 44].

Therefore, as previous preliminary data suggests [37], NIR/DOS and DCS can be useful as tools that are able to assess bone properties and, in particular, to provide complementary information to the dual-energy X-ray absorptiometry scans, that to these days is the gold-standard for the assessment of bone structural properties, but lacks functional (i.e. hemodynamics) contrast. To this end, I have conducted a study to evaluate bone tissue composition and microvascular parameters using a hybrid NIRS/DOS-DCS approach in human immunodeficiency virus (HIV)-infected patients, affected or not by osteoporosis. Subjects that are infected with HIV are in fact a population at high risk for bone pathologies like the loss of bone mineral density and low-energy bone fractures [45, 46, 47, 48, 49]. I have compared these results with those I obtained scanning HIV-negative controls. Part of this data was previously presented in reference [39], which further supports the effectiveness of the methodology in the study of bones at multiple body locations. Here I have tested the hypothesis that osteoporosis is a condition associated with a lower tissue perfusion and altered tissue constituents concentrations that can be therefore probed by hybrid near infrared diffuse correlation and broadband time resolved spectroscopies non-invasively measuring a bone prominence of the leg, the trochanter.

The methods and results of a comparative, case-control study on 53 subjects are discussed in chapter 5.

Contributions My contributions to this collaborative work were partially the experimental design, the design and manufacturing of the probe, the data analysis and interpretation; I also participated in the redaction of a published journal paper and I am redacting another journal paper (in preparation) that is more closely related to what is presented here.

Measurement standards for hybrid NIRS

In medicine, systems that reproduce the properties of a body district, organ or tissue are called phantoms and they are most commonly found in the realm of medical imaging. In medical optics, tissue phantoms are produced to replicate the optical properties of specific tissue and are commonly used to assess instrument reliability, to compare imaging systems, and to train personnel. A phantom is generically requested to be reproducible, easy to supply, possibly low cost, and to have accurately determined and stable optical properties [50]. Phantom engineering constitutes, by any means, one of the technological challenges that a translational project has to face. Highest accuracy diffuse optical measurement with hybrid TRS and DCS devices are needed to this extent.

Methods and results of the experimental development of the first, to the best of my knowledge, long lasting (∼months) synthetic phantom are reported and discussed in chapter 6.

Contributions My contributions to the work presented in this chapter, which stems from the Babylux project, were the design of the phantom, the design and execution of the experiments, and the data analysis.

Concluding remarks

In this thesis, I have expanded the number and scope of translational studies carried out with diffuse optical and correlation spectroscopy, and I have proposed a technical solution (the time/pathlength resolved method) that is able to tackle three of its shortcomings: partial volume effects, limited depth of penetration, and how the former affect estimation of absolute values of blood flow. The proposed solution is still non-invasive in nature. I also have proposed an improved, long shelf-life, phantom for quality assessment of diffuse correlation spectroscopy.

Chapter 2

Theory

In this Chapter, I provide the basic information to appreciate the crucial features of the propagation of photons in tissues. Therefore, it only provides with the minimal information needed in order to understand the limits and the relevant scales of the physical models that I have used to analyze the data presented in this thesis. Furthermore, I provide the basic equations and algorithms that are pertinent and that are cited throughout this thesis work. In doing so, I'd like to allow the readers to be able to follow the main research results and methods; if desired, please go to the references therein and have a deeper dive into the physics.

2.1 Photon migration in tissue

Scattering and absorption

Photon migration in tissue is conveniently modeled as a random process. Light has a probability to interact with microscopic centers spanning a great range of sizes, varying between roughly few Å (e.g. ∼64 Å of hemoglobin) to tens of µm, which is the diameter of the large mammalian cells [51]. Interactions can result in a photon dissipating its energy (absorption) or changing its direction of propagation (scattering) [52]. Also, note that part of this thesis (see section 2.2) is based on quasi-elastic scattering, but for the main purposes, the scattering processes are considered elastic. Some phenomena like fluorescence, polarization effects and others are not considered. Focusing on a single photon path: the probability of interaction (scattering or absorption) is proportional to the inverse of the number density of the centers (i.e. the volume of tissue that on average contains a single center) divided by the *total* cross-section of the two processes, thus defining a characteristic length or mean free path, $\ell_t = 1/\mu_t$. Let us suppose that the interaction events are independent and identically distributed.

If scattering and absorption are two independent processes, the transport coefficient μ_t can be conveniently written as the sum of absorption (μ_a) and scattering (μ_s) coefficients. A property that comes very handy when modeling photon migration is that, in tissue, μ_a is generally much lower than μ_s.

Very frequent elastic scattering in tissue has the effect of randomizing the direction of propagation of light: photons quickly lose the information on their direction of origin. For this reason imaging (i.e. microscopy) opportunities are severely hindered already in samples of few tens of micron thickness [52]. The exact thickness of tissue that determines a complete randomization depends, other than scattering coefficient μ_s, on the preferential direction of re-emission of the scattered light; both are microscopical properties that vary greatly among different tissues. The wider the mean scattering angle, the shorter the distance that photons have to travel to start behaving as diffusers in a three dimensional random walk. Another typical length called transport mean free path (TMFP) can be introduced, denoted by ℓ_{tr}, which represents the mean propagation distance that has to be traveled by a photon to become diffusive; the associated reduced scattering coefficient can be defined as the inverse of the TMFP (ℓ_{tr}),

$$\mu_s' = \frac{1}{\ell_{tr}} = (1-g)\mu_s, \tag{2.1}$$

where g is the average of the cosine of the angle of scattering (the angle between the incident and scattered direction for each scattering event). In tissue, in the NIR water window, g generally varies between $\sim$0.6 and $\sim$0.9, meaning preferentially forward-directed scattering [53].

Absorption spectroscopy

An important consequence of handling photon migration as a random process is that tissue absorption depends linearly on the concentration of the chromophores in it contained. For each wavelength, having defined an extinction coefficient $\epsilon_i(\lambda)$ and being c_i the (e.g. molar, M) concentration of the i-th chromophore of interest, the absorption coefficient can be expressed as

$$\mu_a(\lambda) = \sum_i \epsilon_{a,i}(\lambda)\, c_i \tag{2.2}$$

If the absorption coefficient can be measured at multiple wavelength, eq. 2.2 is converted in a system of equations that can be solved to determine the concentrations c_i, provided the extinction coefficient spectrum $\epsilon_{a,i}(\lambda)$ of each chromophore is known. In [54] the spectra of oxygenated ([HbO_2]) and deoxygenated ([Hb]) hemoglobin and other chromophores responsible for light absorption in the NIR window (e.g. fat and water) are available and some of them are plotted in fig. 2.1 for typical concentrations found in tissue.

An optimal choice of wavelengths for example used in oxy- and deoxy-hemoglobin quantification has been shown to be a pair, one in

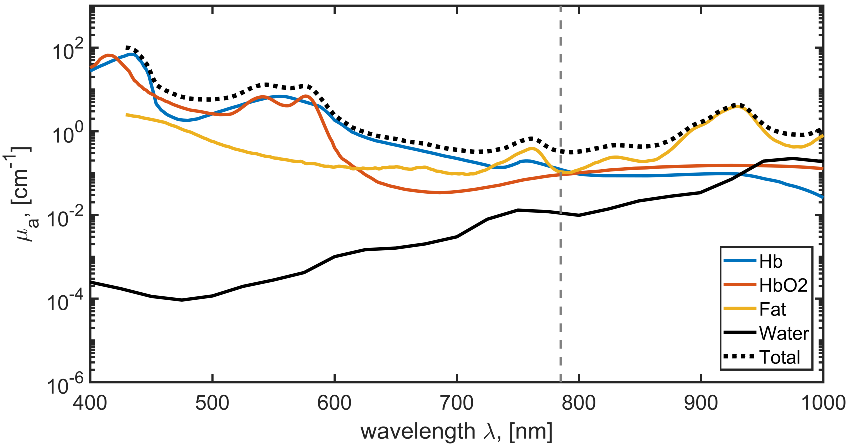

Figure 2.1: Absorption properties of tissue computed using typical concentrations: total hemoglobin THC=[HbO$_2$]+[Hb], 155 µM; tissue oxygen saturation StO$_2$=$[\mathrm{HbO_2}]/\mathrm{THC}$, 65%; fat, 30%; water, 50% (data from [54]). The vertical dashed line represent the wavelength used for most of our experiments (785 nm), which is near to the isobestic point for hemoglobin.

the range 660 to 760 nm and one at 830 nm [55, 56, 57]. It is worth noting that in order to absolutely quantify concentration it is necessary to have absolutely quantified absorption coefficients.

Scattering spectroscopy

The spectral shape of scattering carries information about the size of the scatterers. An effective scatterer size can therefore be interpreted from the data acquired with a broad band time resolved spectrometer. For homogeneous, independently behaving spheres, the Mie theory can be used to predict the angular distribution and the intensity of each scattering event. Even though light scatterers in tissue are neither spherical nor uniform in size, a wide range of experiments [51, 58, 37] show good agreement with the Mie prediction

$$\mu_s'(\lambda) = a\left(\frac{\lambda}{\lambda_0}\right)^{-b} \tag{2.3}$$

in the 600 to 1000 nm range. When eq. 2.3 is compared to the experiments, a and b are fitted as free parameters, and show a dependency, respectively, on the scatterers concentration and on the Mie-equivalent size of the scatterers. In a variety of tissue (abdomen, forehead, and arm) b has been found varying between 0.47 and 1.79 [58] and in the cancellous bone of the calcaneous, broad spectral fit of 6 subjects ranged between 0.4 and 0.65 [37]. Scattering centers with spatial dimensions that are much smaller than the wavelength of light show a faster decaying spectrum, towards the limit of Rayleigh scattering, thus exhibiting a $\sim \lambda^{-4}$ dependency.

2.1.1 *In vivo* tissue spectroscopy

Near infrared spectroscopy (NIRS) is aimed to the quantitative assessment of tissue composition by its interaction with light. Two approaches are here discussed: continuous wave (CW) and time domain (TD). Continuoys wave NIRS makes use of a continuous light source and a detection apparatus that can be photon counting or analogical, as long as it is able to detect variations of intensity due to the changes in optical properties of the sample. Source intensity can be modulated, especially in multiple spatial channel systems, generally up to a few kHz frequency. This allows to frequency-tag the detection channels for time-interleaved operation and to exploit phase-locked signal amplification techniques. *In vivo*, its application is limited to the assessment of relative, small (linear) changes in time (t) of chromophores concentrations Δc_i, which are manifest as changes in optical density (OD), defined by the modified Beer Lambert law [5]:

$$\Delta OD(\lambda,t) = -\log\left(\frac{N(\lambda,t)}{N_0(\lambda)}\right) \approx \frac{\partial OD(\lambda,t)}{\partial\mu_a}\sum_i \Delta c_i\,\epsilon_{a,i}(\lambda) =$$
$$= DPF(\rho,\mu_s',\mu_a,\lambda)\sum_i \Delta c_i\,\epsilon_{a,i}(\lambda) \tag{2.4}$$

Its derivation requires assuming no changes in the scattering properties of the medium during the measurement, $\partial OD/\partial\mu_s'=0$, and small changes in the OD so its expression can be truncated to the first order term of a Taylor expansion with respect to the changes in the optical properties. The differential path length factor (DPF) depends on μ_s' and on the source-detector separation (ρ), and it cannot be measured by the CW approach; is usually found tabulated for the tissue of interest. Although multi-distance CW NIRS [59] can quantify absolute optical properties in homogeneous samples, its accuracy is still not adequate even for bulk measurements of oxygenation [60]. Time domain NIRS, on the contrary, employs light source providing pulses lasting a few tens of picoseconds and sub-nanosecond resolution photon counting detectors. By detecting temporal shape changes of the injected pulses it can disentangle the contributions of scattering and absorption, which can be absolutely quantified. It is also intrinsically stable to changes in the overall intensity that are generated e.g. by movement of the sample. It was shown that TD methods can readily regress extracerebral systemic changes from deeper brain ones [61, 62], a feature that CW techniques used in functional studies struggle to achieve [63]. Frequency domain (FD) NIRS, another commonly used approach, allows the independent determination of μ_a and μ_s' by measuring the phase shift and attenuation of a very rapidly (~100 MHz or above) intensity modulated source [15].

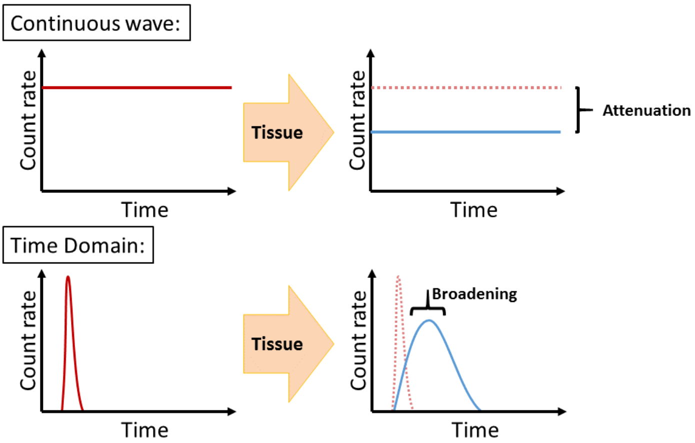

Figure 2.2: Two common NIRS approaches for the quantitative study of biological tissue properties. Compared to continuous wave, which measures only the relative changes (attenuation) of a known source, time domain methods, by measuring the temporal broadening of a known short (∼100 ps) pulse of light, allow disentangling μ_a from μ_s' contributions.

2.1.2 Diffusion approximation

A quantitative approach to tissue spectroscopy greatly benefits from a convenient model of photon migration that can predict, and therefore be compared to, the measured optical signals. An equation describing radiative transport, the RTE, can be written for the radiance L (in units of $\mathrm{W\,cm^{-2}\,sr^{-1}}$) based on the balance of energy (the continuity equation) inside a 3D volume element of tissue. However, with some assumptions a much simpler equation can be used to describe photon migration through a turbid medium [64]. This equation, termed the diffusion equation (DE), combines a continuity equation with Fick's first law of diffusion for photons, which introduces a photon diffusion coefficient $D = \ell_{tr} v/3$ (in units of $\mathrm{cm^2\,s^{-1}}$). It is generally written for the fluence rate ϕ (in units of $\mathrm{W\,cm^{-2}}$), which is the integral of the radiance L for all solid angles. This formulation is an analogous to the diffusion of heat in a metal and generally similar to those that describe propagation of particles that are not driven by external forces [65]. This much simplified and more tractable description of radiative transport in turbid media has been tested extensively and found to describe light transport phenomena in many cases of interest with an accuracy that is comparable to the RTE [66].

Boundary conditions

Several analytical solutions of the DE are known, depending on the boundary conditions of interest. In this work, the semi-infinite approximation for the reflectance geometry is considered. In this geometry, the turbid medium is modeled as a infinite slab on the spatial xy-coordinates plane, having infinite thickness, and having a boundary on the $z = 0$ plane, where the source of light (a pencil beam that is perpendicular to the boundary) is located. The detector is also located on the same boundary, defining a source-detector separation ρ. Mathematically, the exact partial flux or the simpler extrapolated-zero boundary conditions [67] can be used when there is a sharp difference in the index of refraction across the $z = 0$ plane, $n_r = n_{in}/n_{out}$. In the first case, the fluence rate ϕ is related to its gradient at the boundary

$$\phi = z_b\, \hat{n} \cdot \nabla\phi \qquad \text{at the interface} \tag{2.5}$$

(with $\hat{n}$ the unit vector pointing outside the surface, i.e. negative z direction) while in the second ϕ is Taylor expanded to the first order around the interface

$$\phi(z) = \phi(z=0) + \left.\frac{\partial\phi}{\partial z} z\right|_{z=0} \Rightarrow \phi(-z_b) = 0 \tag{2.6}$$

In both cases, z_b is called extrapolated boundary distance, and depends on the transport length $\ell_{tr} = 1/\mu_s'$ and the effective Fresnel reflection coefficient R_{eff} [5]

$$R_{eff} \approx -1.44 n_r^{-2} + 0.71 n_r^{-1} + 0.668 + 6.36 \cdot 10^{-3} n_r \tag{2.7}$$

as

$$z_b = 2\ell_{tr} \frac{1 + R_{eff}}{1 - R_{eff}} \tag{2.8}$$

This last formulation (eq. 2.8) is equivalent to considering two isotropic light sources located one at $z = \ell_{tr}$ inside the medium and one outside at $z = -(\ell_{tr} + 2z_b)$; it is a reasonable approximation to the exact boundary [67, 66]. The method of images can be applied to obtain the analytical solutions of the DE in a variety of geometries [5].

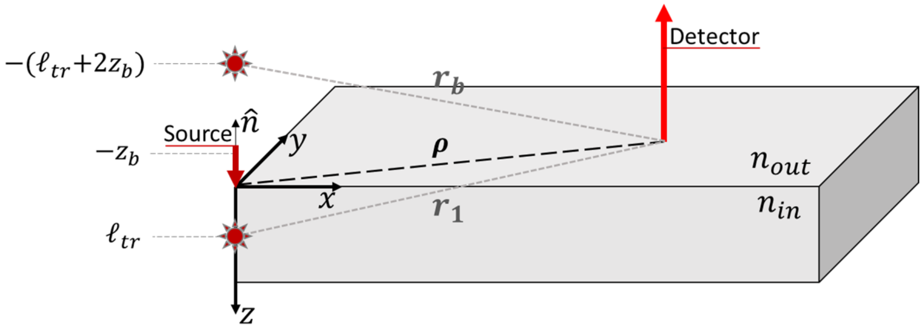

Figure 2.3: Schematic of the semi-infinite geometry described in the text. The separation between source and detector is ρ. Two image sources, one inside and one outside the medium, are modeled at the xy position of the source.

A general property of the RTE and of DE is that, when a Green's function solutions G (solution of for a Dirac's delta source in both space and time), is known, solutions to more complex source configuration can be obtained by convolution integrals [65, 5]. Another useful property regarding the solution space is that if $L_0(\boldsymbol{r}, \hat{\Omega}, t)\Big|_{\mu_a=0}$ is a Green's function solution of the RTE for the non-absorbing case (μ_a=0), then

$$L(\boldsymbol{r}, \hat{\Omega}, t) = \exp(-\mu_a\, vt)\; L_0(\boldsymbol{r}, \hat{\Omega}, t)$$

is still a solution when a homogeneously absorbing medium of absorption coefficient μ_a is considered. It is postulated that this property are still valid for the diffusion approximation of the RTE [68].

Diffuse reflectance

An analytical expression for the light intensity recorded by a fiber at a distance ρ from the source, on a semi-infinite medium with coefficients μ_a and μ_s', index of refraction $n_{in} = n$, having a boundary at $z = 0$ with air (n_{out}=1) and for a radiant source of intensity $S(\boldsymbol{r}, t) = S_0 \delta(\boldsymbol{r}) \delta(t - t0)$ that is small compared to the source-detector distance ρ (e.g. a laser beam exiting from a fiber), was first obtained by Patterson *et al.* [69] using a derivation for DE formulated for an absorbing medium. This solution, termed reflectance function $R(\rho, t)$, can be introduced as the Green's function solution of the DE in terms of the square modulus of the photon flux

$$\begin{aligned} R(\rho, t) &= |\boldsymbol{J}(r = \rho, z = 0, t)| = \\ &= S_0\, (4\pi\, D\, t)^{-3/2}\, z_b\, (t - t_0)^{-5/2} \exp\left[-\frac{\rho^2 + z_b^2}{4D(t - t_0)}\right] \cdot \\ &\quad \exp\left[-\mu_a\, v(t - t_0)\right] \end{aligned} \tag{2.9}$$

by using the polar symmetry of the considered geometry.

Here it is noteworthy that the dependency on the absorption coefficient appears simply as a multiplicative exponential factor

$$\exp\left[-\mu_a\, v(t - t_0)\right]$$

of the non-absorbing solution.

2.1.3 Time resolved spectroscopy

Frequency and time domain methods can be used to disentangle and therefore separately measure the absorption and scattering properties of tissue. In time domain, time resolved spectroscopy (TRS), the broadening of short (1 to 100 ps) laser pulses at a wavelength of interest (for tissue spectroscopy, wavelength λ is chosen in the NIR water window, 600 to 1200 nm) can be used to characterize a turbid medium and precisely measure its absorption and scattering coefficients, provided a model of light transport in the experimental geometry of interest is known. Limited to diffusive semi-infinite turbid media, this is conveniently carried out by comparing the solution of the diffuse reflectance $R(t)$ (eq. 2.9), convoluted with the instrument time response function (IRF), with the distribution of times of flight (DTOF); the DTOF is in fact the broadened profile of the laser pulse after it has traveled trough the medium. Timing electronics (e.g. time correlated single photon counters, TCSPC) and precise (i.e. low jitter) single photon detector can be used to measure the delay between the detection of a photon and its emission; the DTOF is therefore obtained when enough photons are collected (in order to overcome photon counting Poisson noise) and the histogram of their arrival time is computed [70]. In reflectance geometry, if ~100 µm core fiber optics are used as source and detector points, $R(t)$ can be estimated as the Greeen's function solution of the DE for some relevant boundary conditions [69, 68].

Linear method

With TRS, the error of the estimation of optical properties (namely μ_a and μ'_s) is generally a few percent for typical measurement conditions in tissues [18, 71]. An even more accurate and precise estimation of optical properties is particularly important for developing recipes for reference standards (phantoms). To do so, a linear method has been proposed [71]. It relies on two properties of the solution of the RTE and DE.

First, if the difference between two experiments depends only on the changes in the absorption coefficient $\Delta\mu_a$, by invoking the scaling property of DE and RTE the detected intensity (by instance, the normalized reflectance $\tilde{R}'(t)$) changes with respect to the baseline normalized $\tilde{R}(t)$ only by the multiplication by a factor $\exp(-\Delta\mu_a\, vt)$. Experimentally, computing the natural logarithm ratio of the two reflectances yields

$$\log\left(\frac{R(t;\mu_a)}{R'(t;\mu_a+\Delta\mu_a)}\right) = \Delta\mu_a\, vt + \log\left(\frac{A}{A'}\right) \tag{2.10}$$

where A' and A are the count rates of the two measurements. Changes in absorption can be therefore recovered by estimating the slope through a linear fit of the logarithm of the ratio of a certain number of reflectance measurements with respect to time. I stress that the measurements have to be carried out at the same distance ρ, with the same instrument and therefore the same IRF, and on samples differing one from each other only by the absorption coefficient. Even though these assumptions are hard enough to make its application to living tissue sound questionable (although often a requirement in some CW NIRS formulations), it is an ideal condition when titrating the concentration e.g. of ink in a phantom. Care must be taken in using inks and pigments that have a non-negligible *albedo*, as their concentration shall contribute only to sample's absorption and not to scattering.

Secondly, by looking at the form of the solution of the DE with extrapolated boundary conditions (e.g. eq. 2.9), the only dependence on the source-detector separation ρ resides in the exponential factor $\exp\left(-\rho^2/4D(t-t_0)\right)$. Therefore, by taking the natural logarithm of two measured $R(t;\rho)$ and $R(t;\rho+\Delta\rho)$ one obtains

$$\log\left(\frac{R(t;\rho)}{R'(t;\rho+\Delta\rho)}\right) = \mu_s' \frac{3\Delta\rho}{4v}\frac{1}{t} + \log\left(\frac{A}{A'}\right) \tag{2.11}$$

This time, the reduced scattering coefficient μ_s' can be recovered from a linear fitting between the variables $1/t$ and $\log(R/R')$, for a certain number of reflectance measured at different source detector separations.

Following the error analysis reported in [71], an error in the estimated optical properties as low as 0.5% for absorption and 1.5% for reduced scattering of a phantom preparation can be reached by this method.

2.1.4 Depth of penetration of photons

Interestingly, unlike in the CW case, when time domain methods are used the penetration depth of photons in a turbid medium in reflectance geometry does not depend neither on the source-detector separation nor on the absorption coefficient [72, 16]. The penetration depth increases as the photon time-of-flight increases. This seems counter-intuitive, but can be proven matematically by modeling light transport in reflectance geometry in a slab of depth d. In this case, the probability a photon detected at a distance ρ and time-of-flight t

has of reaching depth z, indicated as $p(\rho, t, z)$, is proportional to the reflectance measured if the slab thickness was infinite (semi-infinite medium) *minus* the reflectance for a slab of thickness $d = z$. This basically corresponds to the fraction of reflectance photons that would be lost due to the finite thickness of the medium. The exact expression for $p(\rho, t, z)$ is given in [72] by computing the reflectance in a turbid slab, and although the reflectance does depend on the optical properties of the medium and on the source-detector separation, both the time resolved probability $p = p(t, z)$ and the mean path length in tissue within a layer of thickness d at a depth z, $\langle s \rangle(t, z, d)$ do not depend on them[1].

The dependence on μ_a and ρ is evident in CW techniques; in the steady state the optical properties and ρ determine the probability distribution of time-of-flight at the detector. Longer separation for example imply longer average times-of-flight, that in turn correspond to higher depth of penetration of the photons. This fact has been widely utilized in research. In their work for example Yu *et al.* ([73]) used increasing source detector separations in the range 0.5 to 3 cm to probe deeper into the more metabolically active and reactive muscle tissue of the arm during a cuff occlusion. An extract is shown in figure 2.4.

2.1.5 Depth of penetration enhancement by time-of-flight gating

Late photons that convey to the detector information about deep tissue are rare and hard to detect, i.e. signal-to-noise is poorer [13]. The

---

[1] An implication of this is that the average maximum and mean penetration depth $\langle s_{max} \rangle$ and $\langle s \rangle$ do depend on the time-of-flight only. For quantitative estimation of these quantities, please refer to [16], fig.5 a) and b).

input power of light cannot be raised above the maximum permissible exposure limit for skin and, even so, the rapid decay of reflectance as time-of-flight increases means that shallow-dwelling early photons are preponderant and consume the dynamic range of the measurement if they are not properly accounted for. The time-dependent, semi-infinite medium solution in eq. 2.9 is however a monotonous decreasing continuous function with respect to the source-detector separation ρ, which means that more photons are being detected *at any time-of-flight* as ρ decreases. For this reason, a null-separation approach has been first proposed [74] and then implemented [75]. Null separation time domain approaches combine the advantages of having more photons available at every time-of-flight and of having an increase spatial precision by minimizing the partial volume effects, as photon migration is confined to smaller volumes (see fig 2.5). On a technological point of view, the overwhelming contribution of the small time-of-flight photons can be neglected by using a fast gated detector synchronized with the pulse emission time and turned on, at each pulse, at a delay corresponding to the maximum time-of-flight of the early coming photons to be rejected.

2.2 Speckle fluctuations and light scatterers dynamics

2.2.1 Diffusing wave spectroscopy

Quasi elastic light scattering, also known as dynamic light scattering (DLS) or photon correlation spectroscopy, is a widespread technique used among other things for particle size determination [76]. It uses the single scattering theory to interpret the correlation of the intensity of light scattered by small concentrations of scatterers. In 1987, Maret and Wolf first introduced experimentally a way to study the Brownian dynamics of light scatterers in the multiple scattering regime [77], highlighting a strong dependence on the experimental geometry of the data. Photon diffusion theory was applied to the quantitative interpretation of data [78] and the technique was termed diffusing wave spectroscopy (DWS). In DWS, a model for the electric field autocorrelation can be written as

$$g_1(\tau) = \int_0^\infty R(s)\, \exp\left(-2\frac{\tau}{\tau_0}\frac{s}{\ell_{tr}}\right) ds \tag{2.12}$$

where τ is the autocorrelation time and $R(s)$ is the probability of detecting a photon with path length s in the sample. An equivalent expression can be found substituting the time-of-flight $t = s/v$ for media in which n (and therefore v) is homogeneous. In eq. 2.12, $\tau_0 = (D_B\, k_0)$ is the characteristic decay time of the autocorrelation which depends on the Brownian diffusion coefficient D_B (in units of $\mathrm{cm}^2\,\mathrm{s}^{-1}$) of scatterers [2], and $k_0 = 2\pi n/\lambda$ is the wave number of light in the medium. The exponential factor in eq. 2.12 can be interpreted as the contribution to the autocorrelation decay of a single path length, and s/ℓ_{tr} is the average number of randomized scattering along the path. Two of the most remarkable improvements of DWS over DLS, apart from working in multiple scattering regime, are the sensitivity to movement of the scatterers over length scales much smaller than λ, and a much weaker dependence on the size dispersion of the light scattering particles [79]. If long paths with high number of scattering, therefore carrying the contribution of many scattering events, are considered, each particle need to be displaced by only a small distance for the total path length to change by a wavelength. On average, DWS is sensitive to scattering displacements of the order of $\lambda\,(s/\ell_{tr})^{-1}$.

---

[2] This should not be confused with the photon diffusion coefficient D introduced previously

2.2.2 Diffuse correlation spectroscopy

In the first half of the 90s of the past century the seminal work of Ackerson *et al.* [80], and the later contribution by Boas *et al.* [6], introduced a mathematical way to describe the transport of the electric field ($\boldsymbol{E}(\boldsymbol{r},t)$) non-normalized autocorrelation in turbid media like the tissue

$$G_1(\boldsymbol{r},\tau) = \langle \boldsymbol{E}(\boldsymbol{r},t) \cdot \boldsymbol{E}^*(\boldsymbol{r},t+\tau) \rangle \tag{2.13}$$

where $\langle\cdot\rangle$ denotes the expectation value or equivalently, by a experimental point of view, the ensemble average over the realizations of an experiment, τ is the correlation lag time, and $*$ denotes the complex conjugate. Relying on the diffusion approximation for describing photon transport, this equation was termed correlation diffusion equation (CDE), and solutions are known in the semi-infinite reflectance geometry for extrapolated boundary conditions[5]

$$G_1(\rho,z,\tau) = \frac{v}{4\pi D}\left[\frac{\exp(-K(\tau)r_1)}{r_1} - \frac{\exp(-K(\tau)r_b)}{r_b}\right] \tag{2.14}$$

with

$$\begin{aligned} K(\tau) &= \sqrt{3\mu_a\mu_s' + k_0^2\,\mu_s'\,\langle\Delta r^2\rangle\,\tau} \\ r_1 &= \sqrt{\rho^2 + (z-\ell_{tr})^2} \\ r_b &= \sqrt{\rho^2 + (z+2z_b+\ell_{tr})^2} \end{aligned}$$

(for a graphical representation of r_1 and r_b please refer to fig. 2.3). The term $\langle\Delta r^2(\tau)\rangle$ in K represents the mean square displacement of the light scatterers during time τ and has been found [81] to be best approximated in perfused tissue by

$$\langle\Delta r^2(\tau)\rangle = 6\,\alpha D_B\,\tau$$

which namely corresponds to red blood cells that behave as Brownian diffusers in the tissue, having a diffusion coefficient D_B, and interacting with light with a probability α with respect all the other scatterers. Despite being essentially the same thing, in terms of technology, as DWS, one generally refers to it as diffuse correlation spectroscopy (DCS) when it is applied to the study of living perfused tissue, due to historical reasons.

In a typical DCS experiment, the normalized intensity autocorrelation g_2 is computed from a stream of timed photon detection events yielded by a photon counting device. A quantitative model for the decay of the normalized electric field autocorrelation function $g_1(\tau)$, derived from the photon diffusion approximation for a wide range of commonly used experimental geometry, is fit to the data to recover a blood flow index (BFi) as a free parameter. The model in equation 2.14 can fit intensity correlation data only if the electric field $\boldsymbol{E}$ is a Gaussian variable in time with zero mean, an assumption that has been found to be true *a posteriori* for most biological tissue [5, 82]. It relies on the fact that a high number of scattering events along the photon paths happen to be with mutually independent moving scatterers (i.e. the sample is ergodic). In this case the Siegert relation [27]

$$g_2(\tau) = 1 + \beta \left| G_1(\tau)/G_1(0) \right|^2 \tag{2.15}$$

allows fitting the measured (normalized) intensity autocorrelation $g_2(\tau)$ with the model presented in eq. 2.14. An estimation of the blood flow index BFi=αD_B is obtained as a best fit parameter.

Optical absorption and scattering coefficient (μ_a and μ_s', respectively) in eq. 2.14 affect the estimation of the BFi value; they need to be independently estimated by time domain or frequency domain spectroscopy (time resolved spectroscopy, TRS, and FD-NIRS, respectively), otherwise only relative changes of BFi can be detected under the assumption that the effects of changes in μ_a and μ_s' are negligible during the measurement.

The signal-to-noise ratio of DCS depends among other parameters on the optical coherence length of the laser light and/or the number of independent electric field modes that are detected and resolved [83]. The experimental parameter β is an experimental constant that depends among other things on the number of detected modes and on the coherence length of the laser [83]. In order to achieve optimal SNR, state-of-the-art DCS instruments make use of a continuous wave laser that has very narrow bandwidth and, therefore, long coherence length. Namely, coherence length must be much longer than the maximum difference of the path length that the detected photons traverse in the tissue [83].

Despite the fact that BFi has dimensions $\mathrm{cm}^2\,\mathrm{s}^{-1}$ it has been found to strongly correlate with other techniques that measure blood flow *in vivo* in human tissue, as Xenon-enhanced computed tomography (Xe-CT), positron emission tomography (PET) and arterial spin labeling magnetic resonance imaging (ASL-MRI) [14]. Recently it has been proposed that by measuring the transit of intravenously injected indocyanine green boluses in brain tissue, relative changes in DCS signal (rBFi) can be calibrated to obtain absolute cerebral blood flow [84, 85].

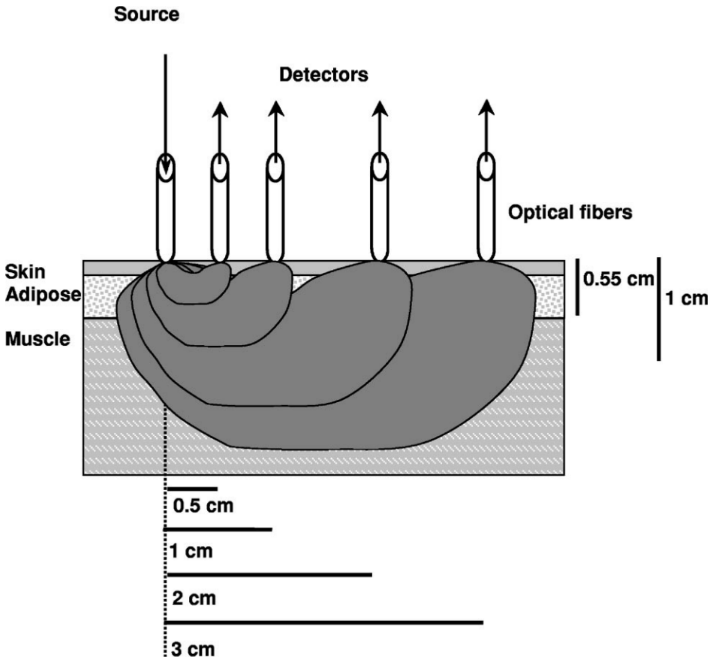

Figure 2.4: A schematic of a multi-layer tissue model and the simplified presentation of diffuse light penetration in relation to the different source-detector separations. The source-detector separations are 0.5, 1, 2 and 3 cm respectively. Grey shaded areas indicate schematically the simplified presentation of the penetration (the light visitation probability) of diffuse light in relation to the different source-detector separations, simulated via a three-point green function method (please refer to the original publication for the details). Clearly, the signals from the large separations of 2 cm and 3 cm derive mainly from the muscle tissue whereas signals from 0.5 cm and 1 cm are mainly from upper layers. (Adapted with permission from [73]).

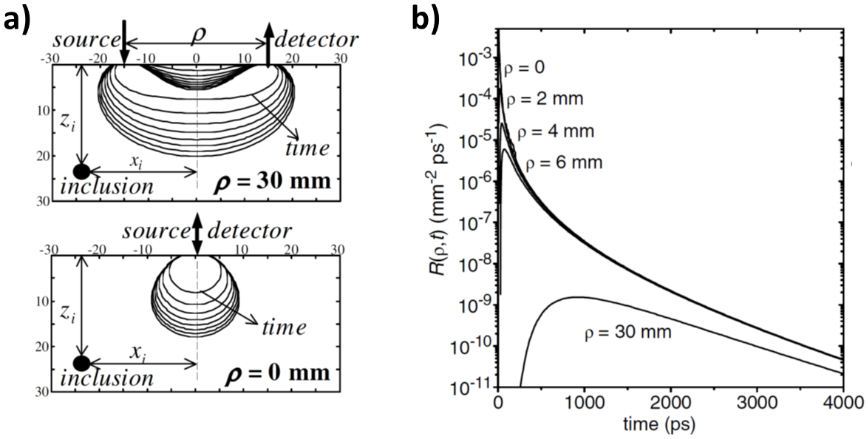

Figure 2.5: (a) Sensitivity profiles for 30 mm (top) and for the null-separation (bottom) in a homogeneous medium (μ_a=0.05 cm^{-1}, μ_s'=10 cm^{-1}, n=1.4) with an embedded simulated moving inclusion (absorption $\mu_{a(i)}$=0.2 cm^{-1}, scattering $\mu'_{s(i)}$=10 cm^{-1} and volume 1 mm^3). Each line represents the contour edge of the contrast at 4% of the maximum, at a given time-of-flight (only data from t in 0.5 to 4 ns, in 0.5 ns steps, are shown for clarity). (b) Time-resolved reflectance curve for small source-detector separations (0, 2, 4 and 6 mm) and for 30 mm in a homogeneous medium. (Adapted with permission from [74]).

Chapter 3

Time domain methods for blood flow estimation

This study has been carried out in collaboration with Dr. Sanathana Konugolu Venkata Sekar, Lorenzo Colombo, Dr. Alberto Dalla Mora, Dr. Alessandro Torricelli, Dr. Davide contini, Dr. Antonio Pifferi, Dr. Edoardo Martinenghi and Dr. Laura di Sieno from Politecnico di Milano (Milano, Italy) and was partially disseminated in peer-reviewed publications in Ref. [86] and Ref. [87], plus one in press ([88]) and in various conferences worldwide (ECBO 2017, Munich, Germany: invited oral contribution [89]; OSA 2018, Fort Lauderdale, Florida, USA: oral contribution [90]; ECBO 2019, Munich, Germany: oral contribution [91]).

The work presented in the last section has been made possible thanks to the collaboration with Ernesto Vidal Rosas from ICFO (Castelldefels, Spain).

3.1 Introduction

The combination of TRS and DCS can use the estimated local optical properties in the DCS fit to obtain absolute blood flow index and oxygenation values. This has been demonstrated in several studies [17, 18, 19, 20]. However, the proposed hybrid solutions so far use separate laser sources and detectors; the two techniques are made to work together by using optical filtering, with a consequent sub-optimal light collection efficiency, or using time-multiplexing, which reduces the sample rate. In addition to this, as described in [21, 17], continuous wave DCS and TRS have different penetration depths and sampling volumes, possibly resulting in partial volume effects that are difficult to correct and that depend on the optical properties and structure of the tissue being probed. The ultimate combination would be to utilize pulsed sources, similar to those used in TRS, to measure a path length resolved DCS signal.

Unfortunately, standard picosecond pulsed sources used as TRS sources have too low coherence lengths (ℓ_c) to be used as DCS sources. In reflectance geometry, typical tissue optical properties result in distributions of the path lengths that are much wider (in the order of 10 m). When ℓ_c is smaller or comparable to the span of photon path lengths, the signal-to-noise ratio is expected to decrease and the Siegert relation that relates g_1 to the measured g_2 has to be modified [26].

Time-bandwidth product acts as a physical limit on the compromises that can be accepted between short pulse duration and long ℓ_c. In the simple case of Gaussian temporal beam profile of FWHM Δt, being $\Delta \nu$ the FWHM bandwidth, it can be stated that

$$\Delta\nu\Delta t < \Pi \tag{3.1}$$

with Π a dimensionless constant called time-bandwidth product that depends on the characteristics of the laser. A Gaussian transform-limited (e.g. not chirped) pulse ($\Pi = 0.44$) of 10 ps has a bandwidth of *at least* 4.4 GHz. As large bandwidth is inversely related to ℓ_c, this corresponds to a ℓ_c at 785 nm wavelength of *at most* 22 mm. Compromises must be made in order to use the same pulsed sources for TRS (short pulse needed) and DCS (short bandwidth needed).

Just recently pulsed light DCS has been demonstrated to be feasible at relatively low source light levels [31]. In the cited work, a custom made two stage pulsed laser (150 ps pulse width, 150 MHz repetition rate, 6.5 mW power) and a prototype red enhanced single-photon avalanche photodiode (SPAD) were used in addition to a custom built time to digital converter (TDC) to select only portions of the photons arriving at the detector based on their time-of-flight. By selecting (gating) photons in a narrow (48 ps) window (gate) of arrival times with respect to the laser pulse clock (time-of-flight), the span of photon path length in a gate is reduced and some signal-to-noise ratio of the intensity autocorrelation can be recovered, even if the coherence length of the pulsed source is limited by the time-bandwidth product and by other factors. Signal-to-noise ratio is proportional to the value of intensity autocorrelation at zero lag time, or β, that is in fact expected to increases when the gate width decreases. More recently commercial sources and detectors have been used as reported in [92].

As an experimental strategy, the use of a pulsed but yet sufficiently coherent laser would allow using broader gates and this in turn increasing the photon count rates at each gate; signal-to-noise ratio of the estimated autocorrelation curves can therefore be increased, allowing faster time resolution TD-DCS that until recently hindered important *in vivo* applications in humans.

Searching for a compromise between the pulse duration and coherence length it should be taken into consideration that broad pulses, other than degrading the capacity of accurately estimate the optical properties as happens in TRS, limit in a sense the use of narrower gates as they mix photons with different times-of-flight in a similar fashion to when using high timing jitter detectors.

Another approach is to use interferometric techniques that can measure the scattered electric field autocorrelation function by sweeping the source wavelength in time, as initiated by the work of Tualle *et al.* [93, 94] and recently demonstrated *in vivo* on small animals in [95]. Although its apparent convenience, the practical *in vivo* translation is complex.

In this chapter I describe how an experimental setup based on a pulsed yet highly coherent active mode locked laser and a novel acquisition scheme, based on broad, hundreds of picoseconds time-of-flight gates, allowed for the first time *in vivo* human measurements of cerebral hemodynamics and of fast-changing blood flow in a arm cuff occlusion experiment with 1 s resolution. Beside proving that the TD-DCS technique allows to retrieve optical properties (μ_a and μ_s') and to enhance the depth sensitivity, I also show that blood flow can be measured at very small, ideally null source-detector separations. I present this as a consequence of independence of path length distribution from source-detector separation that is proper of time domain methods (see section 2.1.4). Finally, I show how the discussed technological improvements can be applied to speckle contrast optical spectroscopy (SCOS), achieving time domain SCOS for the first time. This latter technique has many potential advantages that I discuss thoroughly in the last section.

3.2 *In vivo* time domain diffuse correlation spectroscopy

3.2.1 Improvements to the state-of-the-art

Previous state-of-the-art TD-DCS setup [30, 31] did not have sufficient signal-to-noise-ratio for fast (seconds) acquisition of *in vivo* measurements. Using a pulsed yet highly coherent active mode locked laser as the light source it was possible to make use of broader (hundreds of picoseconds to nanoseconds) time gates, allowing breaking the signal-to-noise ratio barrier and demonstrating the usefulness of TD-DCS *in vivo* in humans for the first time.

Three main benefits of the TD-DCS approach are foreseen, with respect to CW-DCS, when applied *in vivo* are:

1. the simultaneous estimation of optical properties and blood flow offers a more complete picture of the hemodynamic processes investigated;
2. the selective use of deeper reaching photons signal, depth sensitivity is achieved in a way that is less sensitive to the confounding heterogeneity of the probed tissue at a macroscopic level as would happen in a CW multi source-detector separation approach [96, 61];
3. the disentanglement of the separate contributions of i) the time-of-flight distribution in tissue and ii) the flow of red blood cells to the estimation of absolute BFi from the decay of g_1 curves is achieved in a physically elegant way expressed by eq. 2.12.

I demonstrate these points first on phantoms and then on the head and arm of healthy subjects when blood flow is (reversibly!) hindered by applying superficial pressure to the area being probed on the head or by occlusion of afferent arteries by the inflation of a arm tourniquet.

3.2.2 Methods

Instrumentation

Figure 3.1 shows the experimental setup of the TD-DCS experiments described in the present section. The instrumentation comprised the laser source, a detector with its associated timing electronics and correlator, and the fibers used to guide light.

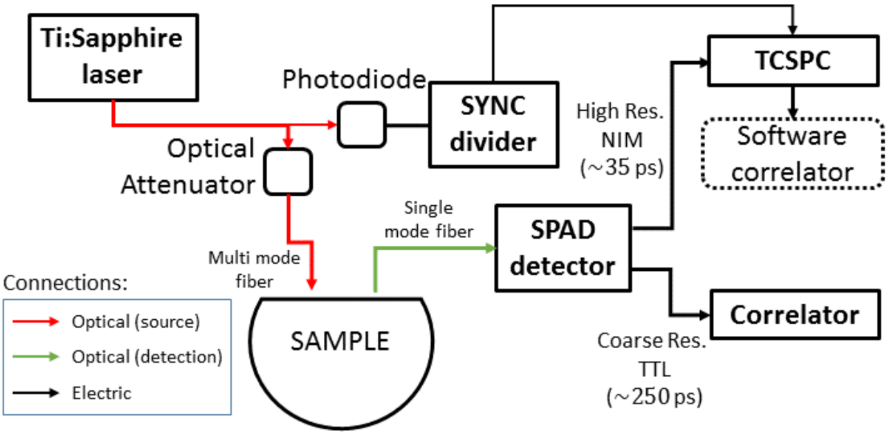

Figure 3.1: The sketch of the experimental setup for the TD-DCS system (adapted with permission from Ref. [86])

The laser source was a custom made [97, 98] active mode locked titanium-sapphire laser (Ti:Sa) operated at 785 nm, pulse repetition frequency of 100 MHz, and a variable pulse width (FWHM) that for the experiments described here was in the range between 100 to 350 ps, depending on the carrier number and cavity offsets, which I estimated from the FWHM of the system IRF. An acousto-optic modulator in the laser cavity allowed phase locking of longitudinal modes, leading to a high temporal coherence characteristic of the beam. Population inversion was achieved by pumping the lasing crystal with a 5 W frequency double continuous wave Nd:YAG laser. A small fraction of the Ti:Sa beam ($< 5\%$) was split off by a pellicle beam splitter and detected by a photodiode (OCF-401, Becker & Hickl, Germany) that generated an electronic synchronization signal (SYNC), periodic, and with the same period of the laser pulse. A fast active comparator circuit (SYNC divider), developed in house, removed one pulse every two or three, depending on the experimental needs, thus decreasing the frequency of the synchronization signal. At 100 MHz in fact the SYNC rate would have been too high for the timing electronics (time-to-digital converters or time correlated single photon counters) or time-gated detectors like the one used (see below). The rest of the light was attenuated with a stack of three metallic variable attenuators, cleaned by passing through a ~3 mm wide adjustable size aperture iris, and launched into a 3 m length, 200 µm core diameter, step index fiber (WF200, Ceramoptec, USA) by using a F280APC-780 fixed-focus collimator (Thorlabs, USA). Prior to the measurement, the attenuator was set to reduce the output light at the sample-facing tip of the multi mode fiber below skin maximum permissible exposure (MPE) according to ANSI Z136.1.

The light was collected at a variable distance depending on the experiment by a single mode fiber (780HP, 4.4 µm core diameter, cutoff wavelength 730 nm, Nufern, USA) and detected by a single photon avalanche diode (SPAD, PDM model, Micro Photon Devices, Italy).

The photon detection efficiency was estimated to be about 20% at the wavelength of 780 nm. The detector had two outputs: one was a high detection timing precision, nuclear instrumentation module (NIM) output, with nominal timing precision of 35 ps, while the other was a coarser precision, transistor-transistor logic (TTL) output, with few hundred of picoseconds timing precision.

A time correlated single photon counting (TCSPC) module (Pico Harp 300, PicoQuant, Berlin, Germany) was connected to the NIM output of the SPAD and to the timing electronics SYNC after it was processed by the divider. The TCSPC card, however, could process SYNC inputs up to a maximum frequency of 84 MHz. For this reason only a pulse every three was accepted by the SYNC divider. The TCSPC recorded on a file on a Windows computer a detection "time stamp" for each photon that was detected. Each photon time of arrival and delay with respect to the last SYNC signal could be extracted from the time stamps. The timing resolution of this photon counting card is 8 ps. I used a Windows 7 PC and the Picoquant instrument GUI to carry out the acquisition in the T3 mode generating a `.ptu` file for every experiment (8 in total).

An electronic 8-channel USB correlator (Flex-05, Correlator.com, USA) was connected to the coarse (~250 ps) precision TTL output of the SPAD and used to independently compute ungated intensity autocorrelation function to be stored in a control Windows PC. During some of the experiments, 1 s resolution acquisition of the USB correlator was manually synchronized with the PH-300 acquisition.

The overall IRF of a time domain spectrometer, as in TRS, can be computed by producing the histogram of the times-of-flight directly connecting the source and detector fibers [99]. As in TRS, a thin scattering layer, like for example paper [99] or polytetrafluoroethylene tape (Teflon), was placed between source and detector multimode fibers. The IRF was then acquired by facing the source and the detector fibers directly in front of each other with a sub-millimeter thick Teflon sheet in between and integrating for 30 s. The full width at half maximum (FWHM) of the IRF was about 100 ps.

Phantom preparation

A two layer liquid phantom container was built by separating two water-tight compartments, identified as superficial (S) and deep (D). They were separated by a 50 µm thick semi-transparent Mylar sheet (RS components, Spain), a solution that has been previously proposed when containment of some liquid phantom was needed [100]. Another Mylar sheet window separated the S compartment from the outside. Optical investigation of both compartment was possible through it (see fig. 3.2). The thickness δ of S was varied with a precision micrometer screw mechanism in order to reproduce different superficial tissue thicknesses. Two different Lipofundin[1] (B. Braun Melsungen AG, Germany) based water solutions were mixed, one with 6.5% and one with 13.5% (weight ratio) concentrations of Lipofundin. Since the goal was to create a contrast in the diffusion dynamics of the scatterers, I added pure glycerol (Sigma Aldritch, USA) to the second, which has the effect of decreasing the Brownian diffusion coefficient D_B of the light scattering droplets in Lipofundin. Despite the decrease of the solute/solvatant refractive index mismatch would bring down the μ_s', the higher concentration of Lipofundin exactly compensated for this effect as it was described in [102]. The two phantoms were tested for having the same optical properties by fitting their measured DTOFs with

---

[1] Lipofundin is an emulsion of fat droplets in water that is widely used as the scattering part in water-based liquid phantoms for diffuse optics. It is an alternative of the better known Intralipid [101].

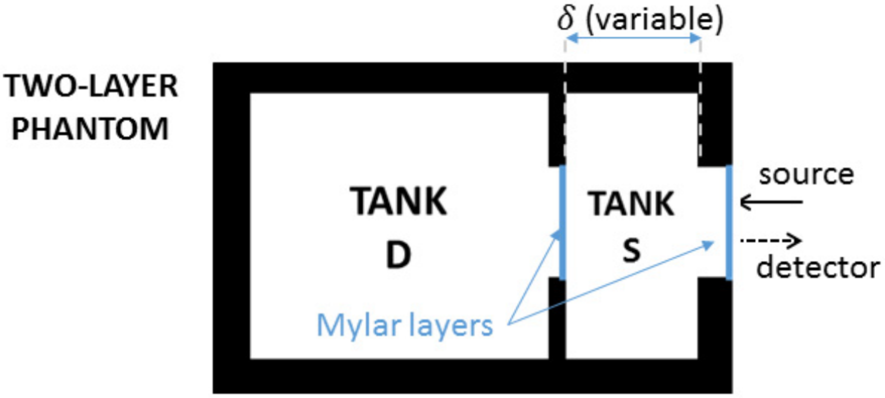

Figure 3.2: Sketch of the two-layer liquid phantom holder. δ is the thickness of the superficial layer S. This is a schematic representation therefore not in scale. (Adapted with permission from Ref. [86])

the convolution of the IRF and the reflectance solution of the photon diffusion equation in reflectance geometry [68, 69]. I estimated that having a 30% concentration of glycerol in the second phantom determined a 40% lower D_B. In a first step, both compartment were filled by the pure Lipofundin/water solution (I call this condition *dynamically homogeneous*, or *DH*), and the height of S varied in δ=5 and 10 mm. By replacing the content of the S compartment with the Glycerol/Lipofundin/water solution, *dynamically heterogeneous* case or *DA* was produced. In this case the height of S was varied to δ=5, 10 and 15 mm. I carried out a measurement for each of the five configurations (two *DH* and three *DA*) by acquiring a total of about 4×10^8 photons per measurement at 15 mm source-detector separation.

In vivo experiments

A healthy human subject (male, 30 years old) with no history of neurovascular diseases was recruited for the two protocols (head and arm). The protocol was approved by the Ethical Committee of Politecnico di Milano and experiments were conducted in agreement with the Declaration of Helsinki. The subject signed a written consent before his participation.

Head The subject was instructed to lay on a bed, supine, and to remain alert during the whole experiment. The location being probed was a portion of the forehead, far from the midline and on a relatively flat region. A $5 \times 5 \times 5\,\mathrm{cm}$ black plastic fiber holder, which hosted source and detector fibers and kept them 10 mm apart and pointing perpendicularly on the skin was placed on this location. During the first trial (control), the holder was secured to the head by encircling both with a cotton mesh wrap. In the second trial, pressure was manually applied by the experimenter by pushing the probe to the surface of the head up to the maximum pressure the subject was comfortable with. In this way I tried to reduce by compression the blood flow in the tissue above the skull (scalp), as shown in [103, 104]. For each pressure scenario (pressure and control), I acquired up to a target of 2×10^7 photons or 300 s.

Arm The same source detector separation was used for measuring the BFi on the arm before, during and after occluding the afferent arteries by inflating a tourniquet of a manual sphygmomanometer at 180 mmHg, well above the subject's systolic blood pressure. The black plastic holder with the fibers of the head measurement was placed above the brachioradialis muscle in the right arm and was secured with a loose bandage. The tourniquet was placed right below the shoulder joint of the same arm. The cuff occlusion started 245 s after the start of the measurement and lasted 180 s. In order to resolve hemodynamic changes in time, after collecting 600 s I divided the period into smaller 1 s parts that I analyzed separately. One of the USB correlator channels was connected to the TTL output of the SPAD to acquire ungated autocorrelations every second. It was started at the same moment of the start of the TCSPC acquisition.

Data analysis

The time-of-flight (t') of each detected photon was computed by subtracting the time at which the IRF has a peak (t_0), measured during calibration, from the delay time that is available from each time stamp. As a consequence of the introduction of a divider circuit, photon time delays could span three laser repetition periods ($3 \times 10\,\mathrm{ns}$). To correct for this effect in the analysis I transformed the delay time by applying a modulus operation with respect to the laser period. Delay time and laser period were rounded to the nearest 8 ps TCSPC channel.

Gated autocorrelation was achieved by classifying the time tags according to their time-of-flight. Limiting i.e. the autocorrelation or the binned intensity computation analysis to a time-of-flight gate $[t'_A, t'_B]$ means that only the time stamps with t' that falls between the extremes of the gates should be considered. Both the intensity autocorrelation and binned intensity were estimated by processing only the photon arrival times t stored in the time tags that belonged to a certain gate. Carrying out computations on a gate that extends between $-\infty$ and ∞ is equivalent to carrying out a ungated CW-DCS analysis.

Intensity autocorrelation function $g_2(\tau)$ was computed from the arrival times t by modifying the FoCuS-point correlator [105], which, in turn, is based on the relatively fast algorithm for photon autocorrelation described in Wahl *et al.* [106]. The notable modifications I carried out were meant to control the spacing of the autocorrelation time delay τ, to allow time-of-flight gating, and to control the time resolution of the measurements. The binned intensity is computed by building the histogram of the photon arrival times according to some selected gate and resolution that are detailed in the following paragraph for each experiment.

Pine *et al.* [30] first proposed in the context of diffusing wave spectroscopy that a model for the electric field autocorrelation function measured in a gated, pulsed diffusing wave spectroscopy (DWS) experiment, is given by the integral of the single photon path length autocorrelation function, weighted by the probability of that path length to be present among the detected photons. Assuming the Siegert relation to be valid and the sample to be homogeneous in terms of its refractive index n, which allows a linear relation between time-of-flight t and path length $s{=}c/nt'$, a model for the intensity autocorrelation is proposed:

$$g_2(\tau, \hat{k}) = 1 + \beta \left| \int_{t'_A}^{t'_B} P(t')\, exp(-\hat{k}t'\tau)\, dt' \right|^2 \tag{3.2}$$

In this equation, $P(t')$ is the distribution of times-of-flight t' in the sample, $[t'_A, t'_B]$ is the time-of-flight gating interval, and the exponential function is the electric field autocorrelation for a single path length in tissue. Following the approach in [30] the probability distribution $P(t')$ is for these experimental conditions the diffuse reflectance $R(t')$ of eq. 2.9. The decay rate for a single time-of-flight $\hat{k}$ is

$$\hat{k} = 2\mu'_s \, \frac{c}{n} \left(\frac{2\pi\, n}{\lambda} \right)^2 \alpha D_B \tag{3.3}$$

where D_B is the Brownian diffusion coefficient of the light scatterers and α is 1 in phantoms, while it is usually fitted together with D_B (αD_B=BFi) *in vivo*. With respect to path length s, k is used to denote the autocorrelation decay ($\hat{k} = k\ c/n$).

Fitting of the measured autocorrelations was carried out in Matlab v2017b (Mathworks Inc, USA) with the `fminsearch` function using as an objective function the square of the residuals between the data (autocorrelation estimated by the software correlator) and the model. I used different models, depending on the time-of-flight gate width:

- in case of *broad* gates, I fitted a numerical estimation of equation 3.2, with $P(t')$ being the solution of the diffusion equation for semi-infinite sample geometry and extrapolated boundary conditions [68, 69], computed for the measured or known $\mu_\mathrm{a}$and μ_s', to the gated measured intensity autocorrelation data;
- for gates that are *narrow* with respect to the decay of $P(t')$, as proposed initially by [31, 30], $P(t')$ can be assumed constant and the integral dependence of equation 3.2 drops. In this case, exponential functions can be fitted to the autocorrelation of each gate with respect to τ, obtaining kt_i' with $t_i' = (t_{i,B}' - t_{i,A}')/2$ the average time of the i-th small gate $[t_{i,A}', t_{i,B}']$. A linear fit of kt' with respect to t' yields the estimate of BFi=αD_B as from equation 3.3.

In the first case, as shown in [86], directly fitting the intensity autocorrelation g_2 data allows to retrieve BFi along with β [107], instead of estimating it from the intercept of g_2 curves at τ=0 that, especially for late gate and due to the low probability $P(t')$, tends to be rather noisy.

The ungated intensity autocorrelation curves acquired with the USB correlator, when it was used, were fitted with the CW-DCS theory [5].

Optical properties of the two liquid phantom preparations (with and without glycerol added) were measured for few seconds to measure the distribution of times-of-flight (DTOF, shown in fig. 3.3) from which, with a standard TRS procedure, the optical properties were determined by fitting it to a convolution of the IRF and the semi-infinite solution of the diffusion equation for extrapolated boundary conditions.

Here I considered narrow (160 ps) and broad (0.8 to 3 ns) gates. Using the latter allow increasing the count rate, and therefore the signal-to-noise ratio of the autocorrelation curves. For this reason, broad gates allow also faster measurements compared to the narrow gate case. Broad early gates are selected starting from the peak of the IRF up to the point at which the DTOF has decayed to 90% its peak value towards positive times-of-flight (falling edge). Broad late gates extends from this point up to when the DTOF is no longer distinguishable from the noise floor, for a total width of 2 to 3 ns, depending on the optical properties and on the source detector separation. Narrow gates are used only in the phantom assessment; narrow gate width is a compromise between count rate and β value obtained. Consecutive narrow gates overlap by half their width (80 ps).

3.2.3 Results

Depth sensitivity in phantom

The reduced scattering coefficients were $10.6\,\mathrm{cm}^{-1}$ for the phantom with 30% added glycerol, and $10.5\,\mathrm{cm}^{-1}$ for the phantom without glyc-

	NARROW GATES		BROAD GATES	
δ	EARLY	LATE	EARLY	LATE
5 mm	52%	100%	47%	100%
10 mm	36%	71%	34%	84%
15 mm	28%	50%	28%	61%

Table 3.1: Relative D_B when S layer is filled by 30% glycerol-added phantom (DA), for changing S layer thickness δ, compared to the late gate or gates when $\delta = 5\,\text{mm}$ (100%).

erol. Absorption coefficients were 0.025 and $0.026\,\text{cm}^{-1}$, respectively, compatible with water absorption at that wavelength [108].

For narrow gate analysis I have identified two regions, early and late, reported in fig. 3.3 as shaded areas. The decay constant ks of the narrow gate autocorrelation with respect to the delay time τ increases at later gates. I believe that the non linear behavior before the green shaded region (s <70 mm) is due to contributions of the finite IRF, of non-diffusive photons, and of the noise associated to the finite gate width. On the other side, for late gates outside the orange shaded area (s >500 mm), few photon fall into a narrow bin therefore the noise of the autocorrelation becomes important. The linear coefficient k becomes significantly affected, by substituting the superficial layer with the phantom that has reduced scatterers Brownian motion, i.e. during the transition between DH and DA. Notably, the D_B that was retrieved from the linear fit of k in the two shaded regions drops as the thickness of the superficial compartment δ is increased (see table 3.1).

Autocorrelation estimated in the two broad gates was also numerically fitted with the method described in section 3.2.2. All D_B values changes are relative to the DA late gate at smallest superficial thickness (100%).

Cerebral BFi measurements

Figure 3.4 reports the results of *in vivo* head measurement when the hemodynamics of the layer above the skull is altered by manually compressing it, a measurement that has been recently been repeated in [92]. In the figure, g_2 curves for early (β=0.41), late (β=0.25) and ungated (β=0.29) case are shown, and a 90 kcps at 1 cm source-detector separation was achieved in both cases. Analysis of the ungated case showed that the BFi decreased by 61% when pressure was applied.

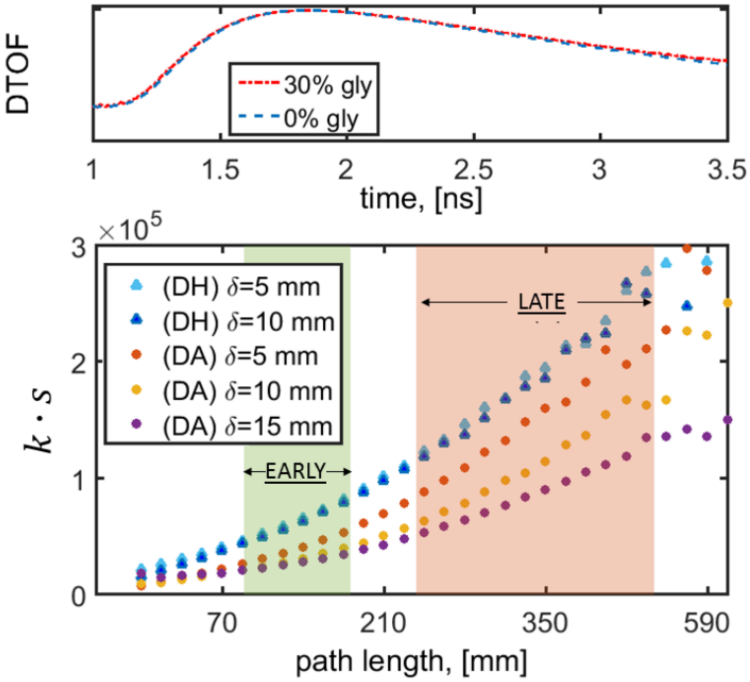

Figure 3.3: (Top) DTOF curves of the two homogeneous liquid mixtures, with (30% gly) and without (0% gly) glycerol. No difference is evident as the optical properties of the two phantoms are almost identical. (Bottom) Narrow gates autocorrelation decay rates (ks) for the DH (circles) and DA (triangles) two-layer phantom configurations. (Adapted with permission from Ref. [86]).

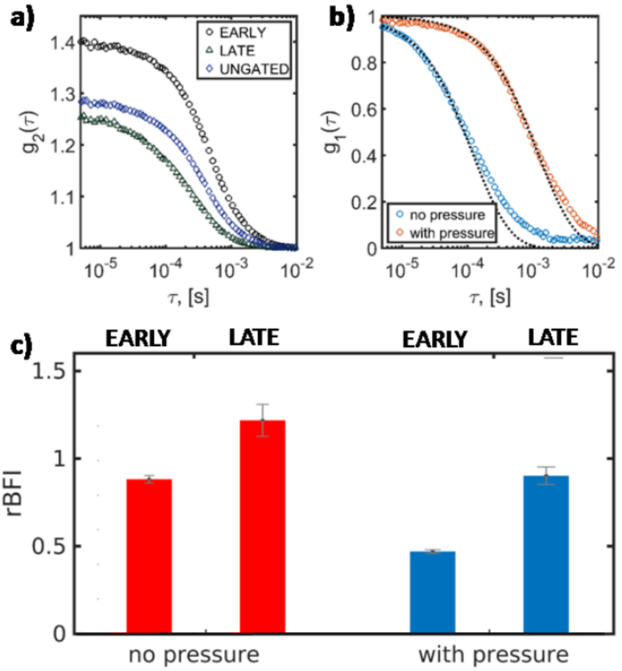

Figure 3.4: (a) Intensity autocorrelations of the early and late gates, and the ungated case, in the control condition (no pressure applied) for the head experiment. (b) Electric field autocorrelation for the early gate when pressure is applied on the probe compared to control. The distortions from the model at late lag times are a common feature of *in vivo* DCS data as illustrated in [5], see fig. 8 therein. (c) Relative BFi with for the early and late gates and the two conditions (no pressure, with pressure) is shown. For each condition, the BFi is normalized by the ungated control condition value. (adapted with permission from Ref. [86])

Arm cuff hemodynamics

Figure 3.5 summarizes the measured BFi changes relative to the first 100 s baseline during the various stages of the arm cuff occlusion. Measured g_2 curves are not shown (average β was 0.36 and 0.32 for early and late broad gates, respectively). In both BFi time series the decay following cuff occlusion, the hyperemia and the recovery are well visible, as well as with the ungated case (continuous line), that was acquired using the Flex-05 correlator. All three traces are very close to each other. The superficial thickness above the muscle, estimated with a skin caliper after folding the skin and fat, was 2.5 mm.

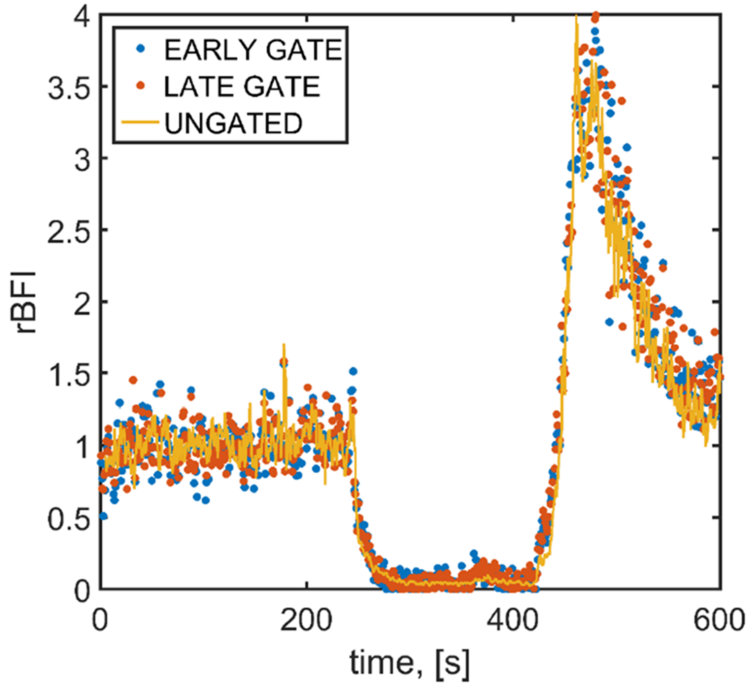

Figure 3.5: Relative BFi (normalized to the first 100 s) during the arm cuff occlusion experiment, broad early and late gates (dots, 1 s resolution) and represent the broad gates analysis (continuous line, 1 s resolution). The continuous line is the rBFi estimation from ungated analysis carried out with the hardware correlator (1 second resolution). (adapted with permission from Ref. [86])

3.2.4 Discussion

In the phantom measurements, achieving the same optical properties in the two compartments means that the contrast is entirely due to the different viscosity that affects D_B. Using narrow gates it is evident how increasing δ does not change the slope of k in the DH case. On the contrary, using narrow and broad gates and comparing to the ungated case, I have shown (see fig. 3.3 and table 3.1) that the decorrelation of the earlier gates is slower when I increased δ in the DA case.

Slower decay of the early gate (superficial tissue) is also evident on the head when I applied pressure, compared with the control condition, when no pressure was applied. Compression does not in fact affect the deeper brain tissue, which is protected by the hard skull bone [14, 103].

Both phantom and head experiments show the usefulness of the technique to enhance the depth sensitivity of BFi measurement, reducing the partial volume effect described in section 2.1.4 from the superficial layer.

Intensity autocorrelation (g_2) curves on the head appear to be well differentiated among the various gates in the control condition, when no pressure is applied from outside. Despite changes in the optical properties that shall take place when compressing the superficial tissue with respect to the control condition (not estimated), β scales as expected between early, late gates and the ungated case (fig. 3.4, a), and the count rate is not significantly affected.

Surprisingly no difference is seen between the measured relative BFi in the early, late gates, and in the ungated case. This is unexpected because, due to the higher oxygen consumption of the deep muscle tissue, which is more metabolically active and reactive than the more superficial skin and fat layers, a higher hyperemic peak in the late gate was expected [73]. I attribute this behavior to the thinness of the superficial tissue measured by the skin caliper for this particular subject (2.5 mm).

In all the experiments I have reported, the absolute values of β are sistematically higher than ones reported in ref. [31], and also than in the more recent example given in ref. [92]; this is evident, for example, by comparing the values obtained in the experiments on the head. Cleaner spectral content of our laser is speculated to be the reason; pulsed light from our source is closer to be bandwidth-limited due to the tunable active pulse locking.

3.2.5 Limitations and outlook

I have not reported many possible combinations of changes of dynamics and optical properties in a two layer media. Moreover, the choice of only two broad gates, or conceptual separation of narrow gates into earlier and later sounds quite arbitrary: sets of numerous time gates are commonly used in TRS [109]. However, this work is meant to establish the proper experimental and theoretical framework under which a more careful characterization of the depth sensitivity enhancement, and how dynamical and optical properties contrast between layers affects this enhancement. Recently the effects of instrument precision have been taken into account, independently, by [110, 111]. Accounting for the effect of a non-null IRF and coherence length comparable to the span of photons within a gate is not carried out here, but it is strongly advocated and it is even unavoidable when one want to deal with absolute values of BFi.

Independently from the above mentioned corrections, some works suggest [27, 112] that the Siegert relation might not be valid when the coherence length of the source is in the order of the distribution of photon path lengths in tissue, or even shorter. Here I have demonstrated that this relation still allows us to extract meaningful values of BFi from in vivo experiments. Sutin et al. [31] have justified the application of the Siegert relation saying that it only apply to small gates: however, in a recent publication [92] they estimate the coherence length of their laser used in 2016 to be less than 5 mm, corresponding to a coherence time of 24 ps, which is even smaller than the 48 ps narrow gate width they used on phantoms. I believe that the greater coherence length of our system allows to avoid most distortions due to the non-ideal conditions when working with broader (up to 1 ns) gates. No evidence of distortions like for example the intensity autocorrelation curves not decaying to one at infinite time were observed.

3.3 Time domain diffuse correlation spectroscopy at short source-detector separation

The time-domain approach is beneficial since it increases the sensitivity of DCS to deep blood flow. Using a finite, non-null source-detector separation, i.e. a physical separation that can be up to tens of millimeters, results in a sub-optimal photon collection efficiency [16]. The probability of light traveling from the source to the detector decreases as their distance on the surface of a turbid medium increases. In continuous wave DCS [14] and NIRS [113] source-detector separations in the order of centimeters are the only way to probe photons with longer times-of-flight, as the peak of the DTOF shifts towards later times [15], therefore towards longer path lengths.

However, despite the fact that source-detector distances reduced to minimum can result in very thin probes, in an increase of the count rate at any gate, and in the maximization of the spatial resolution of the measurement, sub-diffusive photons with very short time-of-flight are also orders of magnitude more numerous [75, 114]. As they carry information mainly from the shallowest layers of the probed tissue, they are not usually of interest in many non-invasive applications, they are actually generally considered a nuisance, since they tend to saturate detectors and time tagging electronics. In order to profit for the benefits of operating at the shortest possible source-detector distance, the selective gating of the long time-of-flight, deep-reaching photons has to be carried out at the detector level [115]. If this is achieved, the short separation approaches can provide performance advantages in signal-to-noise, spatial resolution and probe ergonomics, as discussed above. The shape of sensitivity volume of the shortest (null) separation approach has been recently reviewed for TRS in [13], while ergonomics is discussed also in [116].

In TRS, null source detector separation measurement have been successfully carried out using fast gated SPAD (fgSPAD) detectors [75]. These are solid state single photon counting detectors whose sensitivity to light can be switched on and off (i.e. they can be gated) for few nanoseconds, with a rather short transition time of hundreds of picoseconds, during every laser pulse period [117]. Gating start time is easily adjustable with respect to the pulse time with a great finesse by electronically delaying the synchronization signals. By switching the detector on only during the arrival of the late, long time-of-flight photons, it is possible to neglect the early photons, solve the dynamic range issue, and operate the instrument at a virtually null source-detector separation. When computing intensity autocorrelation functions, as in DCS, time-tagging each photon, e.g. with a time-correlated single photon counter, is no longer needed; off-the-shelf correlators as Flex-05 can be used in real time, resulting in a simplification of the experimental setup and analysis.

In the following section I describe a quasi-null source detector separation measurements of the blood flow during arm cuff occlusion in a healthy subjects. These findings follow from the work reported in ref. [87].

3.3.1 Methods

The source described in section 3.2.2 was used, although at a slightly different set point that resulted in a longer pulse, but also in an increase output intensity and stability; coherence length also was likely to be increased as heuristically proven by having higher β in phantom (data not shown) and *in vivo* (see below) experiments.

On the detector side, two single mode fiber (780HP, 4.4 µm core diameter, cutoff wavelength 730 nm, Nufern, USA) collected light from the sample, one at 12 mm and the other at 2.85 mm distance from the source fiber, a 3 m length, 200 µm core diameter step index multimode fiber (WF200, Ceramoptec, USA). The smallest source-detector separation, from here on called quasi-null separation, was the smallest possible distance allowed by the physical dimension of the ferrules of the two fibers.

For the larger source detector separation, the single mode fiber was coupled to a SPAD detector module (PDM model, Micro Photon Devices, Italy). This SPAD was used in free running mode, i.e. it was not gated. One of its output, the coarse resolution TTL, was connected to one of the 8 channels of the hardware USB Flex-05 correlator. The fiber at quasi-null source detector separation was coupled instead to a fgSPAD, developed in house [117], with a 100 ps nominal timing resolution. It was gated in synchronization with the source SYNC signal. Since the maximum gating frequency allowed by this fgSPAD is 50 MHz, a fast divider circuit was deployed in order to accept only one pulse every two through the SYNC line. One of the detector output was connected to the TCSCP (PH300, the same used and described in 3.2.2), while the other to one of the available channels of the Flex-05 correlator. A low voltage transistor-transistor logic (TTL) translation stage, built using standard components, was used to invert and amplify the nuclear instrumentation module (NIM) output of the fgSPAD to make it compatible with the USB correlator. The original NIM output was supplied, along with the source SYNC on a separate channel, to the TCSPC.

The fgSPAD gate was set to 4 ns width and synchronized with the laser pulse frequency. I defined the delay between the start of the fgSPAD gate and the pulse emission Δt_0=0 when it is made to coincide with the peak of IRF, measured by facing source and detector fiber with a thin (<0.2 mm thick) diffuser in the middle. In the arm cuff experiment Δt_0=512 ps was set.

USB correlator was managed by an *ad hoc* interface written in C on a Windows PC and autocorrelation curves for both the active channels were computed and saved every 2 s. The TCSPC data was processed with the software correlator generating a curve very 2 s.

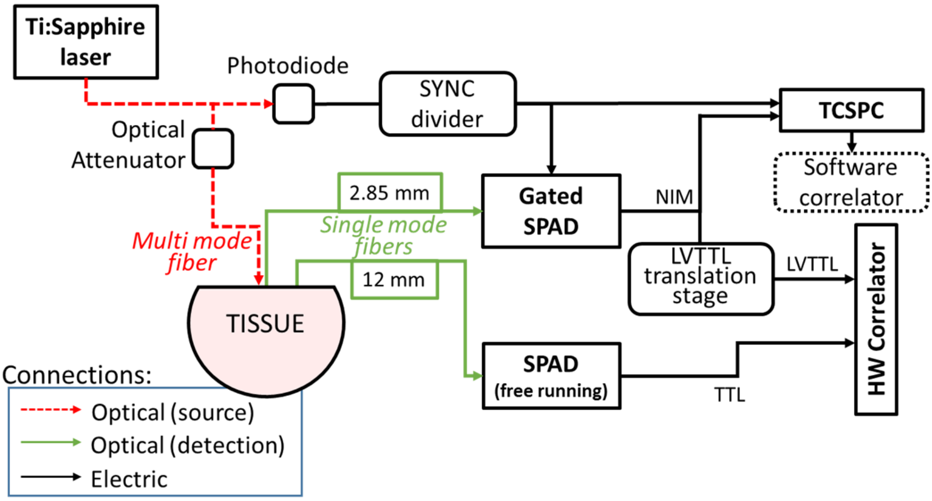

Figure 3.6: Sketch of the experimental setup. (LV)TTL: (low voltage) transistor-transistor logic; SYNC: synchronization; NIM: nuclear instrumentation module; TCSPC: time correlated single photon counter. (Adapted with permission from Ref. [87]).

The probe was made of a black foam matrix. The detector fiber tips were separated by ρ= 12 mm or ρ=2.85 mm (quasi-null-separation). I placed the probe gently on the brachioradialis muscle of a healthy subject (female, 26 years old). The superficial (skin and fat) thickness was measured with a plicometer and was 13 mm. After three minutes of baseline measurement, the tourniquet, placed right below the shoulder joint, was inflated up to a pressure of 180 mmHg, well above the arterial pressure of the subject, and was released after 3 more minutes have passed. The protocol was approved by the Ethical Committee of Politecnico di Milano and was conducted in agreement with the Declaration of Helsinki. The subject gave written consent before participation.

Data analysis

Electric field autocorrelations g_1 were recovered using the Siegert relation from the measured intensity autocorrelations g_2. The three time series of measured curves were fit to the numeric evaluation of the same theoretical model used for TD-DCS, in the following form

$$g_2(\tau) = 1 + \beta \left| \int_{\Delta t_0}^{\infty} P(t',\, \rho)\, exp(-\hat{k}t'\tau)\, dt' \right|^2 \tag{3.4}$$

where the theoretical time resolved diffuse reflectance $P(t',\, \rho)$, for the correct source-detector separation ρ, is computed according to [68] for the optical properties that are estimated through a TRS fit of the 12 mm channel DTOF. Gate delay Δt_0 was either $-\infty$ or 512 ps for the time series in which ρ was 12 or 2.85 mm, respectively.

3.3.2 Results

Optical properties of the arm at the measurement location were estimated to be μ_a=0.14 cm^{-1} and μ'_s=10.3 cm^{-1} from the TRS fit of the DTOF of the 12 mm channel at rest, prior to the experiment. Figure 3.7 reports the measured IRF (orange line, FWHM 350 ps) of the quasi-null-separation channel. I measured the effective width of the gate to be 4 ns between rising and falling edge, defined at $^{1}/_{10^4}$ of the maximum. After measuring the IRF in the quasi-null channel, the gate was adjusted by setting the delay Δt_0 to 512 ps.

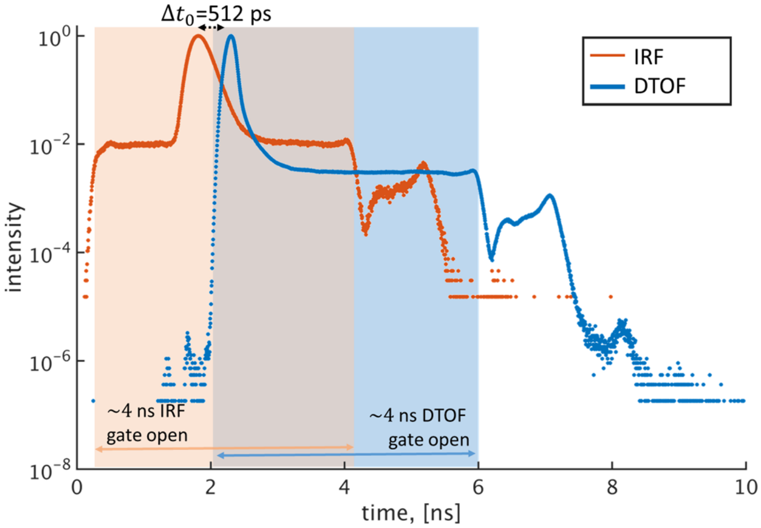

Figure 3.7: IRF of the system (orange line) and a typical distribution of photon times-of-flight (DTOF, blue line) detected by the fgSPAD at quasi-null-distance (ρ=2.85 mm) on the arm during the baseline period. (Adapted with permission from Ref. [87]).

The experiment lasted 660 s. A total of 2.5×10^8 photons were collected by the quasi-null separation fgSPAD, as measured by the TCSPC, which corresponds to an average count rate of 379 kcps. This value is well within the dynamic range of either the detector, the TCSPC, and the hardware correlator. At the larger distance, an average of 228 kcps was recorded. The electric field autocorrelation curves computed from the quasi-null separation channel data, acquired by the fgSPAD, are shown in Fig. 3.8. I have reported three pairs of curves in total, one for each period of the occlusion (namely baseline, occlusion and hyperemic peak); in each pair, one curve was estimated by the software correlator from the TCSPC recorded time-tagged data and one by the hardware correlator. The observed differences were minimal and compatible with the different lag time spacing architecture of the HW and SW correlators, and with the time difference between the acquisition of the two curves ∼1 s (the intrinsic temporal resolution of the measurement). The values of the intercept β of the intensity autocorrelation curves (not shown) were on average 0.26 ± 0.03 for the gated quasi-null-separation and at 0.21 ± 0.02 for the ungated long separation.

I have reported the relative BFi (rBFi) estimated by fitting the HW correlator data in fig. 3.9. BFi is normalized to the first 40 s (baseline, 100%). Two lines are reported: the orange one is the quasi-null-separation, while the blue is the free running detector channel at 12 mm, that is reported as a reference. The features of the baseline (0 to 180 s), occlusion (180 to 360 s) and the hyperemic peak (360 to 420 s) were well evident and corresponded to large differences in the rBFi, as expected from the literature [73].

By fitting an exponential decay $\sim exp(-t/t_0)$ to the BFi decrease right after the hyperemic peak (400 to 500 s), the gated quasi-null separation BFi time series was found to decrease with a decay constant t_0 (1.5 %/s) approximately double than the in the ungated 12 mm case (0.7 %/s).

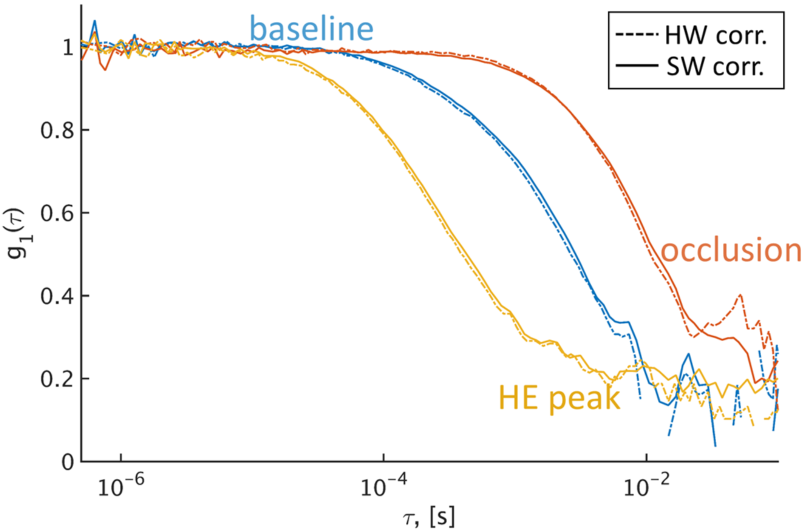

Figure 3.8: Typical electric field autocorrelation (g_1) curves computed from the gated, quasi-null-separation sensor from the hardware (HW, dashed line) and software (SW, solid line) correlators. Three periods are shown at the baseline (blue), the occlusion (red) and the hyperemic peak (HE, yellow). (Adapted with permission from Ref. [87]).

3.3.3 Discussion

Here, by setting a delay Δt_0 of 512 ps to the gated detector operating at a very short, quasi-null separation of 2.85 mm, the short path length photons were rejected, thus limiting DCS data analysis to the set of photons with path lengths longer than $c/n\ \Delta t_0 \simeq 11$ cm.

The intensity autocorrelation decay for the light that has traveled through blood perfused living tissue was successfully measured out at ideally null separation between the source and detector for the first time. The measured curves do not show any significant distortion and

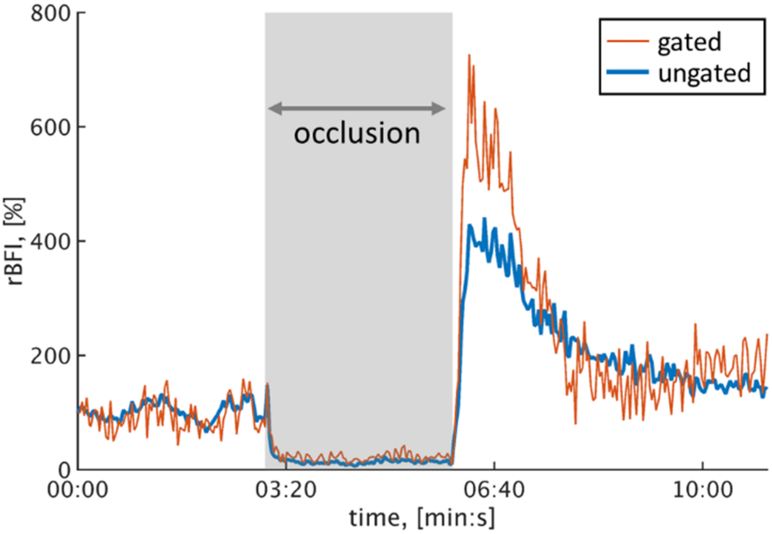

Figure 3.9: Relative BFi (rBFi) during the arm cuff experiment, fitted from the HW correlator output. Two channels are represented, one for the gated, quasi-null separation detector (thin orange line), and one for the ungated, long separation detector (thick blue line). (Adapted with permission from Ref. [87]).

good fit was achieved with our proposed model.

Quantitatively, the estimated BFi dynamics at the quasi-null source-detector separation is in good accordance, albeit slightly noisier, with the measurement at ρ=12 mm during most of the experiment. Furthermore, the quasi-null-separation rBFi shows notably a ~37 % higher hyperemic peak during re-perfusion, and a faster decay towards the baseline. This is expected since the gated, quasi-null-separation measurement probes selectively deeper into the more metabolically active and reactive muscle tissue; higher hyperemic peaks were also observed in multi-distance measurements at large source-detector separations

[73].

It's noteworthy that I have reported results for a very short, quasi-null source-detector separation that is not null but measured slightly less than 3 mm. However, in TRS studies it has been previously shown that no notable differences are to be observed between quasi-null and null distance [118, 74], as long as the quasi-null separation is within few millimeter range and diffusing homogeneous turbid media with the average optical properties of tissue (μ_{s}'=$\sim$10 cm^{-1} and μ_{a}=$\sim$0.1 cm^{-1}). Truly null source-detector separation is beyond the scope of this proof-of-principle experiment but was demonstrated in the past for time-resolved experiments [115].

3.4 Time domain speckle contrast spectroscopy

In this section I discuss the concept of applying time domain techniques to speckle contrast optical spectroscopy (SCOS). I briefly go through the theory of continuous wave (CW-)SCOS, its main limitations and strengths, and describe an *in vivo* experiment that uses pulsed light and time-of-flight sensitive detectors as a showcase of TD-SCOS capabilities.

SCOS [119] measures scatterers dynamics in turbid media by quantitatively assessing the speckle contrast on its surface. Conceptually, this lies at an intermediate step between laser speckle flowmetry [120] and DCS [5]; SCOS however relies on diffuse optics to extract information about the deep tissue blood flow. Pixelated large area detectors [119] or detector arrays [121] are commonly used in SCOS; they are generally slower (and cheaper) than the ones used in DCS.

While both techniques rely on long coherence continuous wave (CW) sources, SCOS is the weapon of choice for the preclinical setting. Having multiple detector channels allows non contact, deep tissue measurements of blood flow of the mouse or rat brain and therefore SCOS tomography (SCOT, [122]) up to few centimeters. Millions of channels, in case of a charge-coupled device (CCD) and complementary metal-oxide-semiconductor (CMOS) cameras, or thousands of channels in case a single photon avalanche diode (SPAD) arrays, would be prohibitively expensive if they were required run at the speed needed for DCS, considering also that each channel would need its own intensity correlator. Detectors used for SCOS, on the contrary, have much reduced requirements in terms of speed, they can be produced by standard silicon manufacturing processes (CMOS processing). This is possible due to a much simplified data analysis strategy used in SCOS with respect to DCS.

TD-SCOS is aimed at enhancing the depth sensitivity of every SCOS channel. By using fast gated SPAD (fgSPAD) detectors [114, 117], time-of-flight sensitivity to longer time-of-flight photons comes naturally into the SCOS data analysis framework and does not potentially require photon timing electronics. Since diffuse optics modeling of photon transport is valid for large time-of-flight photons at any source detector separation (see section 2.1.4), very short separation between the source and detector optics can be used, provided that fgSPAD are used to neglect the initial burst of short time-of-flight photons. Consequently, TD-SCOS displays increased photon collection efficiency and reduced partial volume effects.

In the following paragraphs I first describe a single SCOS pixel *in vivo* experiment that makes use of the speckle contrast information to retrieve the blood flow at very short, quasi-null separation. I then discuss the results by highlighting the advantages with respect to SCOS and the technical challenges.

3.4.1 Time-domain speckle contrast

Coherent light scattered from an ensemble of scatterers generates a interference pattern called speckle pattern. If some of the scatterers are moving, the intensity of the pattern varies depending on the motion of scatterers [123]. The area over which this pattern is detectable spans few cm^2. A quantity called the speckle contrast κ can be defined as the standard deviation σ over the mean μ of the time-varying intensity for a certain integration time T computed over an ensemble of different independent speckles in space, time, or both:

$$\kappa^2(T) = \frac{\sigma(T)}{\mu(T)} \tag{3.5}$$

When the intensity is measured with a device that is sensitive to each photon time-of-flight, like in TD-DCS for example, one can define a time-gated κ as the speckle contrast given by the contribution of only those photons that belong to a certain time-of-flight interval, or gate, i.e. (t_1, ∞). In a similar way to TD-DCS (see section 3.2) one can model the electric field autocorrelation, and therefore the intensity autocorrelation when Siegert relation is assumed to be valid, for a time-of-flight gate as in eq. 3.2. The equation for speckle contrast that was first introduced in [124], eq. 8 therein, can be thus modified in the time-of-flight gated case as

$$\kappa^2(T) = \frac{2\beta}{T} \int_0^T \left(1 - \frac{\tau}{T}\right) \left[\int_{t_1}^{\infty} R(t)\, g_1^{single}(\tau, t; \mathrm{BFi})\, dt\right]^2 d\tau \tag{3.6}$$

Equation 3.6 therefore relates the BFi with the speckle contrast and can be evaluated numerically to assess the former from the latter. For ergodic systems of scatterers like, in most cases of interest, tissue perfused by red blood cells, ensemble average can be substituted by time average when computing κ.

3.4.2 Methods

Time-of-flight sensitivity has been implemented by adapting the null source-detector separation TD-DCS setup described in [87] and section 3.3. The 12 mm separation channel is used as a monitor channel to be analyzed using standard SCOS and the TD-SCOS channel performances are compared against it.

The same laser source of the previous experiments (see sections 3.2 and 3.3) was used.

Experimental protocol

An adult healthy human subject (female, 26 years old) underwent arm cuff occlusion protocol consisting in 3 minutes baseline, 3 minutes occlusion, and 4 minutes recovery. While the subject sat comfortably on a chair with the elbow bent and the forearm resting on a table cloth, arterial circulation was stopped by inflating the tourniquet of a manually operated sphygmomanometer, placed under the shoulder joint, well above her systolic pressure. A $3 \times 3\,\mathrm{cm}^2$ soft black foam pad probe, embedding the source and the two detector single mode fibers, was placed above the brachioradialis muscle of the same arm. Superficial tissue thickness in the region of the probe was estimated to be 13 mm by using a plicometer. The protocol was approved by the Ethical Committee of Politecnico di Milano and it was conducted in agreement with the Declaration of Helsinki. The subject gave written consent before her participation.

Data analysis

A i5 (Intel, USA) PC running windows 7 manages both the TCSPC software (operated in TTTR mode with external synchronization trigger from the laser), which saves the photon arrival times on a `.ptu` file, and the Flex-05 8-channel USB correlator, which saves the intensity autocorrelation curves on a set of `.dat` files (one per acquisition). At the exact starting moment of the experiment, both instrument interfaces were also synchronously started; the delay between the two is therefore on the order of the correlator sampling period, $\sim$2 s.

TD-SCOS channel For the TD-SCOS channel, the speckle contrast κ was computed by temporally binning the number of photons detected over a set of integration times T_j, by using a decorrelation time Δt=10 ms, over a 500·Δt window (5 minutes) that was shifted by a delay d=1 s to obtain each data point. The set of M=20 exposure times that I used was: T_j=50, 100, 200, 400, 600, 800, 1000, 1200, 1400, 1600, 1800, 2000, 3000, 4000, 5000, 6000, 7000, 8000, 9000 and 10 000 µs. The integral on the right side of equation 3.6 was numerically solved for each T and fitted to the speckle contrasts obtained. Blood flow index was then extracted as the best fit parameters, using average optical properties (μ_s'=10 cm^{-1}, μ_a=0.1 cm^{-1} and refractive index n=1.4). This was repeated at every second. This algorithm is an adaptation of the spatial window SCOS algorithm [122]; to the best of my knowledge it is the first time it is applied and it is thoroughly described in detail in appendix 3.A.

SCOS channel Measured (ungated) autocorrelations of the electric field $\hat{g}_1^{(i)}(\tau)$ for $i = 1...n$, where n is the number of the curves obtained every 2 s during the experiment, were obtained from the intensity autocorrelations ($\hat{g}_2^{(i)}(\tau)$) by using the Siegert relation; an average β was measured after the acquisition and used for all the curves. The measured curves were fitted with the ungated DCS model (see section 2.2.2), obtaining $g_1^{(i)}$ model at best fit. The contrast κ^2 was then obtained by substituting the best-fit $g_1^{(i)}(\tau)$ in right side 3.6, as it corresponds to the ungated case.

A Nelder-Mead simplex method was used to fit the κ^2 data in both the detection channels using the `fminsearch` function in Matlab [125].

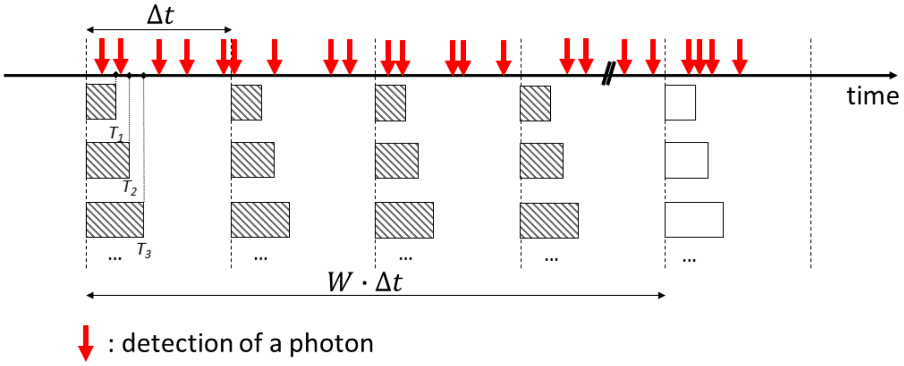

Figure 3.10: Working principle of the sliding temporal window SCOS analysis: photons that fall in exposure times $T_1 ... T_M$ are counted. After a decorrelation time Δt, this is repeated, within the bounds of a temporal window lasting $W \cdot \Delta t$. Iterating over j=1...M and i=1...W, the variance σ_j^2 and mean intensity μ_j are computed over W measurements of the number of counts over an array of W $T_j^{(i)}$. In order to achieve a sub-window sampling time, the window is then shifted by a (arbitrary) time delay d, and the process is repeated.

3.4.3 Results

The entire protocol lasted 660 s during which n=318 curves (2 s integration time each) were acquired by the Flex-05 hardware 8-channel USB correlator. At the time of the experiment, count rate in both channel were, on average, 379 kcps for the quasi-null separation TD-SCOS channel and 228 kcps for the 12 mm separation SCOS channel (average β=0.26).

In figure 3.11 the κ^2 for the quasi-null separation TD-SCOS channel, computed over 3 minutes of baseline, is reported. The sliding window algorithm uses a 1 s delay; three window sizes of 1, 2 and 5 s (100, 200 and 500 decorrelation times) are reported. The κ^2 computed at each slide of the window fitting within the baseline was then averaged (squares). The standard deviation of the speckle contrast was also computed and is reported as errorbars.

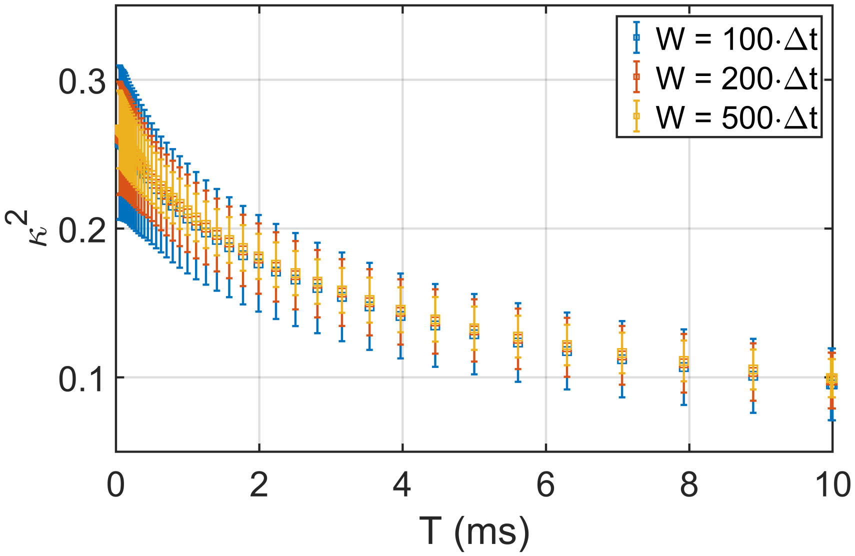

Figure 3.11: Speckle contrast from the first 3 minutes of baseline for different window sizes. The sliding temporal window algorithm was applied with delay of 1 s and then averaged (squares); errorbars report the standard deviation.

Figure 3.12 shows the κ^2 computed for the quasi-null separation TD-SCOS channel using a window size of 5 s (500 decorrelation times) and its fit as described in section 3.4.2 at different stages during the cuff occlusion experiment. It is evident how the absolute values of κ^2 increase during occlusion (shaded plots, t=180 s to t=359 s), as expected for lower blood flow and therefore slower decays of the electric field autocorrelation function.

The plots of the measured electric field ungated autocorrelation curves ($\hat{g}_1^{(i)}(\tau)$, 2 s integration time each, i=1..318) from the hardware correlator for the SCOS channel are reported in figure 3.13 at various stages of the cuff occlusion experiment (occlusion stages are marked as blue shaded plots). The characteristic time at which g_1 reaches a value of 0.5 are reported (red dot). Vertical lines show the minimum and maximum exposure times that were used to compute SCOS κ. Standard DCS best fit $g_1^{(i)}$ curves (red line) are superimposed to each plot.

The BFi curves obtained by the SCOS and TD-SCOS analysis of the corresponding channels are reported in fig. 3.14.

3.4.4 Discussion

Here I used a single detector channel as a proof-of-concept for TD-SCOS. The ability of running at very short, quasi-null source-detector separation was previously unmet. As described in section 2.1.4, this determines a higher photon collection efficiency and a decrease of tissue partial volume effects that in turn correspond to a higher contrast and signal-to-noise ratio when measuring localized hemodynamic changes.

Although the rBFi curves of SCOS and TD-SCOS in fig. 3.14 have similar trends during baseline, occlusion and recovery, higher hyperemic peak and a faster recovery of baseline values are evident for the quasi-null separation TD-SCOS channel when compared to the monitor SCOS channel. This indicates that the technique, by selecting longer time-of-flight making use of the time-domain method, is able to penetrate the tissue in the arm and reach the more metabolically active and reactive muscle tissue underneath, in a fashion similar to large source-detector measurements [73]. As discussed above, however, by measuring the rather homogeneous changes undergoing in the arm muscle, the benefit of a theoretically achievable small lateral partial volume effect is not shown because the changes in blood flow are not laterally localized.

It is also noteworthy that the computationally simpler data analysis method of TD-SCOS (see appendix 3.A) compared to TD-DCS, as one can compute κ^2 instead of the full autocorrelation, can be disruptive when scaling up the number of detectors. The timing resolution required to store the SCOS and TD-SCOS data to be processed is in the order of the smallest exposure time (50 µs), therefore much smaller (about 1000 times) than the time resolution of correlators used in DCS and TD-DCS. Gated silicon detectors, like the fgSPAD exist [126] and essentially already implement gating and count integration, making the expensive timing devices used in TD-DCS redundant. However, the technological advantages of multi-detector SCOS (increased signal-to-noise ratio, possibility of tomographic reconstruction of flow, low cost per channel) are not practically demonstrated yet for TD-SCOS.

As a outlook, albeit the laser source used for this experiment is still an expensive and unique piece of equipment that accounts for most of the cost of this technology, multi-detector TD-SCOS is a valid recipe to make the cost per detection channel to drop, paving the way to the use in clinical or even point-of-care devices.

3.A Sliding temporal window algorithm

In this appendix I report the algorithm for computing κ^2 to which I have commonly referred to through chapter 3 as the *sliding temporal window* algorithm, which to the best of my knowledge is not reported elsewhere.

Input The algorithm needs the memory address of a file where the experimental data are stored as a sequence of photon arrival times t_a, in increasing order, and the associated time-of-flight (t_f). Time-of-flight is computed subtracting the pulse time of the peak of the IRF from the pulse time of each entry. These two numbers constitute a file entry. This way of storing the data is commonly referred to as "photon mode" (PM).

Parameters To implement the time domain character of this algorithm compared to CW-SCOS, only the file entries with a pulse time greater than a given threshold t_{TH} are considered. The speckle decorrelation time Δt[2] is the minimum time that has to pass between two exposures for them to be uncorrelated. Exposure times are defined by the user as a array of times T_i with $i = 1..nT$, in ascending order. A window parameter W here is chosen, which corresponds to how many exposures at the time T_i are considered when computing the variance and mean value of the intensity in order to estimate κ. For simplicity, W is a multiple of Δt. Finally, a time delay d, which represents the sliding temporal window accuracy, is given.

High-level functions In outlining the algorithm I assume that some high-level functions are already given in the environment in which the algorithm is implemented. Apart from element-wise floating point

---

[2] Some references use the notation τ_c for the speckle decorrelation time.

division (multiplication) / $(*)$, element-wise scalar addition (subtraction) $+$ $(-)$, integer post-increment by an unit $++$, they are:

1. `fread` reads a arrival time entry in a file at a place specified by a cursor, then moves the cursor to the next entry;
2. `var` computes the variance of a matrix of positive integer values acting along *rows*;
3. `mean` computes the average of a matrix of positive integer values acting along *rows*;
4. `fit` fits the κ^2 with respect to T according to the expression in 3.6, returns BFi (t_{TH}, β, the functions $g_1^{single}(\tau, t; \text{BFi})$ and $R(t)$ are given).

Output The algorithm returns an array of best fit BFi values, one per every slides of the window that is considered.

```
Input  : file $p$, time $t_{TH}$, time $\Delta t$, array of times $T$ (size
         1x $nT$), integer $W$, time $d$. $N = \lfloor (t_{end} - W\,\Delta t)/d \rfloor$ is
         the number windows slides to be considered.
Output: BFi array of size 1 x $N$
/* initialization                                               */
$file$ links $p$, cursor to first entry;
$T' = T$, a copy of the array;
$t_{end}$ is the $t_a$ of the last entry in $p$;
allocate BFi array of size 1x $N$;
allocate $\kappa^2$ array of size 1x $nT$;
/* loops                                                        */
for $i = 0$ to $N$ do
    allocate $M$ matrix of zeros of size $W$ x $nT$;
    for $j = 0$ to $W$ do
        $counter = 0$;
        for $k = 0$ to $nT$ do
            ($t_a$,$t_f$) = fread($file$);
            while $(t_a - (d * i)) < T_k$ do
                if $t_f > t_{TH}$ then
                    counter++;
                end
            end
            $M(j, k) = counter$;
            $T_k = T_k + \Delta t$;
        end
        set $file$ cursor to first $t_a - (d * i) \geq (\Delta t * k)$ entry;
    end
    $\kappa^2$ = var($M$)/mean($M$);
    BFi$_i$ = fit($T, \kappa^2$);
    set $file$ cursor to first $t_a - (d * i) \geq 0$ entry;
    $T = T'$;
end
```

Algorithm 1: Sliding window TD-SCOS algorithm.

The CW-SCOS case is obtained by using t_{TH} equal to the minimum recorded photon time-of-flight. Negative time-of-flights are possible for non ideal (i.e. non infinitesimally small) source pulses, detectors, and timing devices.

The algorithm here described is strictly valid only for ideal system not affected by noise. Shot noise and dark noise of the detector introduce a bias in the computed κ that can be accounted for as described in [119], eq. 4 therein.

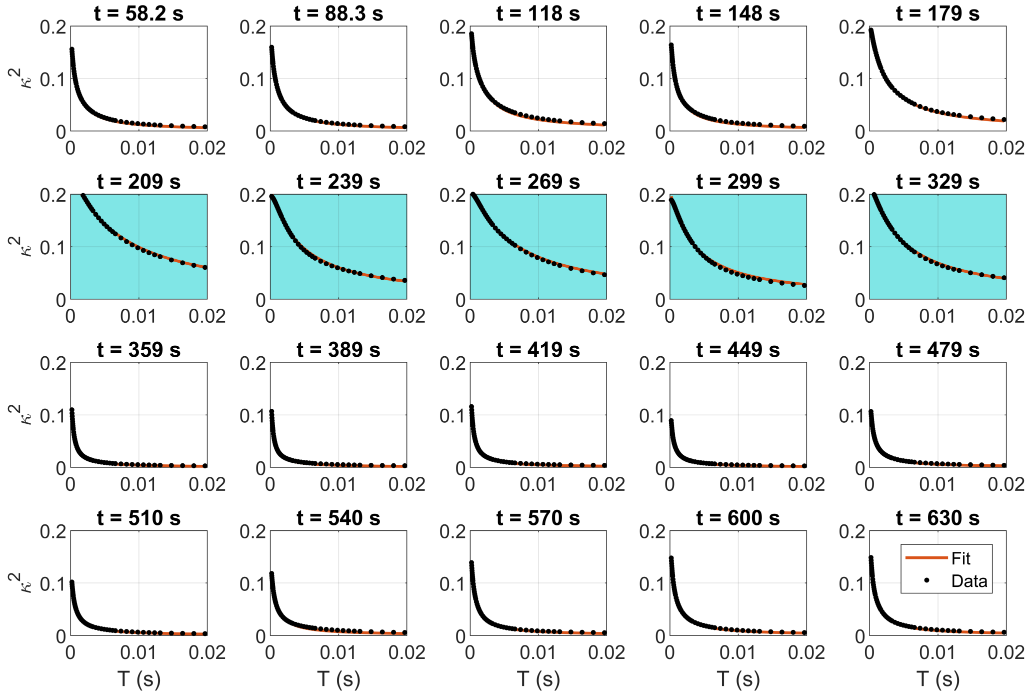

Figure 3.12: Computed κ^2 (black dots, *Data*) and TD-SCOS fit (red line, *Fit*) at various stages of the cuff occlusion experiment. Blue shaded area mark the plots corresponding to the occlusion.

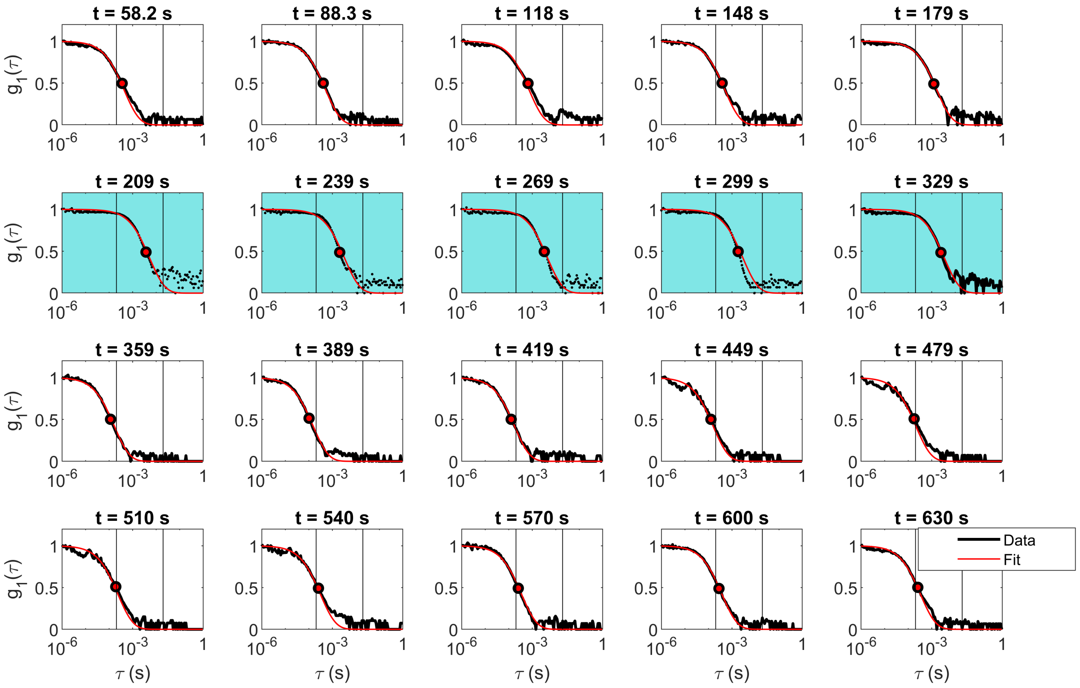

Figure 3.13: Electric field measured autococorrelation (*Data*) for the 12 mm SCOS channel and superimposed best fit model (*Fit*) for some stages of the cuff occlusion experiment. Stages corresponding to the occlusion are highlighted by blue shading of the plot area.

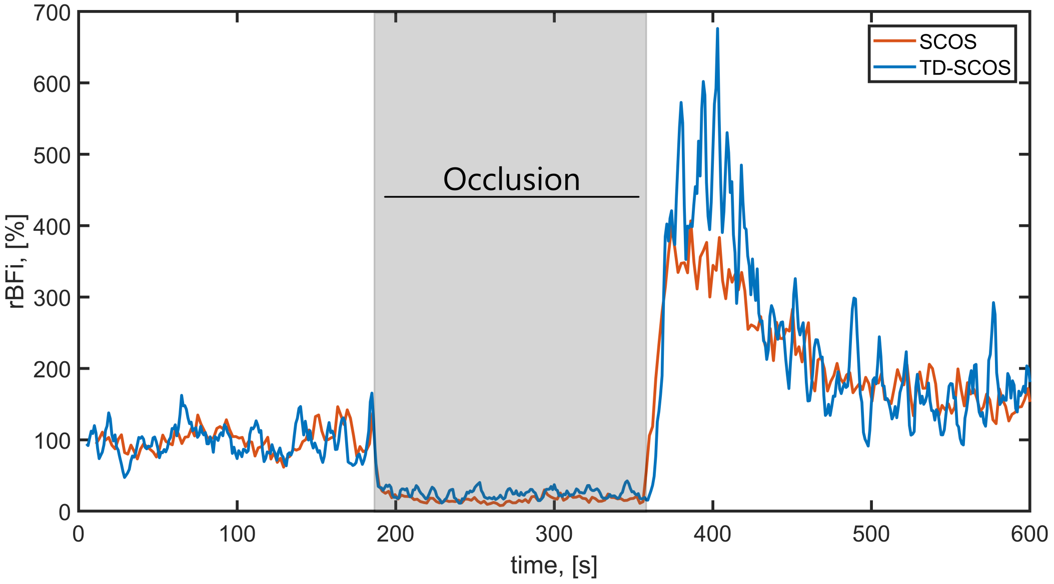

Figure 3.14: BFi relative to the baseline (first 100 s) for the SCOS (orange) and TD-SCOS (blue line) channels. Occlusion of the afferent arteries in the arm was carried out between 180 and 360 s (grey shaded area).

Chapter 4

Functional diffuse correlation spectroscopy on infants

All the work behind the following chapter has been carried out with the collaboration of Dr. Núria Sebastian-Galles, Marc Colomer Canyelles, Dr. Carlos Guerrero-Mosquera, Dr. Chiara Santolin from the Center of Brain and Cognition of Universitat Pompeu Fabra (Barcelona, Spain) and Dr. Aykut Eken of ICFO (Castelldefels, Spain). I'd also like to acknowledge Dr. Judith Gervain, Laboratoire Psychologie de la Perception, Université Paris Descartes (Paris, France) for her helpful and constructive advice. The present work has in part been presented at the 5th conference of the fNIRS society [127].

4.1 Introduction

Cortical function in the brain constantly need supply of oxygen and nutrients and removal of byproducts by circulating blood at the microvascular level. In healthy adults, functional neuronal activations are indeed manifest in healthy adults as a increase in the local cerebral metabolic rate of oxygen extraction, which in turn results in local variations of both the oxygen extraction fraction (that can be non-invasively measured by fMRI [128] or fNIRS [5]) and cerebral blood flow (non-invasively measured at the microvascular level by MRI or DCS [7]). A simpler to detect marker of functional activation is, through the mechanism of neurovascular coupling, the reactive hyperemia (RH, and increase of blood flow and therefore volume) that is manifest as an increase of oxygenated and a decrease of deoxygenated hemoglobin; the latter is supposed to be the basis for the blood oxygen level dependent (BOLD) MRI signal observed in fMRI, while both contribute to the intrinsic signals observed in fNIRS. To this extent, DCS is inherently more sensitive (higher contrast to noise ratio, [21]) to measure cortical blood flow measured from the scalp than CW fNIRS . Functional DCS (fDCS) has been therefore applied in human to detect sensory-motor and visual cortical activation [7, 129].

The neurovascular coupling in the developing brain is still poorly understood [130]. Functional MRI is hard to use on un-sedated infants. On the other hand, thinner scalp and skull and the relative lack of hair in the head of human infants is supposed to facilitate diffuse optical investigation, which however is limited to superficial layers of the cortex. The first fNIRS studies on infants have been historically carried out by detecting relative [HbO_2] and [Hb] changes as markers of reactive hyperemia (RH) when the visual cortex is stimulated by showing a flickering checkerboard on a screen to the subject [131]. This study was carried out on awake infants, 0 to 3.5 months old, looking to a flickering checkerboard lasting (10 s) followed by the dimming (10 s) of a screen in a block designed pattern repeating several times. This age bracket is widely considered in the literature [131, 33, 34, 132, 133]. It is believed that subjects at this age are relatively calm and collaborative. In some studies [131, 33, 132, 34], successful recording of cortical RH was possible while the subject could calmly sit on the parent's lap while being probed. Block patterns as simple as repetitions of rest/stimulus conditions are indeed common when detecting functionally-evoked relative changes.

In the following paragraphs I show the methodology and discuss the results and the limitation of fDCS applied to the detection of RH in awake human infants of about 4 months of age.

4.2 Methods

Young infants of 3.5 to 4.5 months of age were considered for the study. Subject recruitment was carried out by Center for Brain and Cognition, Universitat Pompeu Fabra (Barcelona, Spain). Seventeen subjects were accepted and scanned for visual activation. Five of them were also recruited some days before or later and scanned with a sham protocol.

Device description

I built the DCS optical apparatus for the purpose at ICFO. It comprises two 4-channel single photon detectors (AQ4C, Excelitas, Canada), an electronic 8-channels USB correlator (Flex-05, Correlator.com, USA) and two continuous wave (CW) 785 nm lasers sources (Crystalaser, USA). At each acquisition step, the correlations of each channel were saved on a file in a Windows PC with a average sample rate of 1.90 Hz (integration time of 526 ms) using a Visual Basic graphical user interface. The whole device is connected to the wall plug through a isolation transformer (REO-MED1000-230V, REO, Craven Arms, UK) for safety reasons. I carried out a test of the device and appliances for electrical safety. The device is provided of an external *trigger box* (TB), implemented with an Arduino Due, that records and measures the time of the readings from an accelerometer located on the optical probe, from the correlator (that signals when correlations have been acquired), and from another Windows computer that manages the presentation of the stimuli. By acting as *slave*, the TB marks down on a file, with millisecond accuracy, all these timings together with the reading of the accelerometer. Here's an example of some entries that are saved on a file in a SD memory card on the TB and loaded after the experiment to temporally align the BFi data and the stimulus condition.

```
...
DCSfile 73 at time: 11408, status 01, ACC: 9.60
DCSfile 74 at time: 12158, status 01, ACC: 9.60
DCSfile 75 at time: 12798, status 11, ACC: 9.63
DCSfile 76 at time: 13439, status 11, ACC: 9.61
DCSfile 77 at time: 14189, status 11, ACC: 9.60
Stimulus no. 3 at time: 14406, status 11
DCSfile 78 at time: 14939, status 11, ACC: 9.53
...
```

Listing 4.1: In this sample, sequential numbering from the start of the experiment, milliseconds from turning on the TB, `status` reads pin 1 and 2 of the parallel port on the experimental conrtol PC and can be `01` or `11` depending on the type of visual stimulus (see below), and `ACC` is the integrated accelerometer raw reading between two measurements.

The sequences of visual stimuli and resting conditions were managed by a Windows PC running the Psychtoolbox extension in Matlab [134, 135, 136] and presented on a 19" diagonal ASUS VG248 screen placed 60 cm from the subject and adjusted at the same height. Parallel port pin 1 and 2 connection with the TB allowed precise timing of the sequence. The electroencephalography (EEG) device is a Geodesic (EGI, Eugene, USA) and an HydroCel mesh of 128 sensors from the same company was used, its size fitting infants heads between 3 and 5 months of age.

Probe

I used three bundles of two single mode fibers each (780HP, Neufern, USA), placed at the vertices of a idea equilateral triangle, that collected the light emitted by a Crystal Laser coupled to a multimode fiber (WF200, Ceramoptecs, USA), placed in the center of the triangle, the latter coinciding with the subject's inion after proper placement. Output laser power at this fiber tip was limited to 30 mW, according to ANSI Z136.1 maximum permissible exposure recommendations for skin. Source detector separation is 15.0 ± 0.5 mm. Detector bundles are labeled as A, B and C, starting with the first (A) laying on the medial line above the inion and proceeding clockwise (see figure 4.1 below).

I used another single mode fiber bundle (780HP, labeled T) to detect light, which was delivered to the scalp from the other laser using another WF200 fiber, in a control location above the subject's right prefrontal cortex, about 13.5 cm away along the head circumference. All fibers had a 90° bent tip that I embedded in two separate patches made of semi-rigid plastic that were covered by latex. I have found latex coating convenient to increase skin-probe attrition and therefore to reduce motion artifacts [137]. The patches were fixed to a 50 cm (length) x 2 cm (width) x 1 mm (thickness) head band also made of plastic mesh that I then coated with latex. On the overall, the optode patches and the portion of the fibers directly on the head weighted just about 45 g. For most of their 10 m length, the weight of the fibers was supported by the ground or by the chair where the subject and the carer sat. In a recent review, Cristia *et al.* [138] claim how excessive probe weight can result in decreased inclusion rate for the subjects due to movement induced artifacts and discomfort.

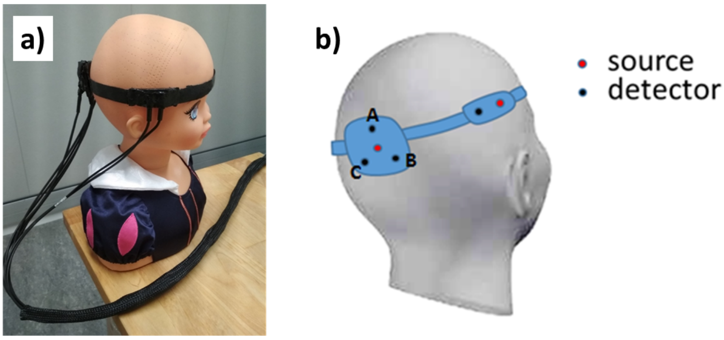

Figure 4.1: a) Source and detector fibers are inserted into two latex covered patches joined by a latex-covered bandage encircling the head. The band attachment can be adjusted to fit to each subject's circumference (head circumference of the doll is 40 cm). b) Position of optodes in the occipital area.

Measurement location

I identified the primary visual cortex by locating the inion as an anatomical landmark. The experimenter then placed the source fiber of the first patch right above it, with two detector fibers below and one above it along the cranio-caudal direction. Due to the age of the babies, there was typically too few hair to obstruct the light or to impede the identification of the inion. When encircling the head circumference with the latex band, I made sure that the second patch lied above the temporal region of the head. The latex band was always longer than the head circumference and had a self-adhesive behavior; the leftover flappers were made to adhere in order to secure the whole probe. A high density electro encephalogram (EEG) elastic cap (Geodesic, USA) was bathed in a warm water and salt solution and then placed on the head, above the optical probe, and indeed further secured the band and patches to the head.

Epoch design

I used a block design alternating blocks of strong visual stimulation with rest periods in some cases. The design was adapted from [139]. Subjects were awake, visually engaged with the screen, and sitting on the parent's lap. In order to restrain the parent from stimulus-dependent interactions, he or she had to wear darkened glasses that impeded to perceive what was presented on the screen. I acquired a video of the subject through a webcam placed few centimeters above the screen to assess the subject's visual engagement and to detect possible movements generating artifacts in the optical data. The visual stimulus was a flickering radial checkerboard flashing at 3.3 Hz with a human face displayed and looming at the centre of the screen (STM). Spatial frequencies of the checkerboard features varied between $0.07\,\mathrm{cm}^{-1}$ and $0.7\,\mathrm{cm}^{-1}$ which translates in angular sizes between 0.75 and 7.5 degrees by considering distance of the subjects and size of the screen. The stimulus block lasted 10 s and was preceded by 1 to 3 s of the same looming faces on a grey background (hereafter termed "attention getter", AG), and followed by 15 to 20 s of fireworks (FW) displayed on dim background. AG and FW had a variable duration; while AG played for at least one second up until a button was pressed by the experimenter, as soon as the subject's attention was caught in a stable manner by the display (and not for more than 3 s, in any case), FW played for a random amount of time, between 18 to 22 s. In sham experiments, the STM block was substituted by 10 s of looming faces on a grey background, in a way that is similar to AG.

An *epoch* is therefore the collection of three consecutive blocks: AG, STM and FW; its duration varied between 29 to 35 s due to recovery randomization (see figure 4.2). The looming faces were randomly selected during each epoch from a subset of “NimStim Set of Facial Expressions” ([140]). The face increase and decrease its size (looms) from 0.52 cm to 2.7 cm and changes to a new face every two cycles (2 s each) to hold the infant’s attention. The study lasted for a maximum of 15 blocks or up to when the subject became bored or fussy,

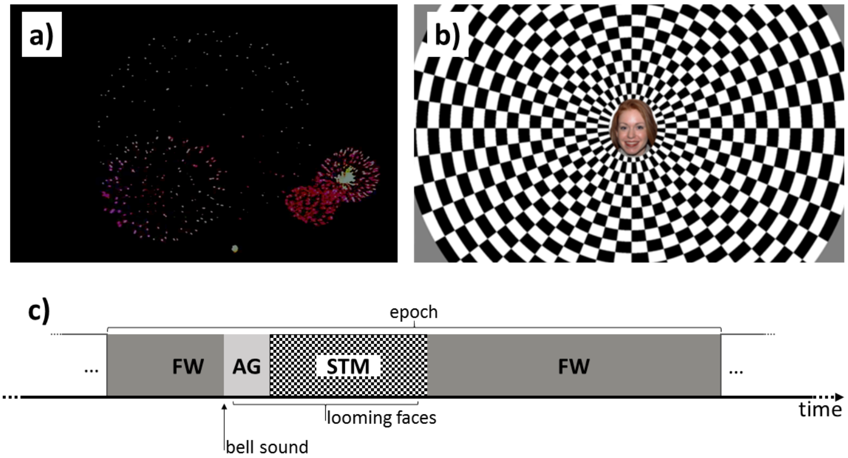

Figure 4.2: a) A frame selected from a fireworks in the night sky movie (FW). Luminosity has been increased by 40% for display purposes. b) A frame selected from the radial checkerboard animation (STM). The face in the middle has been extracted from the “NimStim set of facial expressions” [140]. The face increases 20% its size and shrinks back to this dimension every second (it looms), during both STM and AG. In shams, the checkerboard is replaced by a uniform gray background. c) Sequence of the screen statuses constituting a epoch.

based on the experimenter's judgment. During the whole experiment, soft nursery music, "Camptown races", was played in the background from standard 5 W desktop loudspeakers. Change from FW to AG was accompanied by a bell sound.

4.3 Data Analysis

Event related potentials EEG data analysis relies on quite standard evaluation of event related potentials at some electrode locations. Optical data analysis is instead a process that is worth to describe in detail because, although its potential, DCS has been seldom used in functional protocols to date [5, 141] and, to the best of our knowledge, never in the functional imaging of the awake infant.

A-priori optical quality assessment The intensity in terms of kilo counts per second (kcps) was used as a criterion available for each recorded intensity correlation function (6 for the occipital and 2 from the temporal patches). Values below 10 kcps implied rejection of the associated curves, as the likely cause was a bad optical attachment of the probe. Intensity autocorrelation functions were then first screened for systematic errors. For each spatial channel (A, B, C or T), if both intensity autocorrelation curves passed the screening, the two electric field autocorrelations were computed using the Siegert relation, by using β=0.48[1], and averaged; if just one in two passed, no averaging was carried out; if none of the two channels correlations passed the a-priori assessment, BFi was set to not-a-number (`NaN`) and analysis skipped to the next data point to be processed.

---

[1] β=0.48 is the expected value for the laser/detector combination used.

BFi assessment The homogeneous tissue model [142] for DCS with optical properties μ_s'=10 cm^{-1}, μ_a=0.1 cm^{-1}, n=1.4, was fitted to the acquired autocorrelation curves in Matlab (Mathworks, USA) using the `fminsearch` function. Optimization was carried out on the sum of the square of the residuals at delay times between 400 ns and the delay time at which the electric field autocorrelation g_1=0.7. Four raw BFi time series were therefore obtained.

Filtering and segmentation I used a flat-weighted moving average filter (15 points) to reduce noise in the BFi data series. Using the time tags stored in the TB file I was able to segment the BFi time series and associate each data point to its epoch and condition. Upon visual inspection of the videos, the epochs in which the baby was not paying attention to the stimulus or jerked his head up to a way that motion artifacts were likely to have severely affected the BFi signals were discarded. This happened mostly towards the end of the experiment, and only in some subjects. Segmented BFi within an epoch was then normalized by its baseline, which is defined as the whole duration of the attention getter relative to the epoch, for each epoch and subject separately:

$$\Delta rBFi^{(i)} = \left(\frac{BFi^{(i)}(t)}{\langle BFI^{(i)} \rangle_{AG^{(i)}}} - 1 \right) \cdot 100 \tag{4.1}$$

The obtained quantity $\Delta rBFi^{(i)}$ is the the percent variation of the relative BFi (rBFi) with respect to the baseline for the i-th epoch. Based on these values, I performed some *a posteriori* data rejection that I describe in the next two paragraphs.

Motion artifacts In order to remove spurious effects due to hemodynamic changes overlapping the expected RH signal, motion artifacts due to movements of the head that change the instantaneous coupling efficiency of the source or detector channel to the scalp or that simply get transmitted to the fiber, shaking them, are usually visible as abrupt increases limited to few points of $\Delta rBFi^{(i)}$. Some of these data points could pass through the *a priori* quality assessment of the autocorrelation curves I performed, as they don't distort the autocorrelation curves so much that they trigger automatic rejection. Channels (A, B, C or T) showing abrupt changes in $\Delta rBFi$ were rejected.

Baseline Low frequency (lower than the stimulus presentation time, therefore than the expected hemodynamic response) hemodynamic variations coming either from the brain or from the superficial tissue (systemic) can be mixed into the data and generate spurious responses. For this reason, based on the typical shape of the $\Delta rBFi$ time series, I decided considering only the first epoch of each experiment. Even in this case, to counterbalance the loss of data at the two previous steps, I averaged together all the channels probing the occipital area (A, B and C) on a per-data-point basis.

4.4 Results

Among the 22 total experiments, I achieved an average of 8.4 epochs per subject (4 min and 20 s, 56% success) in which the subject was, upon visual inspection of their behavior and an estimate of their gaze direction based on the recorded video of the experiment, paying attention to the stimulus and being calm and focused on the screen during the recovery. Only one subjects completed the 15-epochs protocol (7 min and 45 s). A minimum of 4 epochs per subject was recorded in 3 cases. Among all the subjects scanned, however, only 12 subjects in 13 experiments had an acceptable behavior during the first epoch shown. Only this subset is reported here. Of these 12 subjects, 2 only contributed as sham, for a total of 3 shams.

In fig. 4.3 I have reported two curves from the same experiment and channel, acquired at different times. Despite being acquired at a comparable and rather high count rate, and therefore having a rather good signal-to-noise ratio, each of the two curves was either accepted (green circles) or rejected (red circles) by the automatic rejection algorithm based on autocorrelation curve shape described above in paragraph 4.3. In particular, it can be noticed that the red dotted curve has a high value of the intercept with the y-axis at τ=0 s ($\beta\sim 0.6$, maximum physical value being β=0.5) and that there is a characteristic bump in the tail for large delay times ($10^{-3}\,\mathrm{s} < \tau < 10^{-1}\,\mathrm{s}$) where the value of g_2 is noticeably greater than 1.

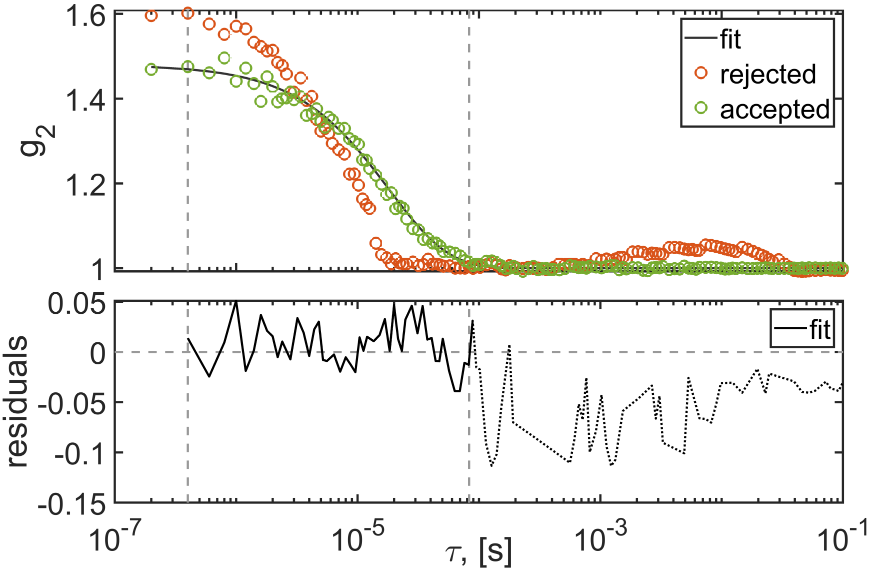

Figure 4.3: On top, two measured autocorrelation curves during the same experiment, one rejected (red circles, 138 kcps) and one accepted (green circles, 198 kcps); the accepted one was also fitted with the homogeneous DCS model and the residuals ($g_1^{measured} - g_1^{model}$) of the fit are shown (bottom).

I have reported in detail three experimental outcomes on three different subjects in fig. 4.4. In (a) a sham experiment (checkerboard not present), a tiny increase with respect to the baseline was seen, with little difference between the occipital and temporal patch signals; it reached its peak in the middle of the stimulus block in the occipital channels, while, in the temporal channel, the peak was reached after stimulus ended. It is worth noting that even though during the sham protocol the checkerboard was not displayed, looming faces were shown starting at the same time of the AG condition, which in this case happens 2 s before stimulus began. In the first of two other experiments that I highlighted, carried out with the standard stimulation protocol (i.e. the checkerboard is shown during stimulus), a much more consistent increase in the BFi was seen. This increase was not seen equally by all the optode locations in the occipital patch, as the broad range of $\Delta rBFi$ suggests; it is anyway in the order of 30%, it started increasing right after the onset of the STM condition, and it reached its peak right after the end of stimulus, 10 s later. The decay was rather slow and happened at approximately the same rate as the increase. In the last highlight, (c), having shown a flashing checkerboard to the subject during stimulus resulted in a BFi time series that resembles, in the occipital channels, case (b) (temporal channel not available). The rate at which the BFi increased was also similar. A plateau, or perhaps the signal reaching its peak later, determined a even slower recovery of the initial (baseline) values.

In fig. 4.5 the time series of the first epoch of the 13 experiments (grouped by experimental condition, i.e. sham or non-sham, red and blue line respectively) are reported against the temporal channel time series of $\Delta rBFi$. Time is reported on the x-axis, normalized to the start of the STM condition, that is marked by a thick black line. With respect to the two highlighted non-sham cases, the blue line showed

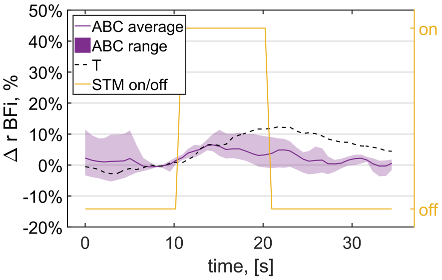

(a) Sham experiment. Moderate increase (~10%) in $\Delta rBFi$ but also in the temporal (T) channel during and after STM is visible.

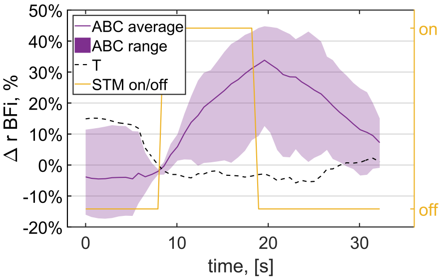

(b) Non-sham. An increase in $\Delta rBFi$ in the occipital region is observed, while the temporal (T) channel readings are constant, suggesting a localized, non-systemic origin of the signal from the visual cortex.

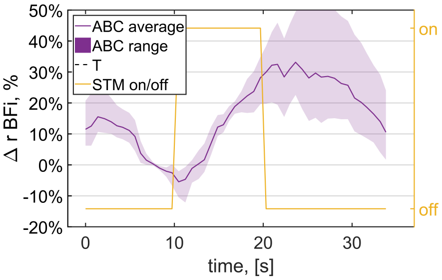

(c) Non-sham. Very similar amplitude and $\Delta rBFi$ increase rate, but longer duration, in the occipital channels during STM with respect to (b). No temporal (T) channel time series was available for comparison.

Figure 4.4: Three $\Delta rBFi$ time series for the first epoch recorded in three experiments. The yellow line marks STM status (on/off); the purple line and the purple shaded area represent the average of the occipital channels and the range of their values, respectively; the black dashed line (reported when available) corresponds to the temporal channel T.

a lower peak value and a steady increase up to 15 s after STM onset. On the other hand, the three shams showed an average response that is bi-phasic, with a dip within stimulus and a peak at 20 s, marking 10% increase in rBFi. While this behavior is unexpected, it is worth noting that this is the average of only three experiments having rather different responses one respect to the other. Both signals in the end failed to reach baseline values towards the end of the epoch. The temporal channel time series was indeed rather flat and lays between 0 and 5%, a range comparable with its uncertainty.

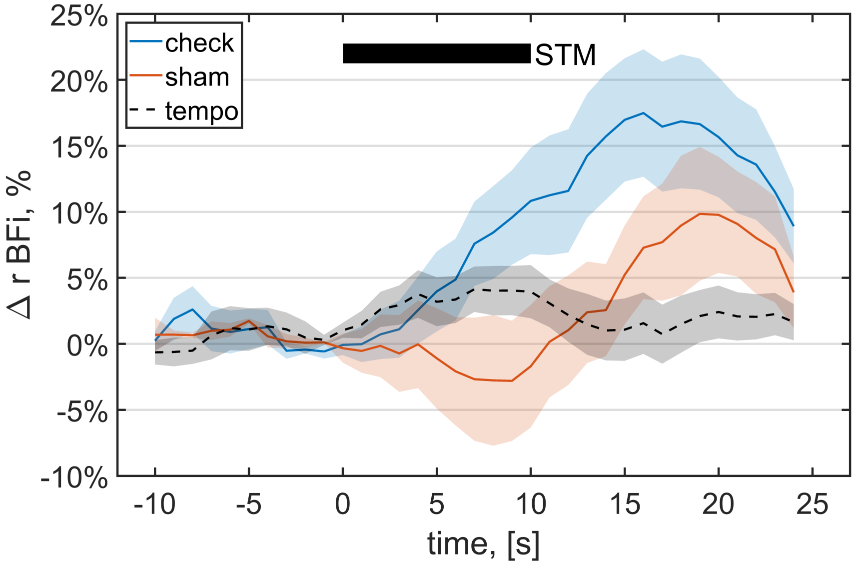

Figure 4.5: Average of all subjects' $\Delta rBFi$ time series. *Sham* and non-sham (*check*) conditions for the occipital channels A, B and C are compared with the inter-subject average of the temporal patch location (*tempo*). The latter is averaged independently on the experimental condition. A black bar represents the start and duration of STM. Shaded area is the inter-subject standard error (SE).

4.5 Discussion

According to [132], [33] and [34] the occipital area of the head, and in particular the region closer to the inion, is expected to originate a detectable HR in babies within an age bracket comparable to the one of the present study. Notably, this area does not exactly coincide with the primary visual cortex in adults.

Regarding the experimental paradigm, I have chosen fireworks display on a dim background for the resting block because it constitutes a visual pattern with low probability of triggering a strong hemodynamic response in the visual cortex; on the other hand, the resting block was designed to keep the attention of the subject between stimulation blocks to an acceptable level. During stimulation blocks, the features of the radial checkerboard pattern span many spatial frequencies and are expected to strongly engage the subject, despite the fact that infants' visual acuity is reported to still be developing at that ages. Looming faces in the center of radial pattern cover the region with the highest spatial frequency patterns, which would likely be missed by the baby, and by looming, they promote the infant's fixation to the center of the screen. During stimulus, a strong hemodynamic response is therefore expected, putting it at the highest rank in therms of stimulation intensity. On the contrary, attention getter is used to promote visual fixation to the screen at the moment of presenting the stimulus. Its dim background is supposed to do not stimulate hemodynamic response as much as the checkerboard. During sham, finally, the absence of the flickering checkerboard during the stimulus block implies and expected hemodynamic reaction much weaker than in the stimulus, although the looming faces still contributed to keep the subject attention. In theory, any observed hemodynamic response response could be due to the faces regardless of whether the inverting checkerboard pattern is present. This is not the case as the hemodynamic activity that has been observed localized to the visual cortex does indeed depend on the presence of an inverting checkerboard pattern on screen and it does not appear to be manifest before the appearance of the flickering checkerboard.

Differences in the blood flow index response to visual stimulation experiments compared to sham and to the temporal channel (fig. 4.5) suggest that using this paradigm I am able to detect the effects of a cerebral hemodynamic response in the visual cortex. Increase of BFi of 15% on average and up to 30% in some selected cases (fig. 4.4) with a duration of few seconds and a slow decay to baseline is in agreement of what has been seen in previous visual stimulation functional DCS studies on adults [7].

The preparation time of each experiment was kept as short as possible in order not to increase the attrition rate of the protocol. As a consequence, good optical contact (i.e. removal of hair) could not be ensured prior to the start of the acquisition for all the measurement locations, as it is usually performed in functional optical and EEG studies on adults. For this reason I relied on redundancy (by using detector bundles and multiple locations) and on semi-automatic data quality assessment on a case-by-case basis.

Even though I have managed, by compromising on experimental design and optimizing (i.e. reducing) epochs duration while aiming aiming for the lowest rejection rate, to accept all scanned subjects (they all complied to pay attention to at least one epoch) and 56% of the number of epochs presented, I resorted on analyzing just one epoch, the first, for each experiment. This is driven by the existence of systematic slow drifts in the hemodynamic signal ($\Delta rBFi$). In many cases, such drifts seem correlated with the block paradigm, despite randomization of the duration of the recovery block. I believe that this is due to the effect of the previous blocks, as seen for example in fig. 4.5 where, after being altered by the presentation of the first stimulus (first epoch), the BFi fails to get back to baseline values in time for a new block to start. One reason that led me to this conclusion is that, if all valid epochs of all the subjects are averaged together, the $\Delta rBFi^{(i)}$ shows a negative reaction with respect to the stimulus [143]. Negative hemodynamic responses have been observed in mice at various early developmental age [130]. In infants, using sedation and arterial spin labeling and using a very similar visual block stimulation paradigm [144] it was shown that the blood flow can decrease upon activation. However, claiming this in our case is not consistent with results: when averaging only the first epoch, no such behavior can be guessed from the data. Were such a decrease of BFi of physiological origin, it would have been manifest also in this case. I believe that the compromises made on the experimental design were excessive, and that a longer waiting time between epochs, even if detrimental to the attrition rate, is needed in order to exclude effects of spurious BFi variations that correlate with the stimulus. I believe further study is needed in this direction, as, to the best of my knowledge, this is the first time that the hemodynamic response in terms of blood flow changes is investigate in the awake developing human brain.

Ultimately, the 8-channel USB correlator has been found to be suboptimal for this application due to the delays in communicating with the acquisition PC. This resulted in a non-steady sampling period (relative error 8%) that impeded the use of digital frequency filters on the data, i.e. band pass to remove the slow drifts and at the same time high frequency noise. For this reason I had to resort using moving average filters, and to consider only the epochs with no evident superimposed slow drifts in a 10 s baseline before the onset of STM. Moreover, if the inter-sample time is compared with the integration time, at each acquisition an average of 181 ms of data are lost, presumably due to the communication time delay between the correlator and its software interface. In conclusion, the usability of the USB correlator is limited at least for infant functional studies, for which a high sampling rate is desirable i.e. to limit the effects of any fast, jerky movement of the head to a single data point.

The range of variation of the rBFi responses to the stimulus for a single experiment, as reported in fig. 4.4 (b) and (c), is rather big (30% for a 30% increase seen at hemodynamic response peak). As a outlook, further optimization of the DCS device, like increasing the number of detector channels used in parallel and using more precisely timed correlators in order not to reject a considerable fraction of the experiment time, are being considered. Also increasing the sampling frequency and using automated rejection algorithms for those data points exhibiting high values of accelerometer reading can hopefully increase precision and accuracy of single experiments and their resilience with respect to noise. The detected hemodynamic responses were also larger than expected, thus requiring a longer inter-stimulus interval that, despite it can likely negatively affect the attrition rates, allows using the average of more than one epoch per subject in the data analysis.

Chapter 5

Broadband hybrid diffuse optical spectroscopies of bone properties

This work was made possible by the fruitful collaboration with Dra. Eugenia Negredo, Núria Pérez-Alvarez, Dra. Anna Bonjoch, Dra. Patricia Echeverría, Dr. Roser Escrig, Dr. Bonaventura Clotet from Lluita contra la Sida foundation (LSF, Germans Trias i Pujol University Hospital, Badalona, Spain), Dr. Joaquim Rosales from Digest (Badalona, Spain), Dr. Sanathana Konogolu Venkata Sekar, Dr. Andrea Farina, Dr. Paola Taroni, Dr. Antonio Pifferi from Policnico di Milano (Milano, Italy), and Dr. Claus Lindner of ICFO (Castelldefels, Spain). Part of this work was disseminated in a peer-reviewed journal paper that I contributed redacting [39]. In this chapter I describe the methods and discussing the results of a multidisciplinary approach involving diffuse optics for the study of the detrimental effects of human immunodeficiency virus (HIV) infection on the well-being of bone tissue *in vivo*.

5.1 Introduction

In the last 15 years there has been a decrease in the rate of deaths from acquired immune deficiency syndrome caused by HIV infection in the world (1.9 million people per year at its peak in 2004) [145]. Although a decrease in new infection rate has also been observed, the number of people living with HIV is increasing and has reached 36.9 million people in 2017 [145]. If treated, like it is common in a high-income setting, a HIV-infected person has nearly the same life expectancy of a uninfected person [146].

Among the aspects that still contribute to their lower life expectancy , HIV-infected subjects are a high-risk population for low bone mineral density (BMD) [45, 46, 47, 147] and low-energy bone fractures [147, 48, 49]. It is known that some antiretroviral drugs [148, 149, 150, 151, 152, 153, 154], the virus itself, and the maintained systemic virus-related inflammation [155, 154, 156] promote bone loss, which is manifest through multiple factors, like the loss of BMD [45, 46, 47, 147]. A prevalence of osteopenia/osteoporosis among HIV-infected population is indeed well documented [48, 49]. Knowing, as early as possible, the status and progression of the disease can therefore be important to reduce the morbidity and mortality.

A wide range of non-invasive and invasive techniques can be used to monitor bone health and predict the risk of low-energy bone fractures. Each method has particular advantages and disadvantages. The most widely used method is dual-energy X-ray absorptiometry (DXA). This technique determines BMD as an indicator of the quantity of minerals in the bone, and, consequently, of the risk of bone fracture according to the BMD. Nonetheless, bone strength and fracture risk are a function of both BMD (degree of mineralization) and architectural structure (quality of bone) [157, 158]. Bone mass, geometry, and tissue material properties all contribute to bone structural integrity. Current available tests provide an incomplete evaluation of the status of the bone tissue, since some of its qualities like architecture, turnover, damage accumulation and mineralization, are not directly evaluated by DXA. A high incidence of vertebral fractures was for example found in HIV-infected subject that exhibited normal or slightly reduced BMD [159].

Tissue vascularization and local micro-vascular hemodynamics play an additional determining role in the bone health [158, 160]. Alterations at this level can lead to disturbances in bone metabolism. Osteoporosis is characterized by changes of the hemodynamics and by the reduction and transformation of mineral in bone matrix [158, 160]. Bone vasculature plays a vital role in bone development, remodeling and homeostasis [161, 162]. In fact, some studies have demonstrated that angiogenesis precedes the onset of osteogenesis [163]. Angiogenesis, then, is key to not only physiological bone growth and remodeling, but also pathological bone disorders. In particular, reduced skeletal blood flow has been associated with reductions in bone mass and increased risk of fractures in elderly people [164]. Age-related decrease of the microcirculatory perfusion of bone preceded the loss of BMD, indicating their possible causal relationship [165]. A better understanding of changes in hemodynamics and bone matrix material properties can result in a earlier detection of the alterations of bone well-being and could help to better manage bone pathologies.

However, the information about the bone hemodynamics is limited: most techniques of circulatory research are difficult to apply to bone. The gold standard for experimental measurement of bone blood flow is the radioactive microsphere technique, which is invasive and exposes the body to ionizing radiations. Novel techniques are being studied, such as dynamic computed tomographic perfusion, laser and ultrasound Doppler velocimetry, and NIR-DOS/DCS [42].

Over the last decades, near-infrared diffuse optical spectroscopy (NIR-DOS) has emerged as a promising technique useful in different clinical scenarios. It can offer information on a variety of tissues including the measurement of local concentrations of oxy- and deoxy-hemoglobin ([HbO_2] and [Hb], respectively), water, lipid, collagen and other light absorber concentrations in tissue [5, 7, 35, 36, 37, 38, 20, 17, 39, 40, 41]. A relatively newer diffuse optical technique, diffuse correlation spectroscopy (DCS), allows the direct measurement of local microvascular blood flow [7, 5]. Hybrid NIR-DOS/DCS has been applied to a growing number and wide variety of biomedical and clinical problems like cerebral oxygen metabolism [14], breast cancer monitoring [83] and early detection of thyroid gland malignancies [19]. Our group has already described assessment of physiological properties of the healthy bone (patella and manubrium) in healthy subjects [38, 20] by this technique. The current study evaluates for the first time the clinical usefulness of this tool in HIV-infected and osteoporotic subjects. In this study, to find out relations between osteoporosis and bone physiological parameters, subjects with normal BMD or osteoporosis shall be compared, and due to the high prevalence of osteopenia/osteoporosis among HIV-infected population, for which the knowledge about the underlying physiological mechanism is scarce, HIV-infected individuals were compared with uninfected subjects. This is the first time that HIV-infected subjects are measured by non-invasive DOS/DCS to assess the relationship between bone loss and bone physiological parameters.

It has been hypothesized by our collaborators in Lluita contra la Sida foundation, Politecnico di Milano and ICFO that osteoporosis is a condition associated with a lower tissue perfusion and altered tissue constituent concentrations. The objective of this chapter is to find out if alteration on bone and related systemic indicators are correlated with optically assessed indicators (oxygen saturation, blood flow, blood volume, water, lipid, collagen concentrations and reduced scattering and absorption coefficients) that can be noninvasively measured by combining NIR-DOS and DCS.

5.2 Methods

Study design and participants

This chapter describes an observational, comparative, case-control, proof-of-concept study. HIV-infected individuals were considered appropriate candidates for this study if they maintained viral suppression (plasma HIV RNA <40 copiesmL^{-1} for more than 6 months) while the history of a recent ($<$ 6 months) acute illness was a criterion for exclusion.

The study was approved by the Institutional Ethics Committee of hospital Germans Trias i Pujol (ID CEIC: PI-14-055) and the local health authorities, and all participants signed written informed consent. The present study has been carried out in-line with Declaration of Helsinki principles

Clinical history and demographics

DXA scan using a commercial scanner (GE LUNAR DPX PRO, software version 12.3) were carried out by our collaborators at Digest to assess bone mass in all participants. Hip and lumbar spine BMD and T-scores were recorded. Subjects were classified, according to the WHO criteria, as: normal BMD, when hip and lumbar spine (L1-L4)

T-scores were > -1.0 standard deviations, osteopenia, in case of a hip and/or lumbar spine (L1-L4) T-score between -1.0 and -2.5, or osteoporosis, in case of a T score < -2.5.

A health questionnaire was handed to each subject asking them to fill it prior to the study. The following demographic and clinical history information was therefore collected: gender, date of birth, comorbidities (diabetes, hypertension, chronic hepatitis, renal and lung disease) and concomitant treatments, as well as body mass index (BMI), smoking habits, consumption of illicit drugs, alcohol intake, amount of exercise practiced. The date of the diagnosis of HIV infection, risk group and antiretroviral history were collected in cases of HIV infection. The following parameters were also recorded in HIV-infected subjects: routine hematology and biochemistry results, viral load of HIV-1, CD4/CD8 T-cell counts and serology of hepatitis C and B virus.

A total of thirty consecutive HIV-infected subjects who attended Germans Trias i Pujol HIV unit from June to August 2014 accepted to participate in the study, as well as twenty-three uninfected subjects to be used as controls. Nine subjects (16.9%) met the osteoporosis criteria in DXA scan, 5 HIV-infected and 4 HIV-negative. Subjects of a wide range (minimum, maximum) of ages (21,78 years old) were recruited to also evaluate the impact of age on the estimated parameters; 6 of the participants aged less than 30 years and 4 aged more than 70 years.

Optical instrumentation and protocol

A broadband time-resolved DOS device developed by the Politecnico di Milano group was utilized alongside a portable DCS device that was custom built by the group at ICFO. I personally carried out with Claus Lindner and Sanathana Konuolu Venkata Sekar the data acquisition campaign in the ICFO laboratories. The details of both devices and analysis methods are described in detail elsewhere [17, 39, 7]. Compared to other body locations, radius distal has superficial bone with high photon penetration depth, but the nature of current study demanded a bone location where the pathological and systemic changes are observed earlier. For this reason, trochanter was chosen as the target bone prominence for the present study. The penetration depth of the hybrid instrument was sufficient to probe this bone as it can be seen in Fig.2 in ref. [39].

Each subject was asked to stand still and relax, breathe normally while the optical measurements were made in the trochanter region. The trochanter was located as a bony notch, identifiable by touch, along the lateral aspect of the thigh. A black foam pad hosting the source and detector fibers for DCS and TRS was then located on top of it. Source and detector fibers at an inter-optode distances of 25 mm were aligned along the cranio-caudal direction. Overall acquisition time per subject (comprising protocol explanation, signing the informed consent, health checklist, and measurement time) was in every case less than an hour (60'). For TRS, the scan over the 60 wavelengths took always less than 8 min. For DCS, 3 repetitions of 7 s allowed us to acquire three DCS curves per subject. Results of the fitting of each curve were averaged.

For NIRS-DOS, time resolved reflectance was fitted to a theoretical model [68], taking in account also the instrument response, to extract absorption (μ_a) and reduced scattering (μ_s') coefficients at multiple wavelengths. The concentrations of constituents of tissue (water, hemoglobin, collagen and lipids) were quantified by fitting the in vivo absorption spectrum with the linear combination of the spectra of each constituent [39]. The empirical power law derived from Mie light scattering theory,

$$\mu_s' = a \left(\frac{\lambda}{\lambda_0}\right)^{-b} \tag{5.1}$$

where λ is the wavelength of light and $\lambda_0 = 600\,\text{nm}$, was considered as a model for the reduced scattering spectrum [58]. Scattering amplitude (a) and scattering power (b) are estimated as best fit parameters. The scattering amplitude is proportional to the concentration of scattering particles, while the scattering power decreases when the effective average radius of scatterers increases [58, 37]. In biological tissues the scattering parameters can provide information on the microscopic structure of tissue and reflect also its composition. For example, in the cancellous bone in the human calcaneous, previous investigations with NIRS-DOS highlighted how the measurement of the scattering power (b) can provide insight on the structure and composition of bone. Specifically, the bovine inorganic bone matrix has the lowest scatter power among the other constituent of the bone that can contribute to the optical signal: water, blood, collagen and fat [37].

For DCS, a solution of the correlation diffusion equation [166, 5] for a semi-infinite medium geometry, computed by using the absorption and scattering values obtained by NIR-DOS at a wavelength of 785 nm, was used as a model to fit correlation data. From this fit I have obtained an estimate of the microvascular blood flow index (BFi).

The following physiological parameters were measured optically by NIR-DOS/DCS in the trochanter from all participants: 1) reduced scattering and absorption coefficients (μ_a and μ_s') in the 600 nm to 1200 nm spectral window, 2) hemodynamic parameters (BFi, [Hb] and [HbO_2], total hemoglobin concentration, THC = [Hb] + [HbO_2], and percentage of tissue oxygen saturation, StO_2 = [HbO_2] / THC x 100),

3) concentration of tissue constituents: water, lipid and collagen; and 4) Mie coefficients of scattering (amplitude a and power b, see above).

Statistical analysis

Parameters estimated by optical spectroscopy were compared among HIV-infected and HIV-negative subjects, affected or not by osteoporosis or osteopenia. In addition, demographic and clinical data, including bone parameters (e.g. BMD at the location of the optical measurement, the trochanter, assessed by DXA) were also included.

I have used t-tests and linear regression models. Optically estimated parameters were taken as the dependent variables while HIV infection status, demographics and clinical variables were fitted as predictor variables or regressors. I have removed the extreme values (5% top and bottom) from the optically estimated parameters to mitigate the effect of extreme values on correlations.

The p-values and confidence intervals were calculated for a bilateral confidence level of 95%. Findings that are failing to reach statistical significance after Bonferroni adjustment for multiple comparisons (N=8) are detailed. I have considered significant correlations among optical variables and predictor that have p-value <0.05 and pass a Shapiro-Wilk test of normality of residuals. If an optical variable was found to be statistically significantly correlated with more than one predictor, a multi-variate linear model regression was considered if it explain the data in a better way than the two single-variate linear regression, as determined by an ANOVA test. I have considered variance inflaction factors when there was a suspected collinearity between regressor variables.

The R software version 3.5.1 was used for data analysis [167, 168].

5.3 Results

Table 5.1 summarizes epidemiological and clinical characteristics of study participants. All reported values are medians and inter quartile ranges (IQR, in parenthesis), except where specified otherwise.

Hemodynamic parameters, concentrations of tissue constituents and scattering parameters (a and b) are reported for all participants stratified by HIV infection status (tables 5.2 and 5.3).

I have found 14 statistically significant correlations among dependent variables and regressors. Among these, two (THC and osteopenia, water concentration and osteoporosis) have skewed distribution of the residuals and therefore are not further considered. Results are reported in table 5.4.

Multivariate regression has been carried out for StO_2 with respect to HIV infection status and age (for this considering also the interaction term as the HIV-infected population is significantly older, p=0.037), and for [Hb] with respect to HIV infection and BMI (no evident collinearities among the regressors in this case). Results are reported in table 5.5.

5.4 Discussion

This exploratory evaluation of HIV-infected and HIV-negative individuals, with and without systemic osteoporosis or osteopenia, found associations between low BMD and higher [Hb] and higher water and collagen concentrations. In addition, HIV infection was associated with reduced tissue oxygenation StO_2 in a similar way to old age. According to these results, HIV has a detrimental effect on bone hemodynamics that is comparable with age. Findings therefore agree with the well-known fact that elderly people have a decreased oxygen supply [169, 170]. However, tissue saturation decreases and [Hb] increases much more markedly with HIV infection than with age. No association was found with microvascular blood flow. This supports the hypothesis that there is an increased oxygen consumption that is not met by the higher blood flow supply. Moreover, the reduced tissue oxygen saturation of bone tissues among the HIV-infected people could explain the faster bone loss observed in this population, similarly to those observed with aging. However, these data do not allow us to state a causal relationship. I believe further studies in this direction are needed.

No direct correlation is visible among hemodynamic parameters and bone mineral density of the trochanter. Nevertheless, the scattering power decreased with bone mineralization and increased in osteoporotic subjects, independently from HIV infection status. This effect seems to be congruent with the fact that bone mineralization contributes to the decrease of the scattering power more than any other component, as noted first by [37]. The fact that b is also correlated with gender, increasing in males, can be due to the fact that in our sample males have statistically more mineralized bone matrix (p=0.008), as it is also well known to happen in the general population. As a general observation, higher b means smaller size of the scattering centers. This is typically observed when the mineralized bone matrix, yielding large scattering centers and consequently low b values, is replaced by more fibrous structures, like cartilage or muscle fibers. However, many distinct conditions related to tissue microstructure (such as density and size of bone trabeculae, subcellular organelles, adipose cells, etc.) may affect the scattering properties. Thus, without further information, it is difficult to identify the exact microscopic origin of the observed scattering differences and correlation with pathology. However, the results obtained so far provide a preliminary indication of the sensitivity of the scattering properties to bone pathological conditions, and of their potential usefulness for the monitoring of HIV-infected subjects.

Collagen concentration in the trochanter is found to be significantly higher in people with systemic osteopenia, once again independently from the HIV infection status, and negatively correlated with trochanter BMD. An attempt to explain this behavior with a multivariate analysis did not succeed, probably due to high collinearity between the two regressors (variance inflation factors for osteopenia and interaction term $>$10, 62 and 49.8 respectively).

In addition, a direct relation, not dependent on HIV infection status, was found between water concentration and osteopenia. It should be taken into account that the reduction in bone mineral density associated with osteopenia leads to an increase of the relative weight of other bone constituents, such as water and collagen, in determining the overall bone tissue mass and density. However, the present implementation of NIR-DOS does not offer information about the properties of this collagen and, although collagen cross-links (and therefore high collagen concentrations) are determinants of bone quality, it could be detrimental collagen, which is involved in many age-related diseases such as osteoporosis and cardiovascular disease [171, 172]. No correlation was found between water and/or collagen concentrations and systemic osteoporosis, maybe due to the small amount of subjects affected by it in the study population. This point merits a further detailed study.

As a secondary consideration, smoking habit was correlated with lower lipid concentration. It is known that smoking population has lower body and bone fat content [173]. Smoking habit has also been found to correlate with increased [Hb], although no statistically significant relation has been observed for microvascular blood flow or tissue oxygen saturation. Likely, the small sample size of the study prevented us from uncovering some of these correlations.

The main limitation of the present study resides in the heterogeneous nature of the probed tissue volume, whereas the optical measurements are analyzed using a homogeneous model of photon migration. This can possibly cause some contamination from the superficial tissue layers (skin, subcutaneous fat) in the assessment of bone properties. Nevertheless, the time-resolved NIR-DOS permits to explore tissue focusing to its deep layers, optimizing independence from the most superficial structures [39, 16].

In conclusion, a better knowledge of the microvascular hemodynamic and metabolic physiology of bone as well as of the correlation between bone health and its composition and microstructure is needed in order to design new strategies to prevent bone mineral density loss leading to osteopenia and osteoporosis, especially in patients at high risk such as HIV-infected subjects. In addition, new techniques are necessary to better assess bone health: a considerable number of patients who present an osteoporotic fracture do not show osteoporosis criteria by DXA scan [159]. Taking all this into consideration, I believe that the noninvasive, non-ionizing, hybrid NIR-DOS/DCS might offer information about both issues: to assess the physiological mechanism of bone loss and to early identify qualitative problems of bone, offering complementary information to DXA scan. Considering that alterations on blood perfusion probably precede a decreased BMD

[174], low tissue oxygen saturation or blood flow in bone could be predictive of osteoporosis and could help us identifying subjects at high risk of bone loss. Similarly, water and collagen content in bone may prove useful to diagnose osteoporotic or pre-osteoporotic bone status. However, due to the exploratory nature of this study, further larger studies in terms of number of subjects, especially among the osteoporotic ones, have to be conducted to corroborate our results.

	HIV-infected (N=30)	HIV-negative (N=23)
Age, years	48 (40;55)	29 (25;45)
Male gender, no. (%)	22 (73)	17 (74)
Time since diagnosis of HIV infection, years	13 (5;22)	-
Time on antiretroviral treatment, years	11 (4;18)	-
Lymphocyte CD4 T cells, cellsμL^{-1}	642 (452;863)	-
Suppressed VL (<50 copies/mL), %	100	-
BMI, kg m^{-2}	24 (22;27)	25 (22;27)
Osteoporosis, no.	5	4
Trochanter BMD, g cm^{-2}	0.85 (0.73,0.91)	0.82 (0.72,0.89)
Trochanter T-score	-0.6 (-1.8,0.1)	-0.8 (-1.6,0.4)
Heart rate, min^{-1}	70 (63;76)	68 (64;77)
Arterial oxygen saturation, %	98 (97;99)	99 (98;99)
Hypertension, no.	6	2
Diabetes, no.	0	0
Dyslipidemia, no.	12	1
Smoking habit, no.	7	2
Regular exercise, no.	27	19

Table 5.1: Baseline characteristics of HIV-infected and HIV-negative subjects. Median (IQR 25%;75%) reported, except where specified. (VL, viral load; BMI, body mass index; BMD, bone mineral density, no.: number of).

	All subjects	HIV-negative subjects	HIV-infected subjects
Water, $\mathrm{mg\,cm^{-3}}$	157 (125, 224)	133 (115, 173)	187 (132, 224)
Lipids, $\mathrm{mg\,cm^{-3}}$	885 (830, 955)	895 (852, 955)	881 (805, 951)
Collagen, $\mathrm{mg\,cm^{-3}}$	30.1 (12.8, 49.4)	24.6 (13.8, 47.1)	32.5 (12.0, 49.6)
Scattering amplitude (a), $\mathrm{cm^{-1}}$	10.8 (9.9, 11.5)	10.6 (9.9, 11.0)	11.1 (10.3, 11.7)
Scattering power (b), $\mathrm{cm^{-1}}$	0.61 (0.55, 0.72)	0.64 (0.57, 0.71)	0.60 (0.52, 0.72)

Table 5.2: Tissue constituent concentrations and scattering and absorption coefficients for all participants and stratified according to the HIV infection status. Median (IQR 25%;75%)

	All subjects	HIV-negative	HIV-infected
Deoxy-hemoglobin concentration ([Hb]), µM	3.98 (2.82, 4.89)	2.98 (2.46, 3.54)	4.52 (3.48, 5.78)
Oxy-hemoglobin concentration ([HbO_2]), µM	6.42 (5.08, 9.52)	6.40 (5.12, 7.74)	7.24 (4.89, 10.00)
Total hemoglobin concentration (THC), µM	10.05 (8.16, 13.28)	8.64 (7.69, 10.68)	11.37 (9.19, 14.53)
Oxygen saturation (StO_2), %	65 (58, 73)	69 (63, 74)	60 (57, 67)
Blood flow index (BFi), $1 \times 10^{-9}\,\mathrm{cm}^2\,\mathrm{s}^{-1}$	2.79 (2.08, 3.94)	2.64 (1.89, 3.49)	3.09 (2.31, 4.32)

Table 5.3: Hemodynamic parameters for all participants and stratified according to the HIV infection status. Median (IQR 25%;75%).

Dependent variable	Regressor variable	p-value	R2	Effect Size (Standard Error)
[Hb]	HIV infection	0.0002	0.26	1.69 (0.41) µM
b	Trochanter BMD	0.0005	0.24	0.37 (0.1) $cm^2\,g^{-1}$
Lipids concentration	Smoking habit	0.0040	0.19	-119 (33) µM
StO_2	Age	0.0033	0.16	-0.28 (0.09) %/year
b	Gender:male	0.006	0.14	0.09 (0.03)
Collagen concentration	Osteopenia	$0.019^{\dagger}$	0.11	17 (7) $mg\,cm^{-3}$
[Hb]	BMI	$0.016^{\dagger}$	0.10	-0.16 (0.06) $\mu M\,cm^2\,g^{-1}$
[Hb]	Smoking habit	$0.023^{\dagger}$	0.09	1.4 (0.6) µM
Water concentration	Osteopenia	$0.026^{\dagger}$	0.09	48 (21) $mg\,cm^{-3}$
Collagen concentration	Trochanter BMD	$0.033^{\dagger}$	0.08	-58×10^{-3} (26×10^{-3}) cm^{-1}
b	Osteoporosis	$0.041^{\dagger}$	0.07	-0.09 (0.04)
StO_2	HIV infection	$0.05^{\dagger}$	0.06	-6 (3) %

Table 5.4: Statistically significant correlations between optically assessed parameters and regressors. R2 is the adjusted coefficient of determination. Correlation that fail to reach statistical significance after Bonferroni correction for multiple test (N=8) are marked with †

	StO_2 (%)	HIV + Age + Age:HIV			[Hb] (µM)	HIV + BMI	
	Estimate	SE	p-value		Estimate	SE	p-value
(Intercept)	0.84	0.047	$<5 \times 10^{-4}$	(Intercept)	6.5	1.4	$<5 \times 10^{-4}$
HIV, infected	-0.26	0.088	0.0054	HIV, infected	1.6	0.4	$<5 \times 10^{-4}$
Age, years	-0.004	0.001	$<5 \times 10^{-4}$	BMI, $\mathrm{kg\,m^{-2}}$	-0.14	0.06	0.017
HIV:Age	0.005	0.002	0.013				

Table 5.5: Multivariate linear model regression results. SE is the standard error. Interaction terms are reported and marker as "regressor1:regressor2" when they provide for a better explicative model as per ANOVA test.

Chapter 6

Diffuse correlation spectroscopy standard with long shelf life

6.1 Introduction

The work presented in this chapter has been made possible with the collaboration with Dr. Sanathana Konugolu Venkata Sekar, Dr. Antonio Pifferi, and Dr. Lorenzo Spinelli from Politecnico di Milano, and presented at OSA 2016 conference (Fort Lauderdale, Florida, USA) [175].

In medical optics, tissue phantoms are produced to replicate the optical properties of specific tissue and are commonly used to assess instrument reliability, to compare imaging systems and to train personnel. Phantoms can be defined as reference materials [176] or as artifacts that are used to evaluate the measurement performance of measuring systems for specific tasks [177]. Phantoms are researched to conveniently mimic tissue in the visible and near infrared regions of the electromagnetic spectrum. A phantom is generically requested to be reproducible, easy to supply and possibly low cost, and to have accurately determined and stable optical properties [50]. Cerussi *et al.* [178] identified three main field of applications for tissue mimicking optical phantoms: i) validation of an instrument, which includes calibration and quality assessment, ii) standardization of procedures and training of users and iii) assessment of the constancy of the performance of a measuring instrument between various centers that take part to the same study. Employing appropriate phantoms is a sensible requirement for any project aiming at the translation to clinical setting of a biomedical technology, and therefore phantom engineering constitutes, by any means, one of the technological challenges that a traslational project has to face.

Many phantoms preparations exist for near infra-red spectroscopy. The general procedure consists in starting with a bulk medium, ideally with no light-scattering properties and transparent in the whole optical spectrum of interest, and adding scattering and absorbing centers in precise and controlled quantities according to their known absorption ($\epsilon_a(\lambda)$) and scattering ($\epsilon_s(\lambda)$) spectra. Phantoms based on liquid media are appreciated because they can be more easily homogenized by mixing. Among the phantoms of most widespread use, it is worth citing liquid suspensions of microspheres, as for example polystyrene beads used for example in [77] and [78], and water suspensions of micelles of lipids used for intravenous nutrition [179, 101]. Gel matrices of Agar and Intralipid [180] are a bridge between liquid and solid matrix phantoms, they can be homogeneized while in their liquid form, and they solidify quickly after. Solid phantoms can be made of epoxy resin or silicone and can be seeded with e.g. titanium dioxide particles as scatterers [181, 180, 182, 183]; the polymer matrix quickly cures generating solid phantoms that generally have the longest shelf life. Despite the fact that it is more difficult to obtain homogeneous optical properties throughout large volumes (on the order of 1 L, for photon migration studies) in solid phantoms, they tend to be more stable and resistant to contamination and evaporation than liquids. Liquid matrix phantoms, on the other side, can get contaminated easily and they eventually evaporate or, in case they are made of biological matter, quickly (days or weeks time) degrade or even rot. Intralipid phantom for example have been found developing superficial layers that alter their properties in a rather short time (∼1 h) [184].

For DCS and laser doppler flowmetry (LDF), a non invasive technology that detects a laser light re-emitted from superficial tissue that has been Doppler shifted by the scattering from red blood cells, some constraints must be added [102]. Phantoms in which scatterers of light are free Brownian diffusers are often used, as they generate a temporal decay of the autocorrelation curves of the intensity of light passing through them in a DCS experiment that is phenomenologically identical to what is observed in a blood perfused living tissue [81].

In LDF, light penetrates just few millimeters inside the human tissue at the typical wavelengths used (680 and 750 nm, [185]). Flux, velocity and concentration of RBC are extracted from the power spectrum of the photocurrent generated in the detector by the re-emitted light. Results are given in a scale of perfusion units (PU), which needs calibration in terms of absolute flow and/or speed values with respect to known standards. As reported in [186], mechanical flow models [187, 188] and carefully controlled animal preparations [189] can be used as an absolute calibration standard for laser doppler flowmeters. Another option is a rotating disc simulating scatterers moving with controlled velocity [190]. However, motility standards made by

Brownian diffusing microparticles are still the common method of calibration, e.g. the F1001 motility standard from Perimed (Perimed AB, Sweden) or the Probe Flux Standard (Moor Instruments, United Kingdom). They are sold from the same manufacturer of the corresponding LDF devices as valid calibration standards to be used in clinical setting. For LDF applications, however, the detected photons are Doppler shifted (heterodyne situation), as opposed to the case of tissue where the vast majority of the photons escapes un-shifted (homodyne situation). This results in a differently shaped power spectrum [191]. For these reason, liquid motility standards can be embedded in semipermeable polymers that introduce a certain degree of scattering from non-diffusing particles [192].

In diffuse optics, the situation is even more complex, because the high penetration of light (orders of 1 cm) requires phantoms with volumes of about ∼1 L in order for the effects of its borders to be negligible. Animal preparations are not a viable option. For the considered volumes, the cost of diffusing microparticles in suspension, which are well suited indeed for making tissue simulating phantoms [193], is expected to be non-negligible. A 5 mL vial of a solution of 2% monodisperse microspheres sells for 200 €, and it takes approximately 200 of these vials to reach μ_s'=10 cm^{-1} in one liter of solution [194].

On the other side, bigger volumes have bigger thermal inertia, therefore are more stable with respect to temperature variations. As noted by Friedriksson *et al.* in [195], the first and higher order moments of the spectral distribution that are used for evaluating the perfusion index during LDF calibration are depending heavily on some properties of the standard (temperature, concentration, status of particle aggregation) that need some experimental precaution to be kept constant.

In this chapter I report about experimenting with a synthetic phantom solution provided by Hemophotonics (Castelldefels, Spain). It consists in an essentially monodisperse, water based solution of microparticles that scatter light and undergo Brownian diffusion. By adding ink or a dye and by titrating the scatterers in solution I was able to tailor its optical properties in order to obtain a diffusive tissue simulating phantom that is suitable for DCS and has a long shelf life.

6.2 Materials and methods

A liquid phantom was made by mixing a suspension of inexpensive synthetic micro particles provided by Hemophotonics (Castelldefels, Spain) and India Ink (Pelikan Tusche A, Ultramarine color, Pelican, Germany) at a concentration of $33\,\mu\mathrm{L}\,\mathrm{L}^{-1}$ in $2\,\mathrm{L}$ of de-ionized water. The size dispersion of the micro particle dimensions was characterized for a very diluted sample by means of dynamic light scattering (DLS) using a Zetasizer Nano Zs (Malvern, UK).

A watertight plastic container for the phantom (outer dimensions $10 \times 17 \times 10\,\mathrm{cm}^3$, inner capacity of about $1.7\,\mathrm{L}$) was 3D printed using an extrusion printer of black poly lactic acid (PLA) filament. Optical measurements were then carried out through a semi-transparent Mylar (Dupont, USA) window measuring $3 \times 5\,\mathrm{cm}^2$ of lateral dimensions and $0.25\,\mathrm{mm}$ thickness. The window was glued to an opening on the top of the container, this way sealing it and keeping the liquid safe from risks of contamination or evaporation. A small magnetic agitator was included in order to allow stirring of the mixture while the phantom was sealed. Stirring was carried out for few seconds at least 5 minutes before every experiment. A time resolved spectroscopy (TRS) TRS-20 system (Hamamatsu Photonics K. K., Japan) was used for the analysis of the optical properties of the Phantom and a HemoFloMo

(Hemophotonics, Spain) for the acquisition of DCS curves. Two couples of straight fibers were wedged into a 3D printed probe with the imaginary lines between their tips describing a "X" on the surface of the Mylar window when in contact. The source-detector distances were 1.53 cm and 1.63 cm respectively for TRS and DCS. For TRS, only the fit of the 801 nm channel was considered. At each experiment, between 5 and 20 curves were acquired with 10 s integration time. For DCS, at least 30 curves with 1 s integration time were acquired in an experiment. The probe was replaced between experiments from 1 to 6 times per day. TRS and DCS measurements were carried out sequentially at least once per week. Two thermocouples (20 cm length, less than 1 mm in diameter) were sometimes inserted in the bulk of the liquid phantom passing through tiny holes drilled for the purpose to monitor temperature variations that could affect the scatterers dynamics. Optical properties from TRS measurements were averaged and used as input for fitting the DCS autocorrelation curves.

Another phantom watertight case, designed to last longer, was made by a film development box (approximate dimensions $15 \times 15 \times 17\,\mathrm{cm}^3$, inner capacity of about 2 L) and filled with a suspension of the same synthetic micro particles for achieving longitudinal stability. For this other phantom (see fig. 6.1) I resorted using water soluble Nigrosin (Sigma-Aldritch, USA), a dye used in phantom preparations [196], at $1.8 \times 10^{-2}\,\mathrm{mg\,mL^{-1}}$ concentration. Two thermocouples were embedded in the bulk of the liquid and were read by an Arduino controller board that saved the temperature in a log file in a SD memory card. A round window on a side of the enclosure (diameter 8 cm) allowed optical measurements to be carried out by simply laying the probe on it. The fact of being placed vertically also reduced bubbles formation at its interface. Optical properties were measured by an in house built TRS device (P-C-760 laser, PMA Hybrid detector and TH260

TCSPC, Picoquant, Berlin, Germany; a 62.5 µm graded-index and a 1 mm plastic optic fibers were used as source and detector, respectively) at 1.6 cm source detector separation and resulted to be μ_s'=14.4 and μ_a=0.2 cm^{-1}. A custom made DCS device comprising 785 nm 120 mW Crystallaser CW laser, a step index 90° bent 10 m long multimode source fiber, two 10 m long 90° bent 780HP single mode single fiber (channel 1 and 2) and a two-bundle of the same fibers (channel 3 and 4), was used to measure the phantom. All the four detection channels were connected to SPCM-AQ4C 4x SPAD module (Excelitas, Canada) and a Flex-05 8-channel USB correlator (Correlator.com, USA) managed by a Visual Basic frontend in a Windows PC was used to acquire the correlations. Twelve DCS measurements of at least 60 s, 1.9 Hz sampling rate, were carried out at approximately 1.5 ± 0.1 cm source detector separation during 136 days. The phantom was resting in a laboratory room without air conditioning. The temperature was found to vary in the room in the range 19 to 25 °C.

In order to make use of the scattering particles in a liquid phantom a recipe matching the particle concentration with the scattering properties is needed. To obtain such a recipe I decided carrying out an optical characterization of various concentrations of scatterers in water by using the linear TRS method described in section 2.1.3 and more in detail in [71]. Optical instrumentation from Politecnico di Milano that I used for the characterization is described here. A compact photonic crystal based pulsed supercontinuum fiber laser (SC450, Fianium, UK) driven at 40 MHz repetition rate was used as a broadband source. A very narrow response photomultiplier connected to a 1 mm fiber was used in detection. The device is described in detail in [197]. Measurements were carried out at two source detector separations ρ=10, 20 and 30 mm in the 600 to 900 nm range, with λ steps of 25 nm.

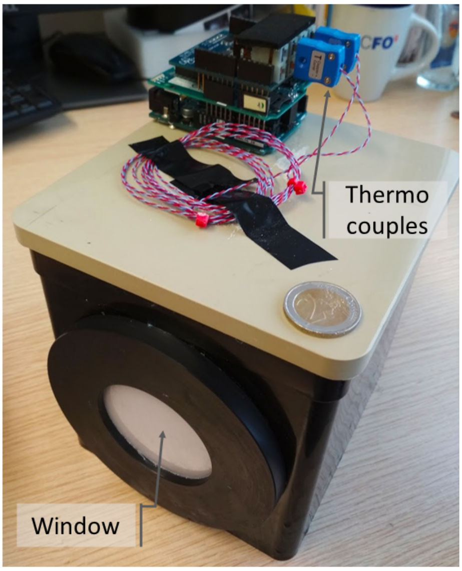

Figure 6.1: The phantom in the watertight casing used for the longitudinal (136 days) assessment of DCS repeatability.

6.3 Results

Particle sizing by DLS determined the effective size of the light scattering particles provided by Hemophotonics. Results are reported in fig. 6.2. The average dimension of the scattering particles was found to be 466 nm with a low polydispersity index (PdI), define as the square of the ration of the standard deviation over the mean of the size distribution, of less than 0.07; this value suggests a relatively uniform distribution of particle sizes [198].

Time resolved spectroscopy characterization of the reduced scattering coefficient yielded a spectral dependence of μ_s' that can be effectively fitted by an effective Mie theory (eq. 2.3). From the coefficient

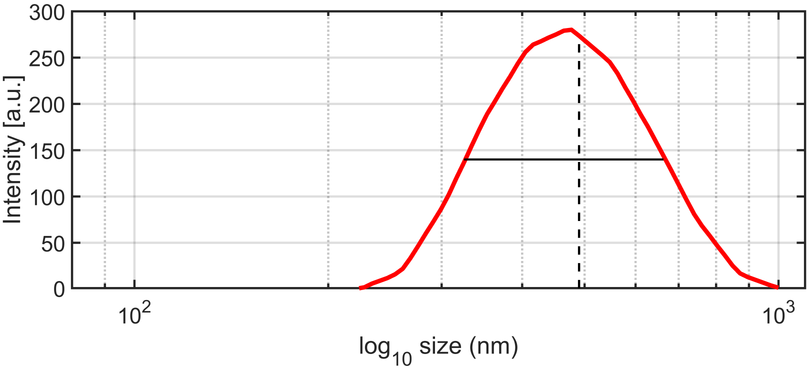

Figure 6.2: Particle size distribution obtained by DLS measurement on a diluted sample. Average particle size was 466 nm with a distribution FWHM of 115 nm, corresponding to a rather low polydispersity index PdI of less than 0.07.

reported in table 6.1, the expected reduced scattering μ'_{s} can be computed for any concentration of the scatterer in water that has been tested (1.63, 2.27, 2.78, 3.49, 4.62, 5.76 and 6.89%, weight/weight). Sample distribution of times-of-flight and instrument response function for 2 source-detector separations and 7 wavelengths are reported in fig. 6.3 along with the linear fit of the recovered μ'_{s}.

a, $[\mathrm{g\,g^{-1}\,cm^{-1}}]$	b
720 ± 20	2.93 ± 0.12

Table 6.1: Results of the fit with the effective Mie theory of the spectral dependence of $\epsilon_s(\lambda)$ according to eq 2.3 for a reference λ_0 of 600 nm. The reduced scattering coefficient μ'_{s} can be obtained as $\epsilon_s\, c_s$, where c_s is the weight ratio concentration of scatterers.

The precise optical characterization based on the linear TRS model did not give reasonable results when I tried to quantify absorption by titrating dye. This is arguably due to the spectral shape of the absorption for dye that I have chosen (Nigrosin), which seriously limits light transmission in the lower λ portion of the spectrum. Combined with the also increasing scattering when λ is smaller, this resulted in a poor TRS signal-to-noise ratio for the smallest wavelengths in the measured spectrum. A recipe for Nigrosin was then found by measuring the absorbance of non-scattering diluted samples at various concentrations with a portable spectrometer (Jazz, Ocean Optics, USA) and a white lamp. At 801 nm the fit of the linear relation between μ_a and water concentration of dye ($\mathrm{g\,mL^{-1}}$) yielded a proportionality constant P_1=$1.31 \pm 0.25\,\mathrm{mL\,g^{-1}\,cm^{-1}}$ and an intercept compatible within the error with water absorption at that wavelength [108].

The average values, obtained by averaging the results of all TRS acquisitions, of optical properties over 70 days were $0.058 \pm 0.004\,\mathrm{cm^{-1}}$ (relative error, RE, 7%, computed as standard deviation over average) and $14.6 \pm 0.8\,\mathrm{cm^{-1}}$ (RE 5%), for μ_a and μ'_s, respectively. The value of the average estimated particle Brownian diffusion coefficient, D_B, was $1.96 \pm 0.28 \times 10^{-8}\,\mathrm{cm^2\,s^{-1}}$ (RE 14.6%). Results are plotted in fig 6.5. Notably, the D_B had a RE within an experiment of, on average, 1.8%, independent on the time window considered (30, 60 and 500 s). Linear regression of D_B with respect to time showed a non statistically significant trend (R-square=2.33×10^{-2}).

In a separate experiment, I let the first phantom that was previously cooled to 14 °C to thermalize at the ambient temperature (23.5 °C). A sharp increase of the Brownian diffusion coefficient was seen as expected. When corrected for temperature and viscosity of water [199] by using the well-known Einstein's formula [200] the variation of D_B

Channel	CR, [kcps]	Avg. daily RE, [%]	Avg. total RE, [%]
CH 1	170	5	8
CH 2	360	5	13
CH 3	153	5	12
CH 4	130	5	11

Table 6.2: For each channel of the longitudinal DCS measurements on the second phantom (20 weeks), average (avg.) count rate (CR), avg. daily relative error (RE) and avg. total RE are reported.

cancels out on this temperature range (see fig 6.6).

Between January 19th and June 4th, 2018, the second phantom was scanned twelve times in twelve different days. Relative changes of D_B are represented in fig. 6.7 where the errorbars represent the RE during the same measurements. Average count rates (CR) varied between 360 kcps (CH 2, shortest source-detector separation) to 130 kcps (CH 4, largest source-detector separation). Average (avg.) per-day and total RE are reported in table 6.2.

6.4 Discussion

Although in the multiple scattering regime where DCS works the dispersion of particle size is less important than for example LDF or DLS, the low polydispersity of particles that is manifest from DLS data ensures that good phantom homogeneity in terms of optical properties is achievable by not allowing gradients of particle sizes to form due to sedimentation. It is also relatively easy to control temperature changes. Particles of a constant size that is comparable to the wavelength of light in the visible and NIR spectral ranges determine that an effective Mie scattering theory can fit the scattering coefficients allowing the μ_s' to be easy to predict outside at intermediate wavelengths between the measurement points.

The scattering particles provided by Hemophotonics have been found to be suitable for building a stable synthetic liquid phantom for DCS. They clearly exhibit a Brownian diffusive behavior when diluted in water (D_B RE$\sim$5%). Water based phantoms are easier to contain and in this case this was achieved without effects of water evaporation to be visible. A recipe that relates the particle concentration in water with the reduced scattering coefficient was obtained using precise TRS characterization. Pigments and dyes like india ink or Nigrosin can be added and optical properties similar to tissues [201] can be obtained.

The stability of the measured D_B was investigated in two separate longitudinal run experiment, with (11 weeks) and without (20 weeks) monitoring of the optical properties. Similar variations of the D_B values in the two cases suggest that optical properties changes (variations of 5% and 7% of μ_s' and μ_a were measured over 11 weeks in the first phantom) do not play a determinant role in the accuracy of the D_B and, therefore, of the BFi that can be rendered by the phantom. The source of day-to-day variations of D_B are more likely explained by the changes in the room temperature. This feature is trivially resolved by storing the phantom at a constant temperature when working in a controlled laboratory, as in the case of the longitudinal measurements carried out on the first phantom, but can be difficult to control in many settings like hospital rooms as in the case of the experiments with the second phantom reported.

Since D_B has been found to vary with respect to the phantom temperature as expected for a diluted collection of Brownian light scatterers, it is possible to use of this phenomenon is to induce a controlled perturbation in D_B that can in theory be used to test the dynamic scale of DCS instrument by carefully and continuously monitoring the temperature of the liquid during heating or during cooling. However, the change of BFi that can be achieved in this case is modest (14% over about 6 °C) and not comparable with a cuff occlusion experiment, which spans generally two order of magnitude variations in BFi. By carefully monitoring the temperature, however, it could also be possible to account for small variations of temperature between days and locations of measurements and further reduce the RE of the longitudinal measurements.

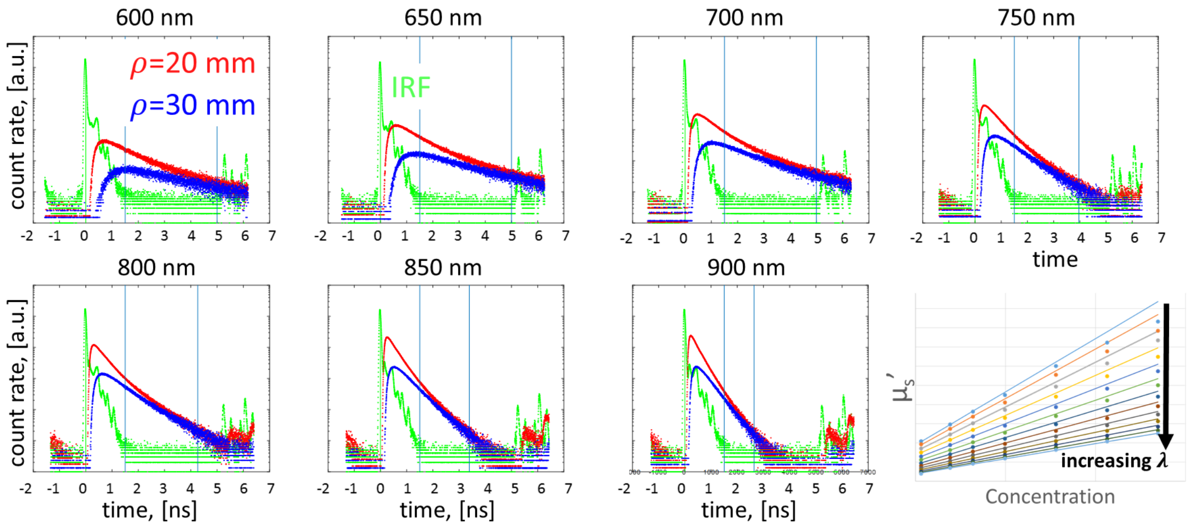

Figure 6.3: Sample distributions of times-of-flight and instrument response function for 2 source-detector separations (ρ=20 and 30 mm) and 7 wavelengths. The linear dependence of the retrieved μ_{s}' at different wavelengths (colors) on the scatterers concentration (x-axis) is also reported.

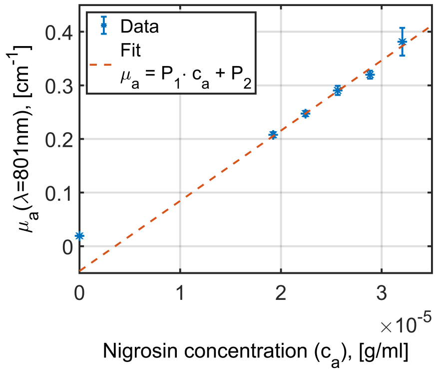

Figure 6.4: Fit of the absorption of dye in water with respect to its concentration (c_a).

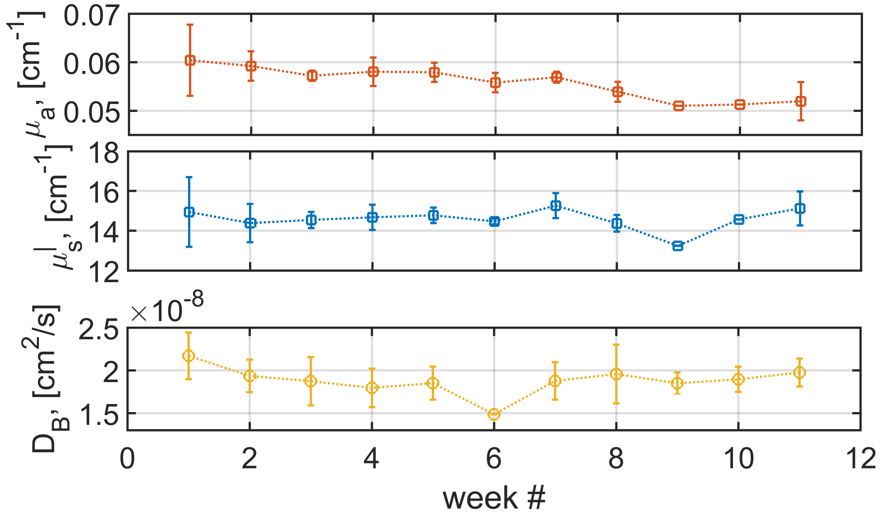

Figure 6.5: Weekly average of the optical properties and of the D_B over a 11 weeks interval.

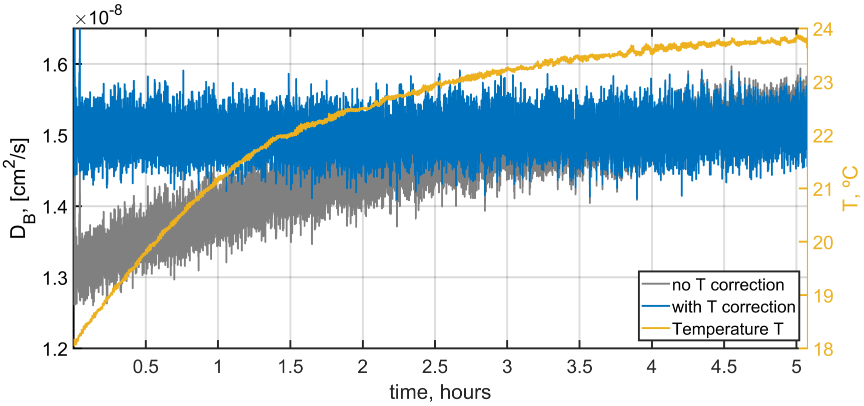

Figure 6.6: The fitted Brownian diffusion coefficient is reported (grey line) for a 5 hours DCS experiment during which the temperature increased (ΔT=9.5 °C) from refrigerated to ambient temperature. Temperature from a thermocouple inserted in the liquid (yellow line) was used to correct for the Brownian diffusion coefficient, yielding the correct stable D_B expected at 300 K (blue line).

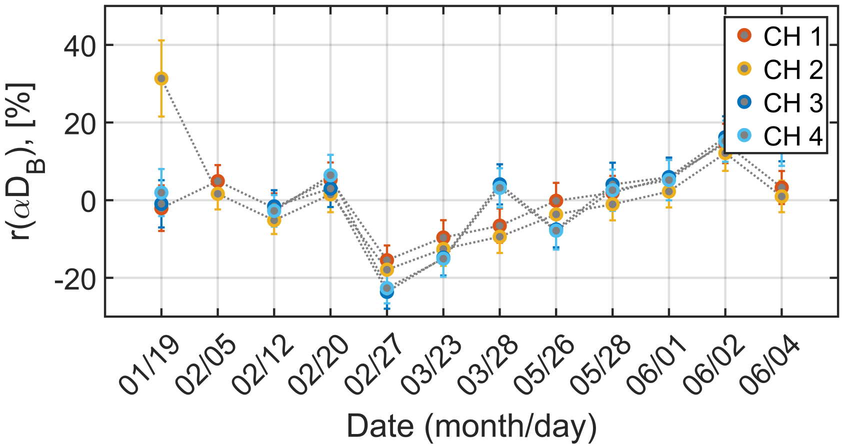

Figure 6.7: Relative changes with respect to the mean of the D_B estimated from the longitudinal phantom during 136 days (20 weeks). Temperature of the room was not controlled; day-by-day changes up to 6 °C were observed.

Chapter 7

Conclusions

This monograph has introduced and demonstrated a set of promising tools for the research and ultimately, for the clinical translation, for measuring the hemodynamic processes in the human body. These tools are based on non-invasive diffuse optical and correlation spectroscopies. This work has expanded cal mechanisms in the human body using endogenous markers like microvascular blood flow and oxygenation. At the same time, new experimental techniques were described, which can potentially improve the existing framework, especially for continuous blood flow and metabolism monitoring, and also enable new applications, like the case of the optical measurements of the bone microvasculature.

To this extent, in chapter 3, I have described how I have contributed to the improvement of the state-of-the-art of the relative new TD-DCS technique. My contribution to this field were the first *in vivo* measurements in humans [86], and the first measurements at very short, practically null, source-detector separation [87]. The introduction of the concept of TD-SCOS has considerable potential to reduce the cost and complexity, making a complete, continuous and non invasive diffuse optical characterization of tissue in terms of tissue components concentrations and dynamics more accessible to the experimenter.

Time domain DCS can be useful in a wide range of applications where DCS and TRS are used; examples are the study of cerebral autoregulation [202], reducing partial volume from superficial head tissue when monitoring the effects of transcranial direct current stimulation [203], and more in general all the studies that benefit from a selective measure of BFi from a depth of the tissue with a single pair of optodes. Among the possible upgrades of this technique, multi-distance DCS has been already demonstrated to achieve optical properties estimation [204] and can in theory be applied to TD-DCS also to offer further constraints to the reconstruction of BFi and optical properties. More interestingly, multiple wavelengths may offer accurate fits of the BFi and hemoglobin concentration simultaneously as in TRS [15].

When defining the wavelengths of interest for a multi-wavelength approach, it is of interest to include the longer wavelength part of the spectrum (i.e. $>$1000 nm). Among The benefits of operating at wavelength above this value: skin safety is guaranteed for higher power laser source at these wavelengths; photons are more numerous even at constant detection flux, determining higher signal is achievable in photon counting experiments; although absorption of water is higher, scattering quickly decays with wavelength determining an overall stable attenuation and penetration of light up to a certain point in tissue; scattering contribution from small centers decays faster, but the relative bigger red blood cells contribution mostly stays unaltered.

Recently, interferometric techniques have been developed and expaded in order to measure multiple independent speckles by using a CMOS cameras for multispeckle detection, with up to 20 speckles measured simultaneously [205]. Parallel detection with non-photon counting detectors, which is carried out already with up to million parallel detectors in SCOS [119], is acknowledged to be potentially disruptive. Although the inclusion of optical phase sensitivity can be beneficial, improvements in performances with respect to SCOS or TD-SCOS, the latter also using non-single-photon-counting cameras, are yet to be proven.

Regarding its applicability and capabilities, the presented time-domain methods will benefit from advancements in the laser and detector technologies. The production of turn-key, portable long-coherence, yet pulsed, lasers are technologically feasible [92]. We may have created the demand for them by introducing them to biomedical applications. The same can be said for photon-counting, fast and high quantum-efficiency detectors. Time will tell.

In this work, biological media of interest have been modeled as homogeneous. However, it would be interesting to extend the analysis method to layered devices using multiple gates and autocorrelation curves at different time bins. Similar analysis methods already exist for TRS [109, 62].

Signal-to-noise ratio has been extensively studied for hybrid TRS-DCS devices [206] but, up to this point, the same has not been carried out for TD-DCS or for TD-SCOS. Given the centrality of this issues, even with respect to comparing time domain and interferometric techniques, and especially for large area, non photon-counting detectors as in TD-SCOS, this will be the argument of further study, also aimed to study of the effect of the temporal coherence and pulse shape properties of laser source on the accuracy and precision of TD-DCS, a problem approached first by [111] and by our group [110]. While this can allow to optimize the selection of a compact off-the-shelf solution for TD-DCS, like for example in [92], this is better done having a versatile open system as the one described in 3.2.2.

Although it has been shown that TD-DCS is able to measure the deeper tissues, it is of interest to test also the advantages of concomitant accurate superficial tissue hemodynamics measurements. Algorithms for the regression of superficial spurious and systemic hemodynamic signals in functional studies have been proposed for example in fNIRS [207], but so far using multi-source-detector separation approach, and only in NIRS; in this case of TD-DCS would be beneficial because of the superficial and deep are sampled at the same time on much more similar volumes for functional BFi estimation.

In chapter 4, I have described my contribution to the field of functional studies with DCS, introducing, for the first time, fDCS measurements of neurovascular coupling in infants. From a point of view of brain physiology, some recent works [130] highlighted how the neurovascular coupling in young subjects is still poorly understood: blood flow measurements on awake subjects during neuronal activation can shed light on the phenomenon. Infants have in fact limited access to MRI, and DCS signal-to-noise ratio is improved in infants due to the relative lack of hair [208]. On the other side, as fNIRS contribution to the neuroimaging community is expected to increase in the coming years [209, 210], DCS, by offering complementary information, is aslo expected to become more widely used.

Chapter 5 described the application of hybrid broadband time domain NIRS/DOS and DCS, which nowadays is the cutting edge technology for diffuse optical devices used in the clinics, for the study of the bone tissue. Light can detect changes generated by bone-affecting disease, in particular HIV infection, in a complementary way to gold standard clinical standard procedures (DXA).

Bone vascular health assessment by optical methods is novel and generally reported in the literature as a series of proof-of-concept studies, as summed up recently in [42]. Interestingly, the cited review paper acknowledges the fact that the key for the improvement of the low reliability and reproducibility of these studies resides in the technological advances; on this side, hybrid broadband time domain NIRS/DOS and DCS used here, for depth of penetration and versatility, constitutes undoubtedly the cutting edge of the available optical technologies for bone investigation.

Lastly, chapter 6 encompassed years of research results on the engineering of measurement standards for DCS, a field that is still far from reach the consensus from the academic and industrial worlds. However, the proposed solution has shown to be more stable than any other solution reported in the literature for the continuous monitoring of the stability of DCS (months).

Flow phantoms for DCS have been reported, as in [211], but having a stable reference over time for the effective BFi was not yet achieved, although is required for many applications, i.e. testing the instrument's accuracy in a multi-center study. Controlled temperature changes in a modest temperature range of 10 °C can be used to test the dynamic accuracy of BFi measurements by DCS. This temperature range has been used because convenient: further studies shall be carried out to determine an optimal temperature range. The span of the dynamic changes achievable this way is not comparable with the span obtained during for example a arm cuff occlusion; however, carrying out measurements at different source-detector separation or with multiple phantoms in which μ_{s}' is varying, it is possible to probe different decay times. The ability of doing that on a calibration standard (i.e. a phantom) instead on a human (or animal) will get the rid of the physiological variability affecting the calibration measurements carried out on the latter.

Bibliography

[1] M. Cutler, “Transillumination as an aid in the diagnosis of breast lesions,” *Surgery, gynecology and obstetrics*, vol. 48, pp. 721—-729, 1929.

[2] E. Sickles, “Breast cancer detection with transillumination and mammography,” *American Journal of Roentgenology*, vol. 142, pp. 841–844, apr 1984.

[3] T. Barozzino and M. Sgro, “Transillumination of the neonatal skull: seeing the light,” *CMAJ: Canadian Medical Association Journal*, vol. 167, no. 11, pp. 1271–1272, 2002.

[4] A. Pifferi, D. Contini, A. D. Mora, A. Farina, L. Spinelli, and A. Torricelli, “New frontiers in time-domain diffuse optics, a review,” *Journal of Biomedical Optics*, vol. 21, p. 091310, jun 2016.

[5] T. Durduran, R. Choe, W. B. Baker, and A. G. Yodh, “Diffuse optics for tissue monitoring and tomography,” *Reports on Progress in Physics*, vol. 73, no. 7, 2010.

[6] D. A. Boas, L. E. Campbell, and A. G. Yodh, “Scattering and Imaging with Diffusing Temporal Field Correlations,” *Physical Review Letters*, vol. 75, pp. 1855–1858, aug 1995.

[7] T. Durduran and A. G. Yodh, "Diffuse correlation spectroscopy for non-invasive, micro-vascular cerebral blood flow measurement," *NeuroImage*, vol. 85, p. 51, 2014.

[8] A. G. Yodh and B. Chance, "Spectroscopy and imaging with diffusing light," *Physics Today*, vol. 48, pp. 34—-41, 1995.

[9] S. Andersson-Engels, O. Jarlman, R. Berg, and S. Svanberg, "Time-resolved transillumination for medical diagnostics," *Optics Letters*, vol. 15, p. 1179, nov 1990.

[10] J. M. Maarek, G. Jarry, J. Crowe, M. H. Bui, and D. Laurent, "Simulation of laser tomoscopy in a heterogeneous biological medium," *Medical and Biological Engineering and Computing*, vol. 24, no. July, pp. 407–414, 1986.

[11] M. Ferrari and V. Quaresima, "A brief review on the history of human functional near-infrared spectroscopy (fNIRS) development and fields of application," *NeuroImage*, vol. 63, no. 2, pp. 921–935, 2012.

[12] M. N. Kim, B. L. Edlow, T. Durduran, S. Frangos, R. C. Mesquita, J. M. Levine, J. H. Greenberg, A. G. Yodh, and J. A. Detre, "Continuous Optical Monitoring of Cerebral Hemodynamics During Head-of-Bed Manipulation in Brain-Injured Adults," *Neurocritical Care*, vol. 20, pp. 443–453, jun 2014.

[13] A. Pifferi, D. Contini, A. D. Mora, A. Farina, L. Spinelli, and A. Torricelli, "New frontiers in time-domain diffuse optics, a review," *Journal of Biomedical Optics*, vol. 21, p. 091310, jun 2016.

[14] R. C. Mesquita, T. Durduran, G. Yu, E. M. Buckley, M. N. Kim, C. Zhou, R. Choe, U. Sunar, and A. G. Yodh, "Direct measurement of tissue blood flow and metabolism with diffuse optics,"

Philosophical Transactions of the Royal Society A: Mathematical, Physical and Engineering Sciences, vol. 369, pp. 4390–4406, nov 2011.

[15] A. Torricelli, D. Contini, A. Pifferi, M. Caffini, R. Re, L. Zucchelli, and L. Spinelli, "Time domain functional NIRS imaging for human brain mapping," *NeuroImage*, vol. 85, pp. 28–50, jan 2014.

[16] F. Martelli, T. Binzoni, A. Pifferi, L. Spinelli, A. Farina, and A. Torricelli, "There's plenty of light at the bottom: statistics of photon penetration depth in random media," *Scientific Reports*, vol. 6, p. 27057, jul 2016.

[17] S. Konugolu Venkata Sekar, A. Dalla Mora, I. Bargigia, E. Martinenghi, C. Lindner, P. Farzam, M. Pagliazzi, T. Durduran, P. Taroni, A. Pifferi, and A. Farina, "Broadband (600–1350 nm) Time-Resolved Diffuse Optical Spectrometer for Clinical Use," *IEEE Journal of Selected Topics in Quantum Electronics*, vol. 22, pp. 406–414, may 2016.

[18] M. Giovannella, D. Contini, M. Pagliazzi, A. Pifferi, L. Spinelli, R. Erdmann, R. Donat, I. Rocchetti, M. Rehberger, N. Koenig, R. Schmitt, A. Torricelli, T. Durduran, and U. M. Weigel, "BabyLux device: a diffuse optical system integrating diffuse correlation spectroscopy (DCS) and time resolved near infra-red spectroscopy (TR-NIRS) for neuro-monitoring of the premature newborn brain," *Neurophotonics*, vol. submitted, 2019.

[19] C. Lindner, M. Mora, P. Farzam, M. Squarcia, J. Johansson, U. M. Weigel, I. Halperin, F. A. Hanzu, and T. Durduran, "Diffuse Optical Characterization of the Healthy Human Thyroid Tissue and Two Pathological Case Studies," *PLOS ONE*, vol. 11, p. e0147851, jan 2016.

[20] P. Farzam, C. Lindner, U. M. Weigel, M. Suarez, A. Urbano-Ispizua, and T. Durduran, “Noninvasive characterization of the healthy human manubrium using diffuse optical spectroscopies,” *Physiological Measurement*, vol. 35, pp. 1469–1491, jul 2014.

[21] J. Selb, D. A. Boas, S.-T. Chan, K. C. Evans, E. M. Buckley, and S. A. Carp, “Sensitivity of near-infrared spectroscopy and diffuse correlation spectroscopy to brain hemodynamics: simulations and experimental findings during hypercapnia,” *Neurophotonics*, vol. 1, p. 015005, aug 2014.

[22] P. Andersson, T. Andersson, and S. Eng, “Interpulse coherence of picosecond pulses from semiconductor lasers,” *IEEE Journal of Quantum Electronics*, vol. 21, pp. 582–586, jun 1985.

[23] P. Andersson, T. Andersson, S. Lundqvist, and S. Eng, “Temporal coherence properties of picosecond pulses generated by GaAlAs semiconductor lasers for directly modulated and frequency stabilized optical communication systems,” *Journal of Lightwave Technology*, vol. 2, no. 2, pp. 146–154, 1984.

[24] N. Curry, P. Bondareff, M. Leclercq, N. F. van Hulst, R. Sapienza, S. Gigan, and S. Grésillon, “Direct determination of diffusion properties of random media from speckle contrast,” *Optics Letters*, vol. 36, p. 3332, sep 2011.

[25] L. Wen-Jun, G. Ren-Xi, and Q. Shi-Liang, “Measurements of femtosecond temporal speckle field of a random medium,” *Chinese Physics B*, vol. 19, p. 024204, feb 2010.

[26] T. Bellini, M. A. Glaser, N. A. Clark, and V. Degiorgio, “Effects of finite laser coherence in quasielastic multiple scattering,” *Physical Review A*, vol. 44, pp. 5215–5223, oct 1991.

[27] P. A. Lemieux and D. J. Durian, "Investigating non-Gaussian scattering processes by using nth -order intensity correlation functions," *Journal of the Optical Society of America A*, vol. 16, p. 1651, jul 1999.

[28] M. Tomita, K. Shimano, and K. Nakata, "Uncertainty relation in fluctuations in the space and time domains in disordered optical media," *Physical Review B*, vol. 54, pp. R3687–R3689, aug 1996.

[29] K. Shimano and M. Tomita, "Influence of the trajectory-distribution function on the temporal and spectral correlations in disordered media," *Physical Review B*, vol. 58, pp. 5160–5162, sep 1998.

[30] A. G. Yodh, P. D. Kaplan, and D. J. Pine, "Pulsed diffusing-wave spectroscopy: High resolution through nonlinear optical gating," *Physical Review B*, vol. 42, pp. 4744–4747, sep 1990.

[31] J. Sutin, B. Zimmerman, D. Tyulmankov, D. Tamborini, K. C. Wu, J. Selb, A. Gulinatti, I. Rech, A. Tosi, D. A. Boas, and M. A. Franceschini, "Time-domain diffuse correlation spectroscopy," *Optica*, vol. 3, p. 1006, sep 2016.

[32] A. A. Phillips, F. H. Chan, M. M. Z. Zheng, A. V. Krassioukov, and P. N. Ainslie, "Neurovascular coupling in humans: Physiology, methodological advances and clinical implications," *Journal of Cerebral Blood Flow & Metabolism*, vol. 36, pp. 647–664, apr 2016.

[33] S. M. Liao, N. M. Gregg, B. R. White, B. W. Zeff, K. A. Bjerkaas, T. E. Inder, and J. P. Culver, "Neonatal hemodynamic response to visual cortex activity: high-density near-infrared spectroscopy study," *Journal of Biomedical Optics*, vol. 15, no. 2, p. 026010, 2010.

[34] S. M. Liao, "High-density diffuse optical tomography of term infant visual cortex in the nursery," *Journal of Biomedical Optics*, vol. 17, p. 081414, jul 2012.

[35] T. Binzoni and D. Van De Ville, "Noninvasive probing of the neurovascular system in human bone/bone marrow using near-infrared light," *Journal of Innovative Optical Health Sciences*, vol. 4, no. 02, pp. 183–189, 2011.

[36] R. Choe and T. Durduran, "Diffuse optical monitoring of the neoadjuvant breast cancer therapy," *IEEE Journal of selected topics in quantum electronics*, vol. 18, no. 4, pp. 1367–1386, 2012.

[37] A. Pifferi, A. Torricelli, P. Taroni, A. Bassi, E. Chikoidze, E. Giambattistelli, and R. Cubeddu, "Optical biopsy of bone tissue: a step toward the diagnosis of bone pathologies," *Journal of Biomedical Optics*, vol. 9, no. 3, p. 474, 2004.

[38] P. Farzam, P. Zirak, T. Binzoni, and T. Durduran, "Pulsatile and steady-state hemodynamics of the human patella bone by diffuse optical spectroscopy," *Physiological Measurement*, vol. 34, pp. 839–857, aug 2013.

[39] S. Konugolu Venkata Sekar, M. Pagliazzi, E. Negredo, F. Martelli, A. Farina, A. Dalla Mora, C. Lindner, P. Farzam, N. Pérez-Álvarez, J. Puig, P. Taroni, A. Pifferi, and T. Durduran, "In Vivo, Non-Invasive Characterization of Human Bone by Hybrid Broadband (600-1200 nm) Diffuse Optical and Correlation Spectroscopies," *PLOS ONE*, vol. 11, p. e0168426, dec 2016.

[40] P. Taroni, G. Quarto, A. Pifferi, F. Abbate, N. Balestreri, S. Menna, E. Cassano, and R. Cubeddu, "Breast tissue compo-

sition and its dependence on demographic risk factors for breast cancer: non-invasive assessment by time domain diffuse optical spectroscopy," *PloS one*, vol. 10, no. 6, p. e0128941, 2015.

[41] C. Chung, Y.-P. Chen, T.-H. Leu, and C.-W. Sun, "Near-infrared bone densitometry: A feasibility study on distal radius measurement," *Journal of Biophotonics*, vol. 11, p. e201700342, jul 2018.

[42] R. Meertens, F. Casanova, K. M. Knapp, C. Thorn, and W. D. Strain, "Use of near-infrared systems for investigations of hemodynamics in human in vivo bone tissue: A systematic review," *Journal of Orthopaedic Research®*, vol. 36, pp. 2595–2603, oct 2018.

[43] S. Han, A. R. Proctor, J. B. Vella, D. S. W. Benoit, and R. Choe, "Non-invasive diffuse correlation tomography reveals spatial and temporal blood flow differences in murine bone grafting approaches," *Biomedical Optics Express*, vol. 7, p. 3262, sep 2016.

[44] S. Han, M. D. Hoffman, A. R. Proctor, J. B. Vella, E. A. Mannoh, N. E. Barber, H. J. Kim, K. W. Jung, D. S. W. Benoit, and R. Choe, "Non-Invasive Monitoring of Temporal and Spatial Blood Flow during Bone Graft Healing Using Diffuse Correlation Spectroscopy," *PLOS ONE*, vol. 10, p. e0143891, dec 2015.

[45] T. T. Brown and R. B. Qaqish, "Antiretroviral therapy and the prevalence of osteopenia and osteoporosis: a meta-analytic review," *Aids*, vol. 20, no. 17, pp. 2165–2174, 2006.

[46] A. Bonjoch, M. Figueras, C. Estany, N. Perez-Alvarez, J. Rosales, L. del Rio, S. di Gregorio, J. Puig, G. Gómez, B. Clotet, and Others, "High prevalence of and progression to low bone

mineral density in HIV-infected patients: a longitudinal cohort study," *Aids*, vol. 24, no. 18, pp. 2827–2833, 2010.

[47] G. V. Escota, K. Mondy, T. Bush, L. Conley, J. T. Brooks, N. Önen, P. Patel, E. M. Kojic, K. Henry, J. Hammer, and Others, "High prevalence of low bone mineral density and substantial bone loss over 4 years among HIV-infected persons in the era of modern antiretroviral therapy," *AIDS research and human retroviruses*, vol. 32, no. 1, pp. 59–67, 2016.

[48] V. A. Triant, T. T. Brown, H. Lee, and S. K. Grinspoon, "Fracture prevalence among human immunodeficiency virus (HIV)-infected versus non-HIV-infected patients in a large US healthcare system," *The Journal of Clinical Endocrinology & Metabolism*, vol. 93, no. 9, pp. 3499–3504, 2008.

[49] R. Güerri-Fernandez, P. Vestergaard, C. Carbonell, H. Knobel, F. F. Avilés, A. S. Castro, X. Nogués, D. Prieto-Alhambra, and A. Diez-Perez, "HIV infection is strongly associated with hip fracture risk, independently of age, gender, and comorbidities: A population-based cohort study," *Journal of Bone and Mineral Research*, vol. 28, no. 6, pp. 1259–1263, 2013.

[50] L. Spinelli, M. Botwicz, N. Zolek, M. Kacprzak, D. Milej, P. Sawosz, A. Liebert, U. Weigel, T. Durduran, F. Foschum, A. Kienle, F. Baribeau, S. Leclair, J.-P. Bouchard, I. Noiseux, P. Gallant, O. Mermut, A. Farina, A. Pifferi, A. Torricelli, R. Cubeddu, H.-C. Ho, M. Mazurenka, H. Wabnitz, K. Klauenberg, O. Bodnar, C. Elster, M. Bénazech-Lavoué, Y. Bérubé-Lauzière, F. Lesage, D. Khoptyar, A. A. Subash, S. Andersson-Engels, P. Di Ninni, F. Martelli, and G. Zaccanti, "Determination of reference values for optical properties of liquid phantoms

based on Intralipid and India ink," *Biomedical Optics Express*, vol. 5, p. 2037, jul 2014.

[51] J. R. Mourant, T. Fuselier, J. Boyer, T. M. Johnson, and I. J. Bigio, "Predictions and measurements of scattering and absorption over broad wavelength ranges in tissue phantoms," *Applied Optics*, vol. 36, p. 949, feb 1997.

[52] V. Ntziachristos, "Going deeper than microscopy: The optical imaging frontier in biology," *Nature Methods*, vol. 7, no. 8, pp. 603–614, 2010.

[53] S. L. Jacques, "Optical properties of biological tissues: a review," *Physics in Medicine & Biology*, vol. 58, no. 11, p. R37, 2013.

[54] S. Prahl, "Assorted Spectra."
`https://omlc.org/spectra/`.

[55] Y. Yamashita, A. Maki, and H. Koizumi, "Wavelength dependence of the precision of noninvasive optical measurement of oxy-, deoxy-, and total-hemoglobin concentration," *Medical Physics*, vol. 28, pp. 1108–1114, jun 2001.

[56] G. Strangman, M. A. Franceschini, and D. A. Boas, "Factors affecting the accuracy of near-infrared spectroscopy concentration calculations for focal changes in oxygenation parameters," *NeuroImage*, vol. 18, pp. 865–879, apr 2003.

[57] D. A. Boas, A. M. Dale, and M. A. Franceschini, "Diffuse optical imaging of brain activation: approaches to optimizing image sensitivity, resolution, and accuracy," *NeuroImage*, vol. 23, pp. S275–S288, jan 2004.

[58] A. Torricelli, A. Pifferi, P. Taroni, E. Giambattistelli, and R. Cubeddu, "In vivo optical characterization of human tissues from 610 to 1010 nm by time-resolved reflectance spectroscopy," *Physics in Medicine and Biology*, vol. 46, pp. 2227–2237, aug 2001.

[59] S. Suzuki, S. Takasaki, T. Ozaki, and Y. Kobayashi, "A Tissue oxygenation monitor using NIR spatially resolved spectroscopy," *Proc. SPIE*, vol. 3597, no. January 1999, pp. 582–592, 1999.

[60] G. Greisen, B. Andresen, A. M. Plomgaard, and S. Hyttel-Sørensen, "Cerebral oximetry in preterm infants: an agenda for research with a clear clinical goal," *Neurophotonics*, vol. 3, p. 031407, apr 2016.

[61] J. Steinbrink, H. Wabnitz, H. Obrig, A. Villringer, and H. Rinneberg, "Determining changes in NIR absorption using a layered model of the human head," *Physics in Medicine and Biology*, vol. 46, pp. 879–896, mar 2001.

[62] L. Spinelli, L. Zucchelli, D. Contini, M. Caffini, J. Mehler, A. Fló, A. L. Ferry, L. Filippin, F. Macagno, L. Cattarossi, and A. Torricelli, "In vivo measure of neonate brain optical properties and hemodynamic parameters by time-domain near-infrared spectroscopy," *Neurophotonics*, vol. 4, p. 1, aug 2017.

[63] I. Tachtsidis and F. Scholkmann, "False positives and false negatives in functional near-infrared spectroscopy: issues, challenges, and the way forward," *Neurophotonics*, vol. 3, p. 031405, mar 2016.

[64] A. Ishimaru, "Diffusion of a pulse in densely distributed scatterers," *JOSA*, vol. 68, no. 8, pp. 1045–1050, 1978.

[65] J. Ripoll, “Principles of diffuse light propagation: light propagation in tissues with applications in biology and medicine,” *Contemporary Physics*, apr 2012.

[66] R. K. Wang and Y. A. Wickramasinghe, “Fast algorithm to determine optical properties of a turbid medium from time-resolved measurements,” *Applied Optics*, vol. 37, p. 7342, nov 1998.

[67] R. C. Haskell, L. O. Svaasand, T.-T. Tsay, T.-C. Feng, B. J. Tromberg, and M. S. McAdams, “Boundary conditions for the diffusion equation in radiative transfer,” *Journal of the Optical Society of America A*, vol. 11, p. 2727, oct 1994.

[68] D. Contini, F. Martelli, and G. Zaccanti, “Photon migration through a turbid slab described by a model based on diffusion approximation I Theory,” *Applied Optics*, vol. 36, p. 4587, jul 1997.

[69] M. S. Patterson, B. Chance, and B. C. Wilson, “Time resolved reflectance and transmittance for the noninvasive measurement of tissue optical properties,” *Applied Optics*, vol. 28, p. 2331, jun 1989.

[70] W. Becker, *The bh TCSPC Handbook*. Berlin: Becker & Hickl GmbH, 7th ed., 2017.

[71] L. Spinelli, F. Martelli, A. Farina, A. Pifferi, A. Torricelli, R. Cubeddu, and G. Zaccanti, “Calibration of scattering and absorption properties of a liquid diffusive medium at NIR wavelengths. Time-resolved method,” *Optics Express*, vol. 15, no. 11, p. 6589, 2007.

[72] S. Del Bianco, F. Martelli, and G. Zaccanti, "Penetration depth of light re-emitted by a diffusive medium: theoretical and experimental investigation," *Physics in Medicine and Biology*, vol. 47, pp. 4131–4144, dec 2002.

[73] G. Yu, T. Durduran, G. Lech, C. Zhou, B. Chance, E. R. Mohler, and A. G. Yodh, "Time-dependent blood flow and oxygenation in human skeletal muscles measured with noninvasive near-infrared diffuse optical spectroscopies," *Journal of Biomedical Optics*, vol. 10, no. 2, p. 024027, 2005.

[74] A. Torricelli, A. Pifferi, L. Spinelli, R. Cubeddu, F. Martelli, S. Del Bianco, and G. Zaccanti, "Time-Resolved Reflectance at Null Source-Detector Separation: Improving Contrast and Resolution in Diffuse Optical Imaging," *Physical Review Letters*, vol. 95, p. 078101, aug 2005.

[75] A. Pifferi, A. Torricelli, L. Spinelli, D. Contini, R. Cubeddu, F. Martelli, G. Zaccanti, A. Tosi, A. Dalla Mora, F. Zappa, and S. Cova, "Time-Resolved Diffuse Reflectance Using Small Source-Detector Separation and Fast Single-Photon Gating," *Physical Review Letters*, vol. 100, p. 138101, mar 2008.

[76] B. J. Berne and R. Pecora, *Dynamic Light scattering with applications to chemistry, biology, and physics.* New York: John Wiley & sons, Inc., 1990.

[77] G. Maret and P. E. Wolf, "Multiple light scattering from disordered media. The effect of brownian motion of scatterers," *Zeitschrift fur Physik B Condensed Matter*, vol. 65, pp. 409–413, dec 1987.

[78] D. J. Pine, D. A. Weitz, P. M. Chaikin, and E. Herbolzheimer, "Diffusing wave spectroscopy," *Physical Review Letters*, vol. 60, pp. 1134–1137, mar 1988.

[79] D. J. Pine, D. Weitz, J. Zhu, and E. Herbolzheimer, "Diffusing-wave spectroscopy: dynamic light scattering in the multiple scattering limit," *Journal de Physique*, vol. 51, no. 18, pp. 2101–2127, 1990.

[80] B. J. ACKERSON, R. L. DOUGHERTY, N. M. REGUIGUI, and U. NOBBMANN, "Correlation transfer - Application of radiative transfer solution methods to photon correlation problems," *Journal of Thermophysics and Heat Transfer*, vol. 6, pp. 577–588, oct 1992.

[81] S. Sakadžic, D. A. Boas, and S. A. Carp, "Theoretical model of blood flow measurement by diffuse correlation spectroscopy," *Journal of Biomedical Optics*, vol. 22, no. 2, p. 027006, 2017.

[82] T. Binzoni, B. Sanguinetti, D. Van de Ville, H. Zbinden, and F. Martelli, "Probability density function of the electric field in diffuse correlation spectroscopy of human bone in vivo," *Applied Optics*, vol. 55, p. 757, feb 2016.

[83] C. Zhou, *In-vivo optical imaging and spectroscopy of cerebral hemodynamics*. PhD thesis, UPenn, 2007.

[84] D. R. Busch, R. Balu, W. B. Baker, W. Guo, L. He, M. Diop, D. Milej, V. Kavuri, O. Amendolia, K. S. Lawrence, *et al.*, "Detection of brain hypoxia based on noninvasive optical monitoring of cerebral blood flow with diffuse correlation spectroscopy," *Neurocritical care*, vol. 30, no. 1, pp. 72–80, 2019.

[85] M. Diop, K. Verdecchia, T.-Y. Lee, and K. St Lawrence, “Calibration of diffuse correlation spectroscopy with a time-resolved near-infrared technique to yield absolute cerebral blood flow measurements,” *Biomedical optics express*, vol. 2, no. 7, pp. 2068–2081, 2011.

[86] M. Pagliazzi, S. Konugolu Venkata Sekar, L. Colombo, E. Martinenghi, J. Minnema, R. Erdmann, D. Contini, A. Dalla Mora, A. Torricelli, A. Pifferi, and T. Durduran, “Time domain diffuse correlation spectroscopy with a high coherence pulsed source: in vivo and phantom results,” *Biomedical Optics Express*, vol. 8, p. 5311, nov 2017.

[87] M. Pagliazzi, S. Konugolu Venkata Sekar, L. Di Sieno, L. Colombo, T. Durduran, D. Contini, A. Torricelli, A. Pifferi, and A. Dalla Mora, “In vivo time-gated diffuse correlation spectroscopy at quasi-null source-detector separation,” *Optics Letters*, vol. 43, p. 2450, jun 2018.

[88] L. Colombo, M. Pagliazzi, S. K. V. Sekar, D. Contini, A. D. Mora, L. Spinelli, A. Torricelli, T. Durduran, and A. Pifferi, “”effects of the instrument response function and the gate width in time-domain diffuse correlation spectroscopy: model and validations,” In press.

[89] M. Pagliazzi, E. Martinenghi, J. Minnema, R. Erdmann, K. Lauritsen, D. Contini, and A. D. Mora, “Compact Time Resolved Diffuse Correlation Spectroscopy Setup with Commercial Off-the-shelf (COTS) Components .,” in *paper presented to European conference of biomedical optics, 25–29 June 2017, Munich, Germany*, pp. 6–8, 2017.

[90] M. Pagliazzi, S. K. V. Sekar, L. Colombo, E. Martinenghi, J. Minnema, R. Erdmann, D. Contini, A. Dalla Mora, A. Torri-

celli, A. Pifferi, *et al.*, "In vivo, depth resolved measurement of blood flow with time domain diffuse correlation spectroscopy," in *Optical Tomography and Spectroscopy*, pp. OW2D–2, Optical Society of America, 2018.

[91] M. Pagliazzi, E. E. Vidal-Rosas, S. K. V. Sekar, L. D. Sieno, L. Colombo, D. Contini, A. Torricelli, A. Pifferi, A. D. Mora, J. P. Culver, and T. Durduran, "In vivo time domain speckle contrast optical spectroscopy," in *European Conferences on Biomedical Optics (ECBO) 2019*, vol. Oral presentation, (Munich, Germany), SPIE/OSA, 2019.

[92] D. Tamborini, K. Stephens, M. Wu, P. Farzam, A. Siegel, O. Shatrovoy, M. Blackwell, D. A. Boas, S. Carp, and M. A. Franceschini, "Portable system for Time-Domain Diffuse Correlation Spectroscopy," *IEEE Transactions on Biomedical Engineering*, vol. PP, no. c, pp. 1–1, 2019.

[93] J. M. Tualle, E. Tinet, and S. Avrillier, "New and easy way to perform time-resolved measurements of the light scattered by a turbid medium," *Optics Communications*, vol. 189, no. 4-6, pp. 211–220, 2001.

[94] J.-M. Tualle, C. Schäfauer, S. Avrillier, E. Tinet, H. L. Nghiêm, D. Ettori, and P. Berthaud, "Time-resolved measurements from speckle interferometry," *Optics Letters*, vol. 30, no. 1, p. 50, 2005.

[95] D. Borycki, O. Kholiqov, and V. J. Srinivasan, "Reflectance-mode interferometric near-infrared spectroscopy quantifies brain absorption, scattering, and blood flow index in vivo," *Optics Letters*, vol. 42, p. 591, feb 2017.

[96] Q. Zhao, L. Spinelli, A. Bassi, G. Valentini, D. Contini, A. Torricelli, R. Cubeddu, G. Zaccanti, F. Martelli, and A. Pifferi, "Functional tomography using a time-gated ICCD camera," *Biomedical Optics Express*, vol. 2, p. 705, mar 2011.

[97] A. Pifferi, *Sviluppo e caratterizzazione di un laser a titanio in zaffiro in regime continuo e di mode locking.* PhD thesis, Politecnico di Milano, 1990.

[98] A. Pifferi, A. Torricelli, P. Taroni, D. Comelli, A. Bassi, and R. Cubeddu, "Fully automated time domain spectrometer for the absorption and scattering characterization of diffusive media," *Review of Scientific Instruments*, vol. 78, p. 053103, may 2007.

[99] F. E. W. Schmidt, M. E. Fry, E. M. C. Hillman, J. C. Hebden, and D. T. Delpy, "A 32-channel time-resolved instrument for medical optical tomography," *Review of Scientific Instruments*, vol. 71, pp. 256–265, jan 2000.

[100] H. Wabnitz, D. R. Taubert, M. Mazurenka, O. Steinkellner, A. Jelzow, R. Macdonald, D. Milej, P. Sawosz, M. Kacprzak, A. Liebert, R. Cooper, J. Hebden, A. Pifferi, A. Farina, I. Bargigia, D. Contini, M. Caffini, L. Zucchelli, L. Spinelli, R. Cubeddu, and A. Torricelli, "Performance assessment of time-domain optical brain imagers, part 1: basic instrumental performance protocol," *Journal of Biomedical Optics*, vol. 19, p. 086010, aug 2014.

[101] P. D. Ninni, F. Martelli, and G. Zaccanti, "Intralipid: towards a diffusive reference standard for optical tissue phantoms," *Physics in Medicine and Biology*, vol. 56, pp. N21–N28, jan 2011.

[102] L. Cortese, G. L. Presti, M. Pagliazzi, D. Contini, A. D. Mora, A. Pifferi, S. K. V. Sekar, L. Spinelli, P. Taroni, M. Zanoletti, U. M. Weigel, S. de Fraguier, A. Nguyen-Dihn, B. Rosinski, and T. Durduran, "Liquid phantoms for near-infrared and diffuse correlation spectroscopies with tunable optical and dynamic properties," *Biomedical Optics Express*, vol. 9, p. 2068, may 2018.

[103] W. B. Baker, A. B. Parthasarathy, T. S. Ko, D. R. Busch, K. Abramson, S.-Y. Tzeng, R. C. Mesquita, T. Durduran, J. H. Greenberg, D. K. Kung, and A. G. Yodh, "Pressure modulation algorithm to separate cerebral hemodynamic signals from extracerebral artifacts," *Neurophotonics*, vol. 2, p. 035004, aug 2015.

[104] R. C. Mesquita, S. S. Schenkel, D. L. Minkoff, X. Lu, C. G. Favilla, P. M. Vora, D. R. Busch, M. Chandra, J. H. Greenberg, J. A. Detre, and A. G. Yodh, "Influence of probe pressure on the diffuse correlation spectroscopy blood flow signal: extra-cerebral contributions," *Biomedical Optics Express*, vol. 4, p. 978, jul 2013.

[105] D. Waithe, M. P. Clausen, E. Sezgin, and C. Eggeling, "FoCuS-point: software for STED fluorescence correlation and time-gated single photon counting," *Bioinformatics*, vol. 32, pp. 958–960, mar 2016.

[106] M. Wahl, I. Gregor, M. Patting, and J. Enderlein, "Fast calculation of fluorescence correlation data with asynchronous time-correlated single-photon counting," *Optics Express*, vol. 11, p. 3583, dec 2003.

[107] L. Dong, L. He, Y. Lin, Y. Shang, and G. Yu, "Simultaneously Extracting Multiple Parameters via Fitting One Single Auto-

correlation Function Curve in Diffuse Correlation Spectroscopy," *IEEE Transactions on Biomedical Engineering*, vol. 60, pp. 361–368, feb 2013.

[108] S. Prahl, "Light Absoprtion by water." `https://omlc.org/spectra/water/`.

[109] L. Spinelli, A. Pifferi, D. Contini, R. Cubeddu, and A. Torricelli, "Time-resolved optical stratigraphy in turbid media," in *Novel Optical Instrumentation for Biomedical Applications IV* (C. D. Depeursinge and I. A. Vitkin, eds.), vol. 7371, p. 73710A, jul 2009.

[110] L. Colombo, M. Pagliazzi, S. Konugolu Venkata Sekar, D. Contini, A. Dalla Mora, A. Torricelli, A. Pifferi, and T. Durduran, "Effects of Temporal Gating in Time Domain Diffuse Correlation Spectroscopy for Real Systems," in *Biophotonics Congress: Biomedical Optics Congress 2018 (Microscopy/Translational/Brain/OTS)*, no. 1, (Washington, D.C.), p. OTu2D.1, OSA, 2018.

[111] X. Cheng, D. Tamborini, S. A. Carp, O. Shatrovoy, B. Zimmerman, D. Tyulmankov, A. Siegel, M. Blackwell, M. A. Franceschini, and D. A. Boas, "Time domain diffuse correlation spectroscopy: modeling the effects of laser coherence length and instrument response function," *Optics Letters*, vol. 43, p. 2756, jun 2018.

[112] D. A. Boas and A. K. Dunn, "Laser speckle contrast imaging in biomedical optics," *Journal of Biomedical Optics*, vol. 15, no. 1, p. 011109, 2010.

[113] J. R. Goodwin, *Functional Near-Infrared Spectroscopy of the Adult and Infant Brain Queensland University of Technology*

Functional Near-Infrared Spectroscopy of the Adult and Infant Brain. PhD thesis, Queensland University of Technology, 2016.

[114] A. Puszka, L. Di Sieno, A. Dalla Mora, A. Pifferi, D. Contini, G. Boso, A. Tosi, L. Hervé, A. Planat-Chrétien, A. Koenig, and J.-M. Dinten, "Time-resolved diffuse optical tomography using fast-gated single-photon avalanche diodes," *Biomedical Optics Express*, vol. 4, p. 1351, aug 2013.

[115] E. Alerstam, T. Svensson, S. Andersson-Engels, L. Spinelli, D. Contini, A. D. Mora, A. Tosi, F. Zappa, and A. Pifferi, "Single-fiber diffuse optical time-of-flight spectroscopy," *Optics Letters*, vol. 37, p. 2877, jul 2012.

[116] S. Saha, F. Lesage, and M. Sawan, "Time-resolved reflectance using short source-detector separation," in *2016 IEEE International Symposium on Circuits and Systems (ISCAS)*, vol. 2016-July, pp. 333–336, IEEE, may 2016.

[117] L. Di Sieno, H. Wabnitz, A. Pifferi, M. Mazurenka, Y. Hoshi, A. Dalla Mora, D. Contini, G. Boso, W. Becker, F. Martelli, A. Tosi, and R. Macdonald, "Characterization of a time-resolved non-contact scanning diffuse optical imaging system exploiting fast-gated single-photon avalanche diode detection," *Review of Scientific Instruments*, vol. 87, p. 035118, mar 2016.

[118] L. Spinelli, F. Martelli, S. Del Bianco, A. Pifferi, A. Torricelli, R. Cubeddu, and G. Zaccanti, "Absorption and scattering perturbations in homogeneous and layered diffusive media probed by time-resolved reflectance at null source-detector separation," *Physical Review E*, vol. 74, p. 021919, aug 2006.

[119] C. P. Valdes, H. M. Varma, A. K. Kristoffersen, T. Dragojevic, J. P. Culver, and T. Durduran, "Speckle contrast optical spec-

troscopy, a non-invasive, diffuse optical method for measuring microvascular blood flow in tissue," *Biomedical Optics Express*, vol. 5, p. 2769, aug 2014.

[120] A. Fercher and J. Briers, "Flow visualization by means of single-exposure speckle photography," *Optics Communications*, vol. 37, pp. 326–330, jun 1981.

[121] T. Dragojević, J. L. Hollmann, D. Tamborini, D. Portaluppi, M. Buttafava, J. P. Culver, F. Villa, and T. Durduran, "Compact, multi-exposure speckle contrast optical spectroscopy (SCOS) device for measuring deep tissue blood flow," *Biomedical Optics Express*, vol. 9, p. 322, jan 2018.

[122] H. M. Varma, C. P. Valdes, A. K. Kristoffersen, J. P. Culver, and T. Durduran, "Speckle contrast optical tomography: A new method for deep tissue three-dimensional tomography of blood flow," *Biomedical Optics Express*, vol. 5, p. 1275, apr 2014.

[123] J. W. Goodman, "Statistical properties of laser sparkle patterns." 1963.

[124] R. Bandyopadhyay, A. S. Gittings, S. S. Suh, P. K. Dixon, and D. J. Durian, "Speckle-visibility spectroscopy: A tool to study time-varying dynamics," *Review of Scientific Instruments*, vol. 76, no. 9, 2005.

[125] J. C. Lagarias, J. A. Reeds, M. H. Wright, and P. E. Wright, "Convergence Properties of the Nelder–Mead Simplex Method in Low Dimensions," *SIAM Journal on Optimization*, vol. 9, pp. 112–147, jan 1998.

[126] D. Portaluppi, E. Conca, and F. Villa, "32 × 32 CMOS SPAD Imager for Gated Imaging, Photon Timing, and Photon Coinci-

dence," *IEEE Journal of Selected Topics in Quantum Electronics*, vol. 24, pp. 1–6, mar 2018.

[127] M. Pagliazzi, M. C. Canyelles, C. Santolin, N. S. Galles, and T. Durduran, "Regional changes in cerebral hemodynamics as a results of visual stimulation measured by diffuse correlation spectroscopy," in *5th biennial meeting of the Society of functional Near-Infrared Spectroscopy (SfNIRS)*, vol. Poster presentation, (Tokio, Japan), fNIRS society, 2018.

[128] K. Uludağ, D. J. Dubowitz, E. J. Yoder, K. Restom, T. T. Liu, and R. B. Buxton, "Coupling of cerebral blood flow and oxygen consumption during physiological activation and deactivation measured with fMRI," *NeuroImage*, vol. 23, pp. 148–155, sep 2004.

[129] F. Jaillon, J. Li, G. Dietsche, T. Elbert, and T. Gisler, "Activity of the human visual cortex measured non-invasively by diffusing-wave spectroscopy," *Optics Express*, vol. 15, no. 11, p. 6643, 2007.

[130] M. G. Kozberg, Y. Ma, S. H. Kim, M. A. Shaik, and E. M. C. Hillman, "Rapid Postnatal Expansion of Neural Networks Occurs in an Environment of Altered Neurovascular and Neurometabolic Coupling," *The Journal of Neuroscience*, vol. 36, no. 25, pp. 6704–6717, 2016.

[131] J. H. Meek, M. Firbank, C. E. Elwell, J. Atkinson, O. Braddick, and J. S. Wyatt, "Regional Hemodynamic Responses to Visual Stimulation in Awake Infants," *Pediatric Research*, vol. 43, pp. 840–843, jun 1998.

[132] G. Taga, K. Asakawa, A. Maki, Y. Konishi, and H. Koizumi, "Brain imaging in awake infants by near-infrared optical to-

pography," *Proceedings of the National Academy of Sciences*, vol. 100, pp. 10722–10727, sep 2003.

[133] S. Lloyd-Fox, R. Wu, J. E. Richards, C. E. Elwell, and M. H. Johnson, "Cortical Activation to Action Perception is Associated with Action Production Abilities in Young Infants," *Cerebral Cortex*, vol. 25, pp. 289–297, feb 2015.

[134] D. G. Pelli, "The VideoToolbox software for visual psychophysics: transforming numbers into movies," *Spatial Vision*, vol. 10, no. 4, pp. 437–442, 1997.

[135] D. H. Brainard, "The Psychophysics Toolbox," *Spatial Vision*, vol. 10, no. 4, pp. 433–436, 1997.

[136] M. Kleiner, D. H. Brainard, and D. G. Pelli, "What's new in Psychtoobox-3?," *Perception*, vol. 36, no. ECVP Abstract Supplement, p. 14, 2007.

[137] S. Lloyd-Fox, A. Blasi, and C. Elwell, "Illuminating the developing brain: The past, present and future of functional near infrared spectroscopy," *Neuroscience & Biobehavioral Reviews*, vol. 34, pp. 269–284, feb 2010.

[138] A. Cristia, E. Dupoux, Y. Hakuno, S. Lloyd-Fox, M. Schuetze, J. Kivits, T. Bergvelt, M. van Gelder, L. Filippin, S. Charron, and Y. Minagawa-Kawai, "An Online Database of Infant Functional Near InfraRed Spectroscopy Studies: A Community-Augmented Systematic Review," *PLoS ONE*, vol. 8, p. e58906, mar 2013.

[139] J. R. Goodwin, A. E. Cannaday, H. G. Palmeri, A. Di Costanzo, L. L. Emberson, R. N. Aslin, and A. J. Berger, "Methodology for high-yield acquisition of functional near-infrared spec-

troscopy data from alert, upright infants," *Neurophotonics*, vol. 3, p. 031415, jul 2016.

[140] N. Tottenham, J. W. Tanaka, A. C. Leon, T. McCarry, M. Nurse, T. A. Hare, D. J. Marcus, A. Westerlund, B. Casey, and C. Nelson, "The NimStim set of facial expressions: Judgments from untrained research participants," *Psychiatry Research*, vol. 168, pp. 242–249, aug 2009.

[141] N. Roche-Labarbe, A. Fenoglio, H. Radhakrishnan, M. Kocienski-Filip, S. A. Carp, J. Dubb, D. A. Boas, P. E. Grant, and M. A. Franceschini, "Somatosensory evoked changes in cerebral oxygen consumption measured non-invasively in premature neonates," *NeuroImage*, vol. 85, pp. 279–286, jan 2014.

[142] T. Durduran, R. Choe, W. B. Baker, and A. G. Yodh, "Diffuse optics for tissue monitoring and tomography," *Reports on Progress in Physics*, vol. 73, no. 7, 2010.

[143] M. Pagliazzi, M. Colomer Canyelles, C. Santolin, N. Sebastian Galles, and T. Durduran, "Regional Changes in Cerebral Hemodynamics as a Results of Visual Stimulation Measured by Diffuse Correlation Spectroscopy," in *fNIRS2018III-57* (FNIRS, ed.), (Tokio), p. 287, 2018.

[144] A. Born, E. Rostrup, M. Miranda, H. Larsson, and H. Lou, "Visual cortex reactivity in sedated children examined with perfusion MRI (FAIR)," *Magnetic Resonance Imaging*, vol. 20, pp. 199–205, feb 2002.

[145] UNAIDS, "2017 Global hiv statistics." `http://www.unaids.org/sites/default/files/media{_}asset/UNAIDS{_}FactSheet{_}en.pdf`, 2018.

[146] UNAIDS, "The GAP report 2014." `http://www.unaids.org/sites/default/files/media{_}asset/01{_}PeoplelivingwithHIV.pdf`, 2014.

[147] L. Battalora, K. Buchacz, C. Armon, E. T. Overton, J. Hammer, P. Patel, J. S. Chmiel, K. Wood, T. J. Bush, J. R. Spear, and Others, "Low bone mineral density and risk of incident fracture in HIV-infected adults," *Antivir Ther*, vol. 21, no. 1, pp. 45–54, 2016.

[148] T. T. Brown, G. A. McComsey, M. S. King, R. B. Qaqish, B. M. Bernstein, and B. A. Da Silva, "Loss of bone mineral density after antiretroviral therapy initiation, independent of antiretroviral regimen," *JAIDS Journal of Acquired Immune Deficiency Syndromes*, vol. 51, no. 5, pp. 554–561, 2009.

[149] G. A. McComsey, D. Kitch, E. S. Daar, C. Tierney, N. C. Jahed, P. Tebas, L. Myers, K. Melbourne, B. Ha, and P. E. Sax, "Bone mineral density and fractures in antiretroviral-naive persons randomized to receive abacavir-lamivudine or tenofovir disoproxil fumarate-emtricitabine along with efavirenz or atazanavir-ritonavir: Aids Clinical Trials Group A5224s, a substudy of ACTG," *Journal of Infectious Diseases*, vol. 203, no. 12, pp. 1791–1801, 2011.

[150] I. Cassetti, J. V. R. Madruga, J. M. A. H. Suleiman, A. Etzel, L. Zhong, A. K. Cheng, J. Enejosa, and S. E. Team, "The safety and efficacy of tenofovir df in combination with lamivudine and efavirenz through 6 years in antiretroviral-na{\"\i}ve HIV-1—infected patients," *HIV clinical trials*, vol. 8, no. 3, pp. 164–172, 2007.

[151] T. T. Brown, C. Moser, J. S. Currier, H. J. Ribaudo, J. Rothenberg, T. Kelesidis, O. Yang, M. P. Dubé, R. L. Murphy, J. H.

Stein, and Others, “Changes in bone mineral density after initiation of antiretroviral treatment with tenofovir disoproxil fumarate/emtricitabine plus atazanavir/ritonavir, darunavir/ritonavir, or raltegravir,” *The Journal of infectious diseases*, vol. 212, no. 8, pp. 1241–1249, 2015.

[152] E. Negredo, P. Domingo, N. Pérez-Álvarez, M. Gutiérrez, G. Mateo, J. Puig, R. Escrig, P. Echeverría, A. Bonjoch, and B. Clotet, “Improvement in bone mineral density after switching from tenofovir to abacavir in HIV-1-infected patients with low bone mineral density: two-centre randomized pilot study (OsteoTDF study),” *Journal of Antimicrobial Chemotherapy*, vol. 69, no. 12, pp. 3368–3371, 2014.

[153] P. M. Grant, D. Kitch, G. A. McComsey, A. C. Collier, S. L. Koletar, K. M. Erlandson, M. T. Yin, B. Bartali, B. Ha, K. Melbourne, and Others, “Long-term bone mineral density changes in antiretroviral-treated HIV-infected individuals,” *The Journal of infectious diseases*, vol. 214, no. 4, pp. 607–611, 2016.

[154] F. Gutiérrez and M. Masiá, “The role of HIV and antiretroviral therapy in bone disease.,” *AIDS reviews*, vol. 13, no. 2, pp. 109–118, 2011.

[155] I. Ofotokun, E. McIntosh, and M. N. Weitzmann, “HIV: inflammation and bone,” *Current HIV/AIDS Reports*, vol. 9, no. 1, pp. 16–25, 2012.

[156] K. M. Erlandson, M. O’Riordan, D. Labbato, and G. A. McComsey, “Relationships between inflammation, immune activation and bone health among HIV-infected adults on stable antiretroviral therapy,” *Journal of acquired immune deficiency syndromes (1999)*, vol. 65, no. 3, p. 290, 2014.

[157] E. Seeman and P. D. Delmas, “Bone quality—the material and structural basis of bone strength and fragility,” *New England Journal of Medicine*, vol. 354, no. 21, pp. 2250–2261, 2006.

[158] R. Burkhardt, G. Kettner, W. Böhm, M. Schmidmeier, R. Schlag, B. Frisch, B. Mallmann, W. Eisenmenger, and T. H. Gilg, “Changes in trabecular bone, hematopoiesis and bone marrow vessels in aplastic anemia, primary osteoporosis, and old age: a comparative histomorphometric study,” *Bone*, vol. 8, no. 3, pp. 157–164, 1987.

[159] L. Gazzola, A. Savoldi, F. Bai, A. Magenta, M. Dziubak, L. Pietrogrande, L. Tagliabue, A. Del Sole, T. Bini, G. Marchetti, and Others, “Assessment of radiological vertebral fractures in HIV-infected patients: clinical implications and predictive factors,” *HIV medicine*, vol. 16, no. 9, pp. 563–571, 2015.

[160] Y.-X. J. Wang, J. F. Griffith, A. W. L. Kwok, J. C. S. Leung, D. K. W. Yeung, A. T. Ahuja, and P. C. Leung, “Reduced bone perfusion in proximal femur of subjects with decreased bone mineral density preferentially affects the femoral neck,” *Bone*, vol. 45, no. 4, pp. 711–715, 2009.

[161] R. E. Tomlinson and M. J. Silva, “Skeletal blood flow in bone repair and maintenance,” *Bone research*, vol. 1, no. 4, p. 311, 2013.

[162] I. McCarthy, “The physiology of bone blood flow: a review,” *JBJS*, vol. 88, no. suppl_3, pp. 4–9, 2006.

[163] U. Saran, S. G. Piperni, and S. Chatterjee, “Role of angiogenesis in bone repair,” *Archives of biochemistry and biophysics*, vol. 561, pp. 109–117, 2014.

[164] J. F. Griffith, D. K. W. Yeung, G. E. Antonio, F. K. H. Lee, A. W. L. Hong, S. Y. S. Wong, E. M. C. Lau, and P. C. Leung, "Vertebral bone mineral density, marrow perfusion, and fat content in healthy men and men with osteoporosis: dynamic contrast-enhanced MR imaging and MR spectroscopy," *Radiology*, vol. 236, no. 3, pp. 945–951, 2005.

[165] L. Ou-Yang and G.-m. Lu, "Dysfunctional microcirculation of the lumbar vertebral marrow prior to the bone loss and intervertebral discal degeneration," *Spine*, vol. 40, no. 10, p. E593, 2015.

[166] D. A. Boas and A. G. Yodh, "Spatially varying dynamical properties of turbid media probed with diffusing temporal light correlation," *Journal of the Optical Society of America A*, vol. 14, p. 192, jan 1997.

[167] R Core Team, *R: A Language and Environment for Statistical Computing*. Vienna, Austria: R Foundation for Statistical Computing, 2018.

[168] M. Maechler, P. Rouss, A. Struyf, M. Hubert, and K. Hornik, "cluster: Cluster Analysis Basics and Extensions," 2018.

[169] T. Kubo, K. Kimori, F. Nakamura, S. Inoue, M. Fujioka, K. Ueshima, Y. Hirasawa, Y. Ushijima, and T. Nishimura, "Blood flow and blood volume in the femoral head of healthy adults according to age: Measurement with positron emission tomography (PET)," *Annals of nuclear medicine*, vol. 15, no. 3, pp. 231–235, 2001.

[170] A. P. Kusumbe, S. K. Ramasamy, and R. H. Adams, "Coupling of angiogenesis and osteogenesis by a specific vessel subtype in bone," *Nature*, vol. 507, no. 7492, pp. 323–328, 2014.

[171] M. Saito, “Poor bone quality in diabetes: detrimental collagen cross-link pattern reduces bone strength without change in bone mineral density,” *Clinical calcium*, vol. 16, no. 8, pp. 1287–1295, 2006.

[172] M. Saito and K. Marumo, “Collagen cross-links as a determinant of bone quality: a possible explanation for bone fragility in aging, osteoporosis, and diabetes mellitus,” *Osteoporosis international*, vol. 21, no. 2, pp. 195–214, 2010.

[173] P. K. K. Wong, J. J. Christie, and J. D. Wark, “The effects of smoking on bone health,” *Clinical Science*, vol. 113, pp. 233–241, sep 2007.

[174] S. Stegen and G. Carmeliet, “The skeletal vascular system – Breathing life into bone tissue,” *Bone*, vol. 115, pp. 50–58, oct 2018.

[175] M. Pagliazzi, M. Giovannella, U. M. Weigel, A. Pifferi, A. Torricelli, and T. Durduran, “Long-lasting, liquid phantom for diffuse optical and correlation spectroscopies,” in *Biomedical Optics 2016*, (Washington, D.C.), p. JTu3A.25, OSA, 2016.

[176] “What are imaging phantoms?.” `https://www.nist.gov/topics/physics/what-are-imaging-phantoms`.

[177] J. Hwang, J. C. Ramella-Roman, and R. Nordstrom, “Introduction: Feature Issue on Phantoms for the Performance Evaluation and Validation of Optical Medical Imaging Devices,” *Biomedical Optics Express*, vol. 3, p. 1399, jun 2012.

[178] A. E. Cerussi, R. Warren, B. Hill, D. Roblyer, A. Leproux, A. F. Durkin, T. D. O’Sullivan, S. Keene, H. Haghany, T. Quang,

W. M. Mantulin, and B. J. Tromberg, "Tissue phantoms in multicenter clinical trials for diffuse optical technologies," *Biomedical Optics Express*, vol. 3, p. 966, may 2012.

[179] S. T. Flock, S. L. Jacques, B. C. Wilson, W. M. Star, and M. J. C. van Gemert, "Optical properties of intralipid: A phantom medium for light propagation studies," *Lasers in Surgery and Medicine*, vol. 12, no. 5, pp. 510–519, 1992.

[180] R. Cubeddu, A. Pifferi, P. Taroni, A. Torricelli, and G. Valentini, "A solid tissue phantom for photon migration studies," *Physics in Medicine and Biology*, vol. 42, pp. 1971–1979, oct 1997.

[181] F. Ayers, A. Grant, D. Kuo, D. J. Cuccia, and A. J. Durkin, "Fabrication and characterization of silicone-based tissue phantoms with tunable optical properties in the visible and near infrared domain," in *Design and Performance Validation of Phantoms Used in Conjunction with Optical Measurements of Tissue* (R. J. Nordstrom, ed.), vol. 6870, p. 687007, feb 2008.

[182] B. W. Pogue and M. S. Patterson, "Review of tissue simulating phantoms for optical spectroscopy, imaging and dosimetry," *Journal of Biomedical Optics*, vol. 11, no. 4, p. 041102, 2006.

[183] L. A. Dempsey, M. Persad, S. Powell, D. Chitnis, and J. C. Hebden, "Geometrically complex 3D-printed phantoms for diffuse optical imaging," *Biomedical Optics Express*, vol. 8, p. 1754, mar 2017.

[184] N. Bodenschatz, P. Krauter, F. Foschum, S. Nothelfer, A. Liemert, E. Simon, S. Kröner, and A. Kienle, "Surface layering properties of Intralipid phantoms," *Physics in Medicine and Biology*, vol. 60, pp. 1171–1183, feb 2015.

[185] H. Cai, S.-E. Larsson, and P. A. Oberg, "Single Fiber Laser-Doppler Flowmetry—Dependence on Wavelength and Tip Optics," *Journal of Biomedical Optics*, vol. 3, p. 334, jul 1998.

[186] V. Rajan, B. Varghese, T. G. van Leeuwen, and W. Steenbergen, "Review of methodological developments in laser Doppler flowmetry," *Lasers in Medical Science*, vol. 24, pp. 269–283, mar 2009.

[187] G. E. Nilsson, T. Tenland, and P. A. Oberg, "Evaluation of a Laser Doppler Flowmeter for Measurement of Tissue Blood Flow," *IEEE Transactions on Biomedical Engineering*, vol. BME-27, pp. 597–604, oct 1980.

[188] A. Obeid, "In vitro comparison of different signal processing algorithms used in laser Doppler flowmetry," *Medical and Biological Engineering and Computing*, vol. 31, no. January, pp. 43–52, 1993.

[189] H. Ahn, K. Johansson, O. Lundgren, and G. Nilsson, "In vivo evaluation of signal processors for laser Doppler tissue flowmeters," *Medical and Biological Engineering and Computing*, vol. 25, no. March, pp. 207–211, 1987.

[190] A. V. Dunaev, E. A. Zherebtsov, D. A. Rogatkin, N. A. Stewart, S. G. Sokolovski, and E. U. Rafailov, "Novel measure for the calibration of laser Doppler flowmetry devices," in *Design and Quality for Biomedical Technologies VII* (R. Raghavachari, R. Liang, and T. J. Pfefer, eds.), vol. 8936, p. 89360D, mar 2014.

[191] W. Steenbergen and F. F. M. de Mul, "Application of a novel laser Doppler tester including a sustainable tissue phantom," in *SPIE Proc.* (A. V. Priezzhev, T. Asakura, and J. D. Briers, eds.), vol. 3252, pp. 14–25, jun 1998.

[192] A. Liebert, M. Leahy, and R. Maniewski, "A calibration standard for laser-Doppler perfusion measurements," *Review of Scientific Instruments*, vol. 66, pp. 5169–5173, nov 1995.

[193] D. Passos, J. C. Hebden, P. N. Pinto, and R. Guerra, "Tissue phantom for optical diagnostics based on a suspension of microspheres with a fractal size distribution," *Journal of Biomedical Optics*, vol. 10, no. 6, p. 064036, 2005.

[194] J. C. Hebden, B. D. Price, A. P. Gibson, and G. Royle, "A soft deformable tissue-equivalent phantom for diffuse optical tomography," *Physics in Medicine and Biology*, vol. 51, pp. 5581–5590, nov 2006.

[195] I. Fredriksson, M. Larsson, F. Salomonsson, and T. Strömberg, "Improved calibration procedure for laser Doppler perfusion monitors," in *Optical Diagnostics and Sensing XI: Toward Point-of-Care Diagnostics; and Design and Performance Validation of Phantoms Used in Conjunction with Optical Measurement of Tissue III* (R. J. Nordstrom and G. L. Coté, eds.), vol. 7906, p. 790602, feb 2011.

[196] D. J. Cuccia, "Determination of optical properties of turbid media spanning visible and near-infrared regimes via spatially modulated quantitative spectroscopy," *Journal of Biomedical Optics*, vol. 15, p. 017012, jan 2010.

[197] A. Farina, A. Torricelli, I. Bargigia, L. Spinelli, R. Cubeddu, F. Foschum, M. Jäger, E. Simon, O. Fugger, A. Kienle, F. Martelli, P. Di Ninni, G. Zaccanti, D. Milej, P. Sawosz, M. Kacprzak, A. Liebert, and A. Pifferi, "In-vivo multilaboratory investigation of the optical properties of the human head," *Biomedical Optics Express*, vol. 6, p. 2609, jul 2015.

[198] M. I. Limited, "Dynamic light scattering common terms defined." http://www.biophysics.bioc.cam.ac.uk/wp-content/uploads/2011/02/DLS_Terms_defined_Malvern.pdf, 2011.

[199] "Release on the IAPWS Formulation 2008 for the Viscosity of Ordinary Water Substance." `http://www.iapws.org/relguide/viscosity.html`, 2008.

[200] L. D. Landau and E. Lifshitz, *Theoretical Physics, vol. 6, Fluid Mechanics.* London: Pergamon, 1987.

[201] S. L. Jacques, "Optical properties of biological tissues: a review," *Physics in Medicine and Biology*, vol. 58, pp. R37–R61, jun 2013.

[202] J. Selb, K.-C. Wu, J. Sutin, P.-Y. I. Lin, P. Farzam, S. Bechek, and A. Shenoy, "Prolonged monitoring of cerebral blood flow and autoregulation with diffuse correlation spectroscopy in neurocritical care patients," *Neurophotonics*, vol. 5, p. 1, nov 2018.

[203] M. Giovannella, D. Ibañez, C. Gregori-Pla, and M. Kacprzak, "Concurrent measurement of cerebral hemodynamics and electroencephalography during transcranial direct current stimulation," *Neurophotonics*, vol. 5, p. 1, jan 2018.

[204] P. Farzam and T. Durduran, "Multidistance diffuse correlation spectroscopy for simultaneous estimation of blood flow index and optical properties," *Journal of Biomedical Optics*, vol. 20, p. 055001, may 2015.

[205] W. Zhou, O. Kholiqov, S. P. Chong, and V. J. Srinivasan, "Highly parallel, interferometric diffusing wave spectroscopy for

monitoring cerebral blood flow dynamics," *Optica*, vol. 5, p. 518, may 2018.

[206] M. Giovannella, L. Spinelli, M. Pagliazzi, D. Contini, G. Greisen, U. M. Weigel, A. Torricelli, and T. Durduran, "Accuracy and precision of tissue optical properties and haemodynamic parameters estimated by the BabyLux device: a hybrid time-resolved near-infrared and diffuse correlation spectroscopy neuro-monitor," *Biomedical Optics Express.*

[207] L. Gagnon, M. A. Yücel, D. A. Boas, and R. J. Cooper, "Further improvement in reducing superficial contamination in NIRS using double short separation measurements," *NeuroImage*, vol. 85, pp. 127–135, jan 2014.

[208] E. M. Buckley, A. B. Parthasarathy, P. E. Grant, A. G. Yodh, and M. A. Franceschini, "Diffuse correlation spectroscopy for measurement of cerebral blood flow: future prospects," *Neurophotonics*, vol. 1, p. 011009, jun 2014.

[209] P. Pinti, I. Tachtsidis, A. Hamilton, J. Hirsch, C. Aichelburg, S. Gilbert, and P. W. Burgess, "The present and future use of functional near-infrared spectroscopy (fNIRS) for cognitive neuroscience," *Annals of the New York Academy of Sciences*, pp. 1–25, aug 2018.

[210] M. A. Yücel, J. J. Selb, T. J. Huppert, M. A. Franceschini, and D. A. Boas, "Functional Near Infrared Spectroscopy: Enabling routine functional brain imaging," *Current Opinion in Biomedical Engineering*, vol. 4, pp. 78–86, dec 2017.

[211] J. Dong, R. Bi, J. H. Ho, P. S. P. Thong, K.-C. Soo, and K. Lee, "Diffuse correlation spectroscopy with a fast Fourier transform-

based software autocorrelator," *Journal of Biomedical Optics*, vol. 17, p. 0970041, sep 2012.